SPACE ENVIRONMENT TECHNOLOGIES

SET TR 2012-001

THREE-DIMENSIONAL EXOSPHERIC HYDROGEN ATOM DISTRIBUTIONS OBTAINED FROM OBSERVATIONS OF THE GEOCORONA IN LYMAN-ALPHA

Justin J. Bailey

May 2012

Notice: This document is released for public distribution by Space Environment Technologies.

THREE-DIMENSIONAL EXOSPHERIC HYDROGEN ATOM DISTRIBUTIONS OBTAINED FROM OBSERVATIONS OF THE GEOCORONA IN LYMAN-ALPHA

by

Justin J. Bailey

A Dissertation Presented to the
FACULTY OF THE USC GRADUATE SCHOOL
UNIVERSITY OF SOUTHERN CALIFORNIA
In Partial Fulfillment of the
Requirements for the Degree
DOCTOR OF PHILOSOPHY
(ASTRONAUTICAL ENGINEERING)

May 2012

for my wife, Natalie, a bona fide yogini

who at times had to wrap her hands around my head

to keep my brain from falling out

Acknowledgements

My opportunity to contribute in this field was established and supported by many different people. After finishing with an M.S. in Astronautical Engineering, I walked into Professor Mike Gruntman's office hoping to learn more about space physics and aeronomy. He proceeded to draw the geocorona in assorted colors on a whiteboard, and it was then that the content of this dissertation was born. Of course, none of this research would have been possible were it not for his expertise and guidance.

I would like to thank my advisory committee (Professors Daniel Erwin, Joseph Kunc, W. Kent Tobiska, and Darrell Judge) for their many insightful observations. I am especially indebted to Dr. Tobiska for numerous opportunities to learn more about the solar output and how it drives the exosphere, leading to a much more descriptive science discussion in the relevant sections.

The TWINS science team offered invaluable feedback, most notably during our collaboration with Professor Hans J. Fahr and Doctors H. Uwe Nass, Jochen Zoennchen, and the late Guenter Lay at the University of Bonn. I am particularly grateful to my colleague and friend, Jochen, for initially providing some necessary details about LAD operations. Also, I very much appreciate that Raluca Ilie at Los Alamos National Laboratory allowed me to summarize some of her recent work in ring current modeling to show an example application of exospheric H density distributions.

This work has been financially supported in part by NASA's TWINS mission. I would also like to acknowledge the Northrop Grumman fellowship program for funding my entire graduate education.

Table of Contents

List of Tables

List of Figures

Abstract

Exospheric atomic hydrogen (H) resonantly scatters solar Lyman-α (121.567 nm) radiation, observed as the glow of the geocorona. Measurements of scattered solar photons allow one to probe time-varying three-dimensional distributions of exospheric H atoms. The Two Wide-angle Imaging Neutral-atom Spectrometers (TWINS) mission images the magnetosphere in energetic neutral atom (ENA) fluxes and additionally carries Lyman-α Detectors (LADs) to register line-of-sight intensities of the geocorona. This work details a process for preparing TWINS data such that LAD measurements can be used to obtain global H density distributions with three-dimensional asymmetries above 3 earth radii. Sequences of distributions are presented to investigate the dynamic exosphere, responding to seasonal variations between a summer solstice and autumnal equinox, as well as to solar and geomagnetic variations as described by commonly used indices. The distributions reveal asymmetries from day to night, north to south, and dawn to dusk. A nightside extension persists that is consistent with the location of a geotail. A seasonal north-south asymmetry occurs as solar illumination differs between the summer and winter polar regions. Pole-equator and less pronounced dawn-dusk asymmetries also appear, possibly due to a coupling effect via charge exchange with the polar wind and plasmasphere, respectively.

A common phenomenon in geospace occurs as magnetospheric energetic ions collide with neutral background atoms and produce ENAs that, no longer bound by Earth's magnetic field, can travel large distances though space with minimal disturbance — providing an opportunity for remote detection. Knowledge of the distribution of the

primary neutral partner, exospheric H atoms, is therefore essential for the interpretation of ENA fluxes and subsequent retrieval of ion densities. An analysis is summarized that demonstrates the importance of exospheric H density distributions on reconstructing magnetospheric images in ENA fluxes and obtaining ring current ion densities.

Some of the main findings in this work have been accepted [*Ilie et al.*, 2012] or are already published [*Bailey and Gruntman*, 2011; *Zoennchen et al.*, 2011] in various scientific journals.

Chapter 1: Introduction

The most abundant neutral constituent in Earth's upper exosphere, atomic hydrogen (H), resonantly scatters solar Lyman-α (121.567 nm) radiation – creating a phenomenon known as the geocorona. Several space experiments have observed the geocorona under various conditions. The first geocoronal Lyman-α measurements were obtained by sounding rocket experiments that started in the late 1950s [e.g., *Kupperian et al.*, 1959; *Donahue*, 1966]. In comparison to rocket-born experiments, satellite missions provided observations over longer time scales. In particular, these longer duration observations were first recorded by three of the Orbiting Geophysical Observatory satellites, OGO-3, -4, -5, and -6 [*Bertaux and Blamont*, 1970; *Mange and Meier*, 1970; *Thomas*, 1970], followed by one of the Orbiting Solar Observatory satellites, OSO-4 [*Thomas and Bohlin*, 1972; *Bertaux and Blamont*, 1973; *Meier and Mange*, 1973; *Thomas and Anderson*, 1976]. The interplanetary spacecraft Mariner 5 observed the dayside geocorona as it departed for Venus [*Wallace et al.*, 1970]. Additionally, images of the geocorona were captured by astronauts using a far-ultraviolet camera/spectrograph from the lunar surface during the Apollo 16 mission [*Carruthers et al.*, 1976]. Figure 1 is one such image with the limb of Earth's nightside silhouetted by the optically thick region of the geocorona. The spatial distribution over a large region is captured for a short period (1 minute) of time. A sequence of images could be used to unambiguously separate spatial and temporal variations.

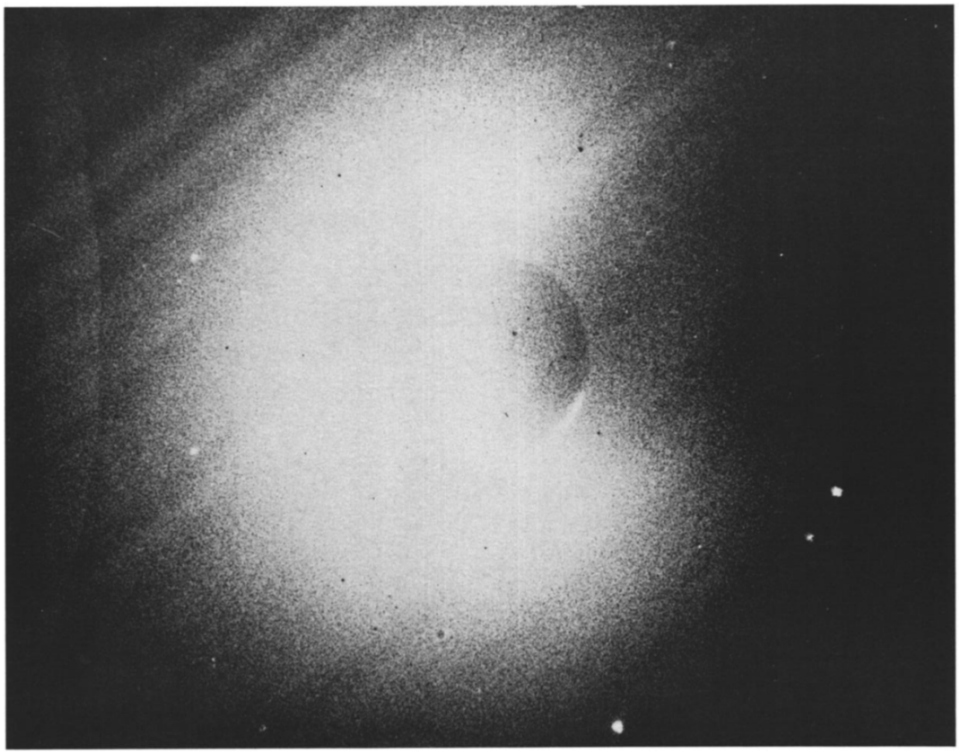

Figure 1. A 1 minute exposure with wavelength range 105 – 160 nm of the optically thick region of the geocorona, taken by astronauts on the Apollo 16 mission. The dark limb of Earth's nightside is seen silhouetted by the geocoronal Lyman-α glow [*Carruthers et al.*, 1976].

More recent space experiments have been used to reconstruct global H density distributions over time scales which depend on observational coverage [*Rairden et al.* 1983, 1986; *Østgaard et al.*, 2003; *Zoennchen et al.*, 2010]. This experimental study uses Lyman-α Detector (LAD) measurements from the Two Wide-angle Imaging Neutral-atom Spectrometers (TWINS) mission [*McComas et al.*, 2009] to obtain global distributions with three-dimensional asymmetries for time periods of a day or five days. The LADs register line-of-sight intensities of Lyman-α radiation that resonantly scatters on H atoms of both terrestrial and extraterrestrial origins. The contribution that comes from interplanetary H atoms, called the interplanetary glow, must be approximated and subtracted out of measurements to obtain exospheric H density distributions.

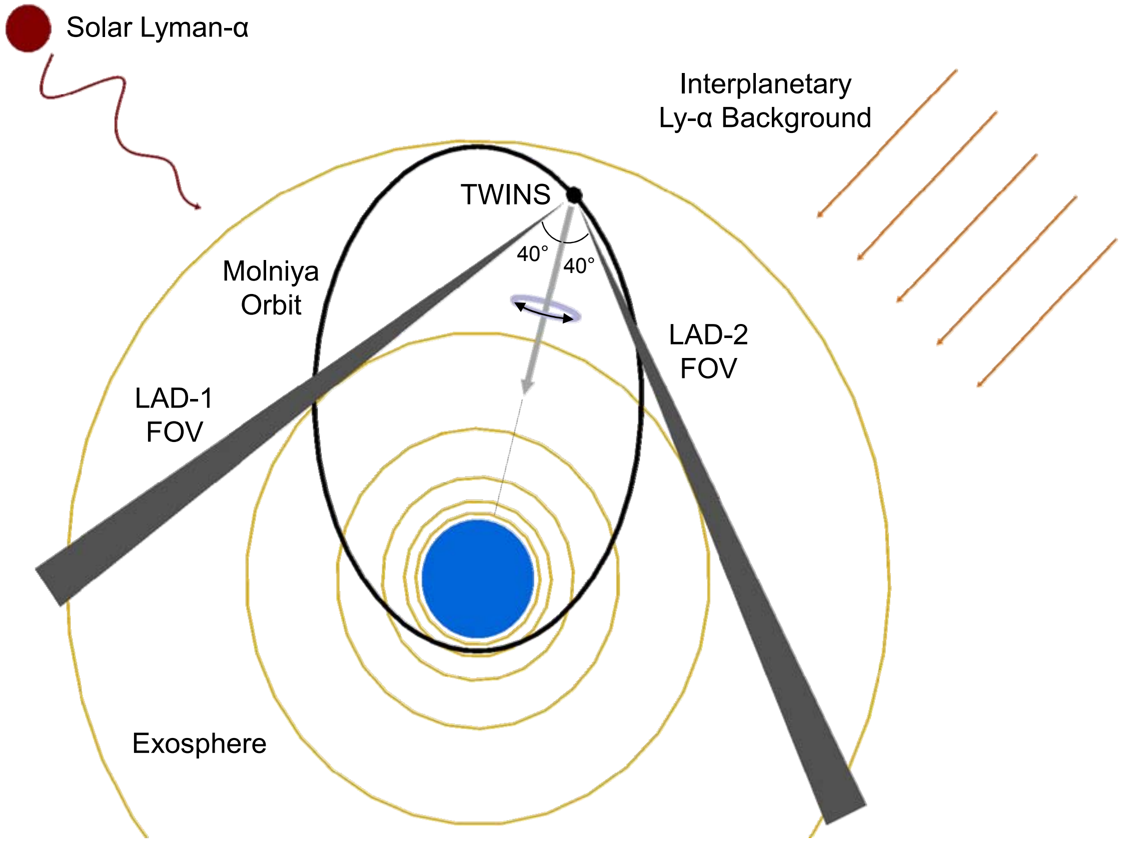

Figure 2. Space-based measurements of the geocorona include a contribution of scattered solar Lyman-α radiation that comes from interplanetary H atoms.

The geocorona reveals an exosphere that is asymmetric, including higher nightside densities, sometimes called the geotail [e.g., *Thomas and Bohlin*, 1972; *Bertaux and Blamont*, 1973; *Carruthers et al.*, 1976; *Rairden et al.*, 1986; *Østgaard et al.*, 2003; *Zoennchen et al.*, 2010]. This work focuses on geocentric distances $r > 3$ R_E (1 R_E = 6371 km is Earth's mean radius), where the H densities are low enough to assume optically thin conditions. The uncertainty introduced by assuming optically thin conditions does not exceed 20% at the minimal geocentric distance of 3 R_E and decreases with altitude. Closer to Earth, the denser conditions require a much more complex essentially radiation transfer treatment [e.g., *Thomas*, 1963; *Meier*, 1969; *Meier and Mange*, 1970; *Anderson and Hord*, 1977; *Rairden et al.*, 1986; *Bush and Chakrabarti*, 1995; *Bishop*, 1999] that is beyond the scope of this work. In this single scattering environment, the observed intensity of scattered Lyman-α radiation is simply proportional to the integral of the H density over the line-of-sight. The predicted intensity flux, F_P, as observed by the LADs, in units of rayleigh (R), 1 R = $10^6/(4\pi)$ phot cm^{-2} s^{-1} sr^{-1}, is

$$F_P = \frac{g^*}{10^6} \int_0^{L_{max}} n(\vec{L})\, I(\alpha)\ dL + F_{IP}\ , \tag{1}$$

where $n(\vec{L})$ is the local H number density along the line-of-sight $\vec{L}$; $I(\alpha)$ is a factor that accounts for the angular dependence of scattered Lyman-α photons; g^* is the local (adjusted to the actual heliocentric distance) scattering rate, the g-factor; and F_{IP} is the contribution of resonantly scattered Lyman-α radiation that comes from the extraterrestrial H population, called the interplanetary glow. Figure 3 shows the predicted H number density along a selected line-of-sight, as an example, allowing one to see the contributions of various parts of the exosphere. The line-of-sight passes through the Northern Hemisphere with a maximum H number density of n_H = 175 cm^{-3} at a geocentric distance of closest approach to the Earth of r_{LOS} = 4.4 R_E.

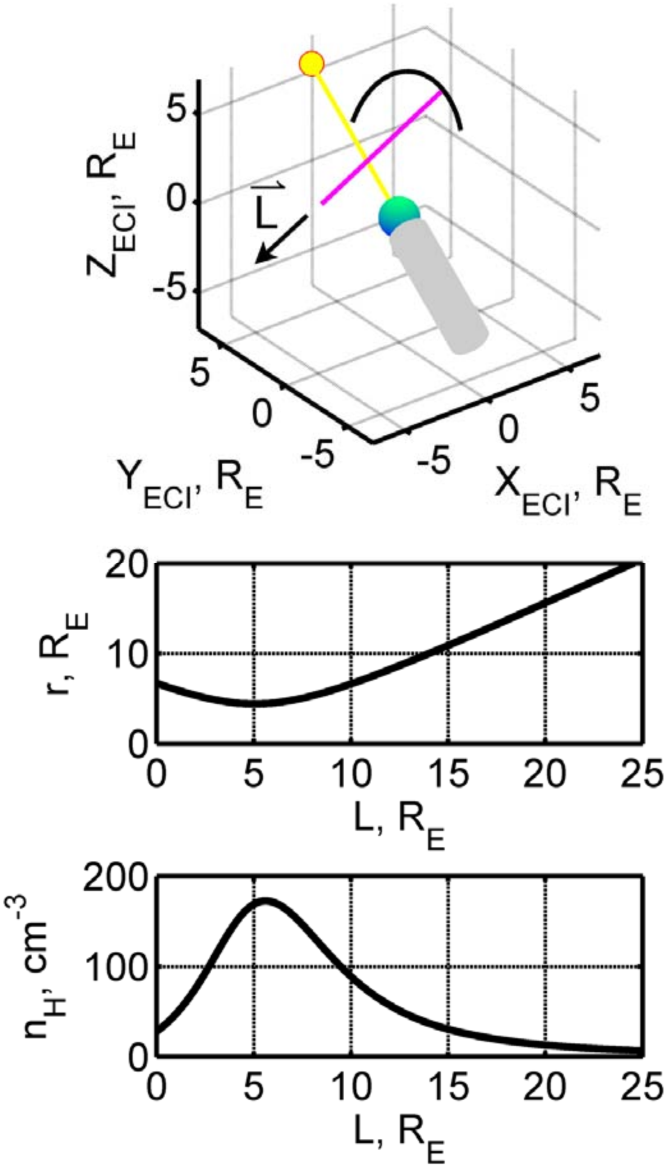

Figure 3. Atomic hydrogen number density distribution dependence on distance L from the observer (bottom) for the selected line-of-sight $\vec{L}$ (top); the middle panel shows the geocentric distance for a given point as a function of L. The blue sphere is the Earth, the yellow line and dot is the direction to the Sun, the gray cylinder is Earth's shadow, and the black curve is the spacecraft trajectory. The observer is at 6.7 R_E; r_{LOS} = 4.4 R_E.

The interaction between charged and neutral particles is a common phenomenon in geospace. Energetic ions collide with neutral background atoms and produce energetic neutral atoms (ENAs) that, no longer bound by Earth's magnetic field, can travel large distances through space with minimal disturbance (Figure 4), providing an opportunity for remote detection [*Roelof*, 1987; *Gruntman*, 1997].

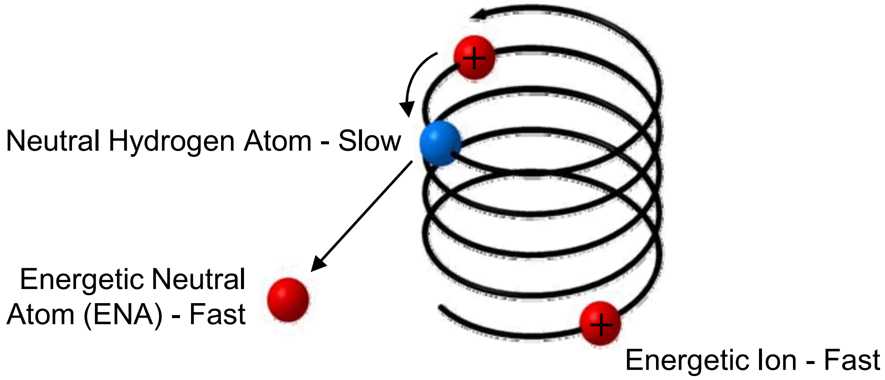

Figure 4. An energetic neutral atom (ENA) is produced when a fast energetic ion collides in charge exchange with a slow neutral background atom. The ENA, not bound by Earth's magnetic field, can then travel large distances through space with minimal disturbance.

The most abundant space plasma ion is protons (H^+). Unlike other space plasma ions (e.g., He^+ and O^+), protons cannot be imaged optically and consequently the only practical way to remotely image populations is with ENAs. Since the primary charge exchange interaction is between protons and H atoms,

$$H^+_{hot} + H_{cool} \rightarrow H_{hot} + H^+_{cool} \, , \qquad (2)$$

knowledge of the H density distribution is essential for the interpretation of ENA fluxes and subsequent retrieval of ion densities. Furthermore, this charge exchange process is important to the plasma budget of Earth's magnetosphere. A coupling effect via charge exchange exists between the exosphere and the magnetospheric region of least energetic plasma, the plasmasphere. High densities (~ 10^3 cm^{-3}) of cold (~ 1 eV) plasma exist in approximately the same region of space as the Van Allen radiation belts, terminating at the plasmapause, which varies from geocentric distances of 4 R_E to 6 R_E [*Kivelson and Russell*, 1995]. An equatorial cross section of the average shape of the plasmapause includes a bulge on the duskside, a result of the opposing nature of the convection (cross-tail) and corotation electric fields [*Carpenter*, 1970; *Chappell et al.*, 1970; *Carpenter et al.*, 1993]. The enhanced duskside proton densities can rotate somewhat in local time due to interaction between the electric ($\vec{E}$) and magnetic ($\vec{B}$) fields, $\vec{E} \times \vec{B}$ drift, depending on magnetospheric condition. The principal mechanism by which the ring current, shown in Figure 5, loses ions following the occurrence of a geomagnetic storm is charge exchange with exospheric H atoms. The spatial distribution of exospheric H atoms is therefore essential to understanding the dynamics of certain magnetospheric processes such as ring current recovery.

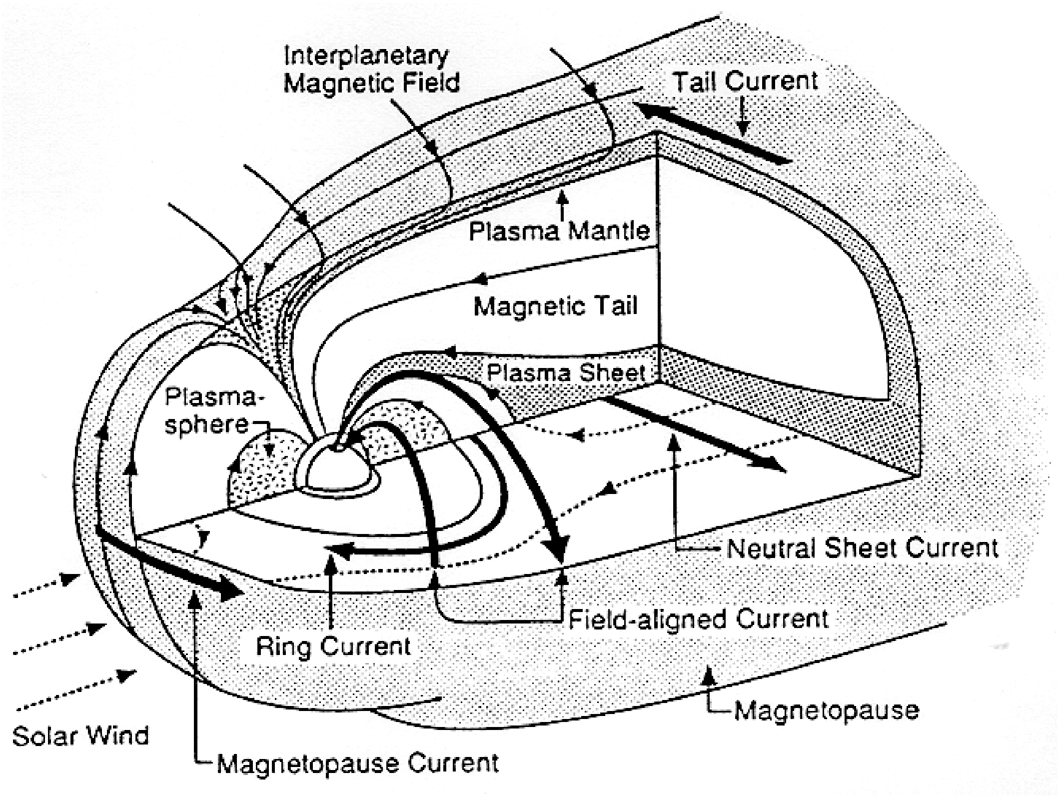

Figure 5. Three-dimensional cutaway drawing of Earth's magnetosphere showing currents, fields, and plasma regions [*Kivelson and Russell*, 1995].

Chapter 2: The Exosphere

The exosphere is the outermost layer of Earth's neutral atmosphere. The lower boundary, the exobase, is typically defined as the height above which collisions become negligible to the motion of particles and is conventionally placed at an altitude of 500 km. The upper boundary can be defined theoretically where the influence of solar radiation pressure on H atom velocities exceeds that of Earth's gravitational pull. The force of solar radiation pressure [*Chamberlain and Hunten*, 1987], F_{srp}, on an H atom is

$$F_{srp} = \frac{hg}{\lambda}, \tag{3}$$

where h is Planck's constant and g is the scattering rate of Lyman-α photons at wavelength λ = 121.567 nm. The force of Earth's gravity, F_g, on an H atom is

$$F_g = \frac{GM_E m_H}{r^2}, \tag{4}$$

where G is the gravitational constant, M_E is the mass of the Earth, m_H is the mass of an H atom, and r is the geocentric distance. An upper boundary of the exosphere can be calculated, by setting $F_{srp} = F_g$,

$$r = \sqrt{\frac{GM_E m_H \lambda}{hg}}, \tag{5}$$

as 28 R_E to 44 R_E for the maximum and minimum, respectively, Lyman-α fluxes over the last 5 solar cycles using the method detailed in Section 3.1 to obtain the scattering rate, g, at 1 AU.

As initially described by *Chamberlain* [1963], the exosphere is comprised of three main particle populations, ballistic, escaping, and satellite, moving in Earth's gravitational field and influenced by solar radiation pressure. Atoms in ballistic trajectories rise from the exobase, which is usually assumed to be between 400 and 800 km, depending on solar conditions, and eventually fall back. Atoms with velocities larger than escape velocities depart from the exobase and leave on hyperbolic trajectories. Atoms in satellite trajectories have been scattered or injected into closed orbits by rare elastic collisions or charge exchange, respectively, and do not intersect the exobase.

Ballistic trajectories dominate in a region immediately above the exobase. As the density of this population rapidly decreases towards higher altitudes, satellite particles begin to dominate above where some of the collisions and subsequent orbit apses occur. Escaping particles are present at all altitudes and at higher altitudes they are the only terrestrial population that remains. Farther away from Earth, extraterrestrial hydrogen becomes dominant. This interplanetary population is principally comprised of inflowing interstellar H atoms from the local interstellar medium (LISM) [e.g., *Fahr*, 1974; *Holzer*, 1977; *Meier*, 1977; *Thomas*, 1978; *Bertaux*, 1984; *Clarke et al.*, 1998; *Stephan et al.*, 2001; *Quémerais et al.*, 2003]. It is also possible that energetic neutral atoms (ENAs) originating in the heliospheric sheath region contribute significantly to neutral atoms within 1 AU from the Sun [*Gruntman and Izmodenov*, 2004; *Schwadron and McComas*, 2010]. At 1 AU, the extraterrestrial H number density varies between 10^{-4} and 10^{-2} cm^{-3}.

Solar radiative heating largely determines temperature and density at the exobase, which, in turn, causes a departure from spherical symmetry of the exosphere. Heating of the upper atmosphere on the dayside, by solar X-ray and extreme ultraviolet (EUV) radiation, also causes asymmetry. For example, a seasonal north-south asymmetry occurs as solar illumination differs between the summer and winter polar regions. In addition, a coupling effect via charge exchange exists between the exosphere and plasmasphere [e.g., *Bishop*, 1985; *Rairden et al.*, 1986; *Tinsley et al.*, 1986; *Hodges*, 1994].

Beyond a few Earth radii, the Keplerian motion of H atoms is also highly susceptible to an effective pressure caused by the resonant scattering of solar Lyman-α radiation. This radiation pressure force varied between the extremes of 0.85 and 2.1 times the Sun's gravitational attraction of H atoms over the last five solar cycles. The effect of this radiation pressure is rather complex and the details of how it influences the satellite population is not quantitatively completely understood yet. Some argue that the satellite population would extend in the antisolar direction, contributing to the geotail [*Bertaux and Blamont*, 1973; *Bertaux et al.*, 1995; *Østgaard et al.*, 2003; *Zoennchen et* *al.*, 2010]. However, this intuitive explanation contradicts the theoretical predictions made by *Chamberlain* [1979] and *Hodges* [1994] who suggested that the geotail was not enhanced as a result of solar radiation pressure rotating the line of apsides of satellite H orbits such that the apogees are shifted away from the Sun.

A numerical simulation performed by *Bertaux and Blamont* [1973] showed that the number of scattering perturbations necessary to significantly alter the orbital parameters of particles in the exosphere corresponds to a time longer than the characteristic time of particles in ballistic and hyperbolic trajectories, but shorter than the lifetime of particles in satellite orbits — leading to a conclusion that that the geotail must be enhanced by solar radiation pressure on satellite H atoms. Conversely, *Chamberlain* [1979] demonstrated that the global structural "shape" would be symmetric in the three principal axes but noted that his perturbation technique was unreliable for trajectories that extend well away from Earth due to the long times spent near apogee. *Chamberlain* [1980] speculated that the existence of a geotail may be due to solar radiation pressure on a loosely bound population of satellite H atoms. The relevant later work [e.g., *Bishop*, 1985; *Hodges*, 1994; *Bertaux et al.*, 1995; *Østgaard et al.*, 2003; *Zoennchen et al.*, 2010; *Bailey and Gruntman*, 2011] has yet to definitively identify the source mechanisms that create the geotail.

More recently, *Rairden et al.* [1983, 1986] fit a spherically symmetric model to geocoronal measurements by Dynamics Explorer 1 (DE 1). They also experimentally confirmed the existence of a geotail.

Hodges [1994] used Monte Carlo simulations to obtain asymmetric global H distributions under solar conditions characterized by F10.7 values representative of a typical solar cycle. For each used F10.7 value (80, 130, 180, and 230), distributions were presented for both equinox and solstice. The H concentrations were noticeably greater at solstice. In addition, his theoretical predictions exhibited an enhancement in the antisolar direction (geotail) and a secondary enhancement in the solar direction. By running simulations with and without resonant scattering of solar Lyman-α photons, he showed that both maxima are related to the effect of solar radiation pressure. He argued that the presence of two maxima contradicts the notion that solar radiation pressure simply turns the line of apsides of satellite H orbits such that the apogees are pushed tailward.

Using the Geocoronal Imager (GEO) on board the Imager for Magnetopause-to-Aurora Global Exploration (IMAGE) mission, *Østgaard et al.* [2003] derived H density profiles that were close to what was reported in *Rairden et al.* [1986]. However, above 8 R_E, they found higher densities. They also confirmed the existence of a geotail and attributed this feature to solar Lyman-α radiation pressure on the satellite population.

A group at the University of Bonn used Lyman-α measurements [*Zoennchen et al.*, 2010] from the LADs on TWINS to derive asymmetric exospheric H distributions for the Northern Hemisphere. They applied a conveniently simplified version [*Nass et al.*, 2006] of the mathematical expansion developed by *Hodges* [1994] to obtain distributions in the summer months of 2008. As compared to *Hodges* [1994] and *Østgaard et al.* [2003], the Bonn group found significantly higher day-night asymmetry, showing a much more pronounced geotail. Additionally, the Bonn group observed much weaker pole-equator asymmetry than *Hodges* [1994].

Prior models of exospheric H density distributions were usually developed under assumptions of being spherically symmetric, or representative of typical (not actual) solar conditions, or averaged over an extended period of time (Table 1). For example, the *Chamberlain* [1963] model is spherically symmetric and based entirely on theoretical predictions. The *Rairden et al.* [1986] model is spherically symmetric and averages DE 1 observations over a 4 year period assuming a constant solar Lyman-α flux at 1 AU of 3.0×10^{11} ph cm^{-2} s^{-1}. While the *Hodges* [1994] model is asymmetric, its distributions were computationally rather than experimentally derived and are representative of four F10.7 solar cycle conditions at equinox and solstice. The *Østgaard et al.* [2003] model is asymmetric, but due to the specifics of GEO/IMAGE observational geometry it averages measurements over the time scale of a year.

Table 1. Prior models of exospheric H density distributions that were developed under assumptions of being spherically symmetric, or representative of typical (not actual) solar conditions, or averaged over an extended period of time.

Model	Spherically Symmetric	Solar Output	Averaging
Chamberlain, 1963	Yes	Indirect	Constant
Rairden et al., 1983	Yes	Lyman-α	4 years
Hodges, 1994	No	F10.7	Solstice and Equinox
Østgaard et al., 2003	No	Lyman-α	1 year

This work expands *the Bonn model* developed by *Nass et al.* [2006] to describe the spatial distribution of exospheric H density. Specifically, the modifications include (1) additional fitting parameters sensitive to possible dawn-dusk asymmetry, (2) an accurate anisotropic photon scattering function, (3) a photon scattering rate at 1 AU (g-factor) obtained from independent measurements of the solar Lyman-α, and (4) an experimentally determined interplanetary glow background derived directly from Solar Wind Anisotropies (SWAN) measurements on the SOlar and Heliospheric Observatory (SOHO) mission.

Chapter 3: Experimental Study of the Exosphere

The method used to retrieve exospheric H densities relies on measuring the brightness of the geocorona. The obtained H atom abundance and three-dimensional asymmetries are therefore directly dependent on the measurement accuracy of both the geocoronal brightness from the LADs (Section 3.1) and independent observations of the solar Lyman-α irradiance (Section 3.2). Furthermore, the use of accurate anisotropic scattering of Lyman-α photons is essential to avoid artifacts in reconstructed distributions (Section 3.3).

3.1 Obtaining H Densities from Observations of the Geocorona

The transition from the optically thick to optically thin regime in the exosphere is gradual with increasing geocentric distance. The brightness of the underlying optically thick region could be as high as 35 kR and its emission would constitute [*Østgaard et al.*, 2003; *Zoennchen et al.*, 2010], at distances > 3 R_E, less than 2% of the incident solar Lyman-α radiation. The exospheric emissions are confined however to a significantly narrower spectral band than the rather broad solar line. Detailed simulations by *Bishop* [1999] show that the altitude-dependent contribution to the glow source function by the multiply scattered photons would vary, depending on the Sun angle, between 10 – 20% and 5 – 7% at geocentric distances 3 R_E and 8 R_E, respectively. Consequently, the uncertainties of exospheric number densities would also be of the same order, that is less than 20% at 3 R_E and decreasing with increasing geocentric distance.

3.2 Solar Output

The solar output in a broad spectral range, from X-rays to ultraviolet, drives the distribution of atomic hydrogen in the exosphere. Vertical transport of H atoms in the mesosphere, formed by photodissocation of water vapor and methane [*Liu and Donahue*, 1974; *Hunten and Strobel*, 1974; *Hodges*, 1994], determines the density and temperature at the exobase. The global structure of the exosphere thus depends on solar radiative heating that causes vertical transport and resultant variations at the exobase. For geocentric distances where TWINS observations are especially sensitive, from 3 R_E to 8 R_E, the exosphere is influenced by resonantly scattered solar Lyman-α radiation that causes an effective pressure; photoionization by solar photons with wavelength $\lambda < 91.1$ nm; and coupling via charge exchange with the plasmasphere and polar wind.

The characteristic times of processes that govern atom injection, dynamics, and losses are different. A few solar indices, namely F10.7, E10.7, and S10.7, are available to characterize the observational conditions (Figure 6). F10.7 is the solar flux at 10.7 cm wavelength. E10.7 is the integrated X-ray and EUV flux between 1-105 nm, especially important for photoionization and heating [*Tobiska*, 2001]. S10.7 is the integrated EUV flux between 26-34 nm, dominated by the chromospheric He II line at 30.4 nm and the coronal Fe XV line at 28.4 nm; it contributes to the thermospheric heating and expansion [*Tobiska et al.*, 2008] that affects the injection of H atoms into the exosphere.

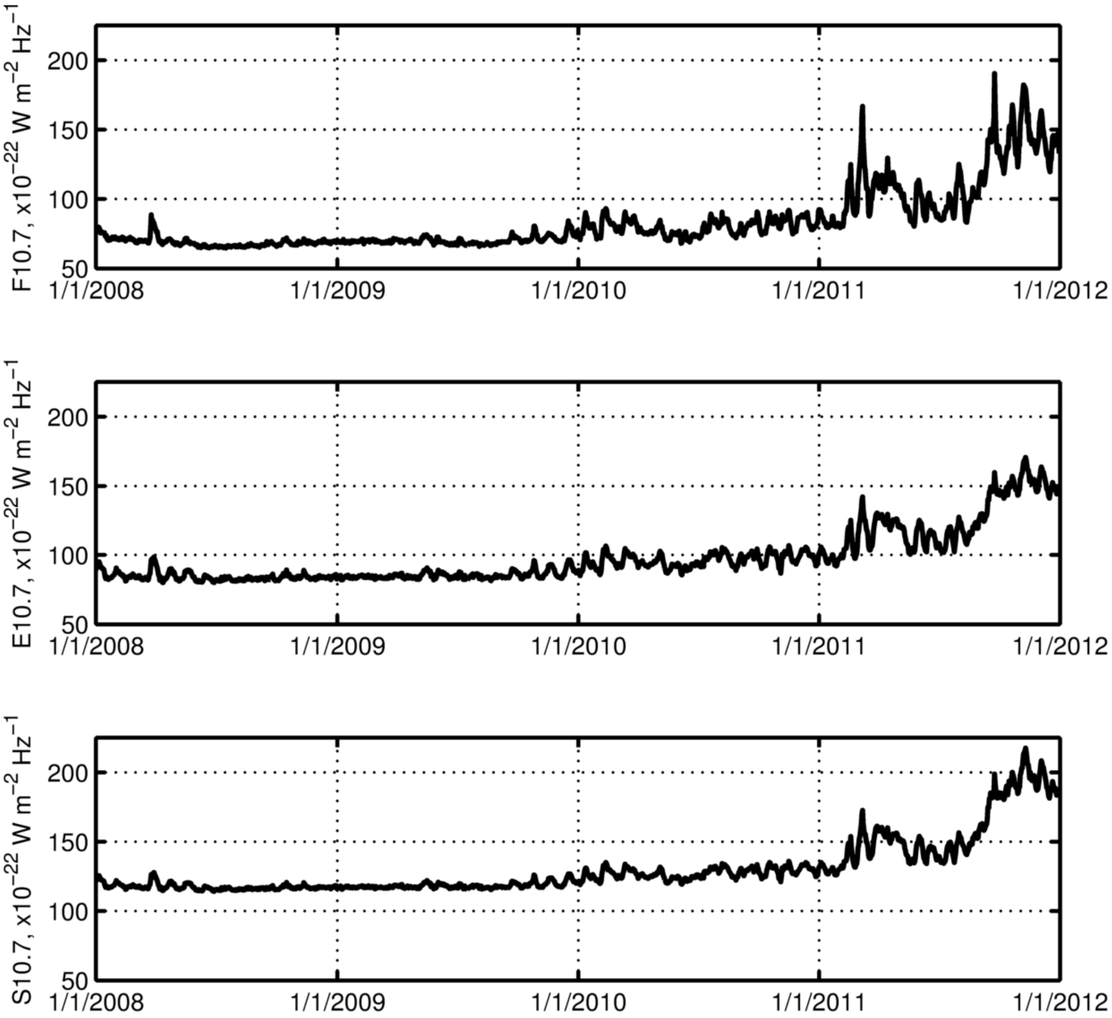

Figure 6. The solar output, shown in F10.7 (top), E10.7 (middle), and S10.7 (bottom) indices, prominently varies over two time scales. First, the passage of active regions across the solar disk during a solar rotation period produces irradiance variations over approximately 27 days. Second, the solar activity cycle generates irradiance variations over approximately 11 years. Solar Irradiance Platform (SIP) v2.37 historical irradiances are provided courtesy of W. Kent Tobiska and Space Environment Technologies, http://www.spacewx.com/solar2000.html.

The bright solar Lyman-α line of hydrogen emission, formed in the chromosphere and transition region of the solar atmosphere, is an important ultraviolet source of energy throughout the solar system. Solar Lyman-α radiation penetrates into the mesosphere and deposits energy mainly by molecular oxygen dissociation in the 70 to 100 km region. The photons additionally dissociate water in the mesosphere and ionize nitric oxide to form the ionospheric D layer that exists between 80 and 110 km [*Woods et al.*, 2000]. The solar Lyman-α emission is important to this experimental study for two reasons. First, the LAD count rates are proportional to the solar Lyman-α flux. Second, an effective pressure caused by scattered solar Lyman-α radiation affects the dynamics and lifetimes of H atoms in the exosphere.

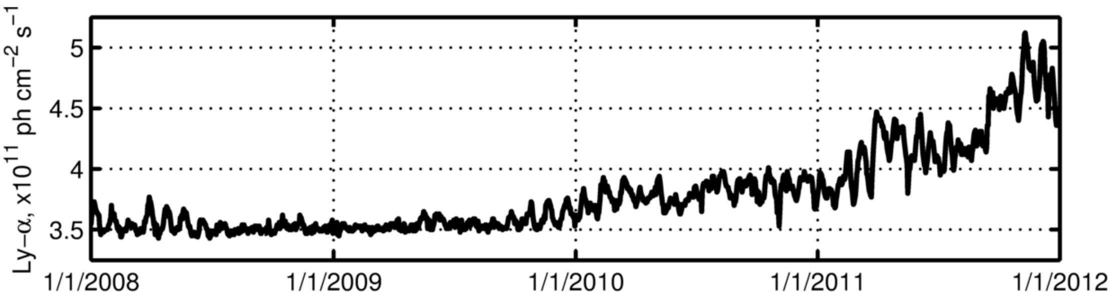

Figure 7. The composite solar Lyman-α flux at 1 AU, available at the Laboratory for Atmospheric and Space Physics (LASP) website, http://lasp.colorado.edu/lisird/lya/, that includes the latest Thermosphere Ionosphere Mesosphere Energetics and Dynamics (TIMED) Solar EUV Experiment (SEE) and SOlar Radiation and Climate Experiment (SORCE) SOLar Stellar Irradiance Comparison Experiment (SOLSTICE) measurements that have been scaled to the Upper Atmosphere Research Satellite (UARS) reference level as discussed by *Woods et al.* [2000].

The Lyman-α resonant scattering rate, g or g-factor (s^{-1}), is determined by the spectral density at the center of the solar Lyman-α line profile. This spectral density, in turn, correlates with the total solar Lyman-α line flux. A semi-empirical relationship between the central spectral, f, and (integrated over the whole Lyman-α line profile) sum total, F, irradiances in units ph cm^{-2} nm^{-1} and ph cm^{-2} s^{-1}, respectively, was defined by *Emerich et al.* [2005] as

$$\frac{f}{10^{12}\ s^{-1}\ cm^{-2}\ nm^{-1}} = 0.64\left(\frac{F}{10^{11}\ s^{-1}\ cm^{-2}}\right)^{1.21} \pm 0.08\,, \tag{6}$$

using measurements from the Solar Ultraviolet Measurements of Emitted Radiation (SUMER) spectrometer onboard the SOlar and Helospheric Observatory (SOHO) mission. For an H atom, the transition probability [*Bethe and Salpeter*, 1957; *Gruntman*, 1989] between the ground state (n = 1, l = 0) and the state (n, l = 1) is

$$A_{10}^{n1} = 8 \times 10^{9} \cdot \frac{2^{8} \cdot n \cdot (n-1)^{2n-2}}{3 \cdot (n+1)^{2n+2}}\, s^{-1}\,, \tag{7}$$

where, for n = 2, A_{10}^{21} = 1.872995 × 10^{9} s^{-1}. The rate at which an H atom will excite to the state n = 2, the g-factor, is then the product of the transition probability, A_{10}^{21}, and $\frac{c^3}{4h\nu^3}\rho_\omega$,

$$\begin{aligned} g &= A_{10}^{21}\frac{c^3}{4h\nu^3}\rho_\omega = A_{10}^{21}\frac{\lambda^4}{8\pi c}f_\lambda \\ &= 3.4745085 \times 10^{-4} \cdot \left(\frac{F}{10^{11} m^{-2} sec^{-1}}\right)^{1.21} s^{-1}\,. \end{aligned} \tag{8}$$

where ρ_ω is the density of radiation at the angular frequency $\omega = 2\pi\nu = \frac{2\pi c}{\lambda}$ of Lyman-alpha (λ = 121.567 nm), f_λ is the spectral irradiance density from Equation 6, c is the speed of light in vacuum, and h is Planck's constant. The composite solar Lyman-α flux at 1 AU, available at the Laboratory for Atmospheric and Space Physics (LASP) website, http://lasp.colorado.edu/lisird/lya/, provides daily values that average the latest versions of the Thermosphere Ionosphere Mesosphere Energetics and Dynamics (TIMED) Solar EUV Experiment (SEE) and SOlar Radiation and Climate Experiment (SORCE) SOLar Stellar Irradiance Comparison Experiment (SOLSTICE) measurements, scaled to match the Upper Atmosphere Research Satellite (UARS) reference level as discussed by *Woods et al.* [2000]. This composite time series is used to obtain the g-factor in part to be consistent with the interplanetary glow model, discussed in Chapter 4. It would instead be possible to use the approximately 14 - 15 measurements that are available each day by SEE, which during normal operations observes the Sun for about 3 minutes every orbit (~ 97 min). The effect of using either data set results in minimal changes to the obtained exospheric H density distributions, partially due to the low solar variation that persisted.

The solar Lyman-α flux is used to obtain the g-factor, which at 1 AU varied from extremes of 1.55×10^{-3} s^{-1} and 3.75×10^{-3} s^{-1} over the last five solar cycles. A scaling relationship is used to calculate the local g-factor, g^*, that accounts for deviations from 1 AU during Earth's orbit around the Sun,

$$g^* = g\frac{r_{sun}}{1\,AU}, \tag{9}$$

where r_{sun} is the heliocentric distance. The eccentricity of Earth's orbit around the Sun is 0.017, which translates into a ± 1.7% change in the heliocentric distance – corresponding to a ± 3.5% change in the radiation flux. The actual distance from the Earth to the Sun is always used when obtaining exospheric H density distributions.

3.3 Photon Scattering by H Atoms

Hydrogen atoms scatter Lyman-α radiation anisotropically. The angular dependence of the scattered intensity, $I(\alpha)$, obtained by *Brandt and Chamberlain* [1959],

$$I(\alpha) = 1 + \frac{1}{4}\left(\frac{2}{3} - \sin^2\alpha\right), \tag{10}$$

is shown in Figure 8. For forward (α = 0°) and backward (180°) scattering, the probability deviates from the isotropic case by over 15%.

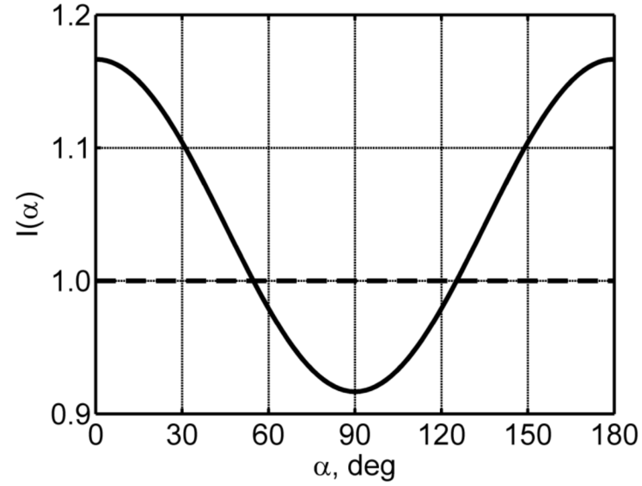

Figure 8. Scattering intensity I as a function of the scattering angle α. The horizontal dashed line, $I(\alpha)$ = 1.0, represents isotropic scattering.

The angular dependence of scattered Lyman-α photons is always applied when obtaining exospheric H density distributions. The scattering angle, α, is determined using the relationship

$$\alpha = \cos^{-1}\left(\frac{(-\vec{L}) \cdot (\vec{L}+\vec{S})}{\|-\vec{L}\|\|\vec{L}+\vec{S}\|}\right), \tag{11}$$

where $\vec{L}$ is the LAD line-of-sight vector, $\vec{S}$ is from the spacecraft to the Sun, and $\vec{S}+\vec{L}$ is from the point of scattering to the Sun as shown in Figure 9.

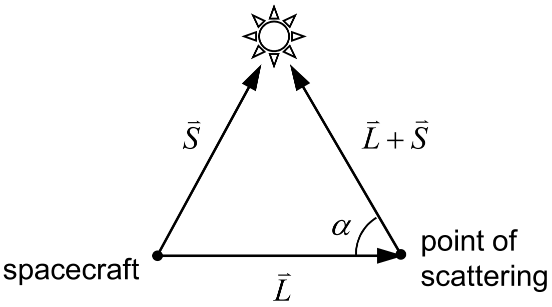

Figure 9. The observational geometry used to calculate the resonant scattering angle, α, of Lyman-α photons on exospheric H atoms, which includes the LAD line-of-sight, $\vec{L}$, a vector from the spacecraft to the Sun, $\vec{S}$, and a vector from the point of scattering to the Sun, $\vec{S}+\vec{L}$.

Chapter 4: Interplanetary Glow

The Sun resides inside a warm, partially ionized, low-density cloud of interstellar gas. Interstellar H atoms flow into the solar system filling interplanetary space [*Fahr*, 1974; *Holzer*, 1977; *Meier*, 1977; *Thomas*, 1978; *Bertaux*, 1984]. Similar to terrestrial H atoms, interplanetary atoms also resonantly scatter solar Lyman-α photons, producing the interplanetary glow with typical intensities that vary from 200 to 1000 R depending on look direction and solar conditions.

The Solar Wind ANisotropies (SWAN) instrument [*Bertaux et al.*, 1995] on the SOlar and Heliospheric Observatory (SOHO) mission made extensive observations of the interplanetary glow. Figure 10 shows the observed Lyman-α background for an example day of 11 June 2008 (available at the SWAN website, http://sohowww.nascom.nasa.gov/data/summary/swan/).

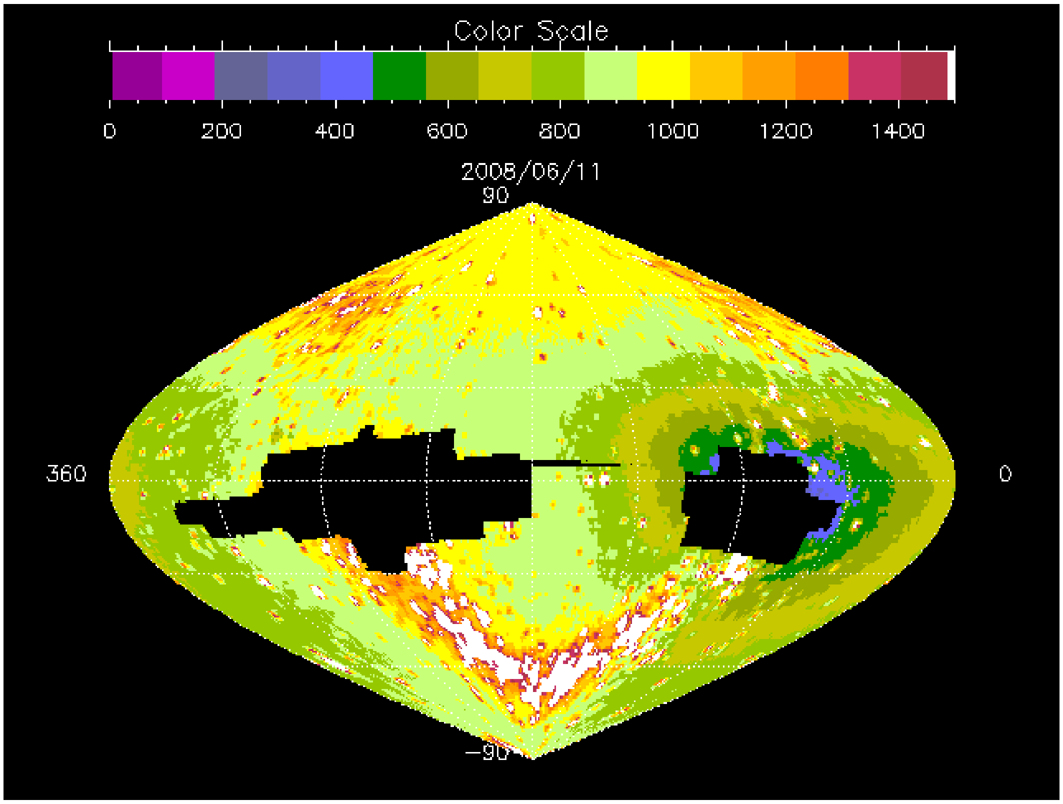

Figure 10. All-sky image of the interplanetary glow observed by the Solar Wind ANisotropies (SWAN) instrument on 11 June 2008 (available at the SWAN website, http://sohowww.nascom.nasa.gov/data/summary/swan/), where the horizontal axis is ecliptic longitude λ and the vertical axis is ecliptic latitude β. The non-uniformity of the intensity pattern, coded in false colors with a scale of counts s^{-1}, is due to a combination of varying interplanetary H atom velocities and ionization processes from the Sun. The dark areas are field of view obstructions by the sunshield and spacecraft. The white dots that are denser along the plan of the Milky Way are the emissions of hot stars.

The LAD measured intensity is the sum of the geocoronal and interplanetary glow. The contribution of the interplanetary glow must therefore be subtracted from each LAD measurement to obtain exospheric H densities. This work subtracts the interplanetary glow using all-sky maps that are derived from SWAN measurements (W. Pryor and R. Gladstone, personal communication, 2011). *Pryor et al.* [2012]

summarizes the fitting process that accounts for field of view obstructions and stellar emissions. Figure 11 is one such all-sky map for an example day on 11 June 2008.

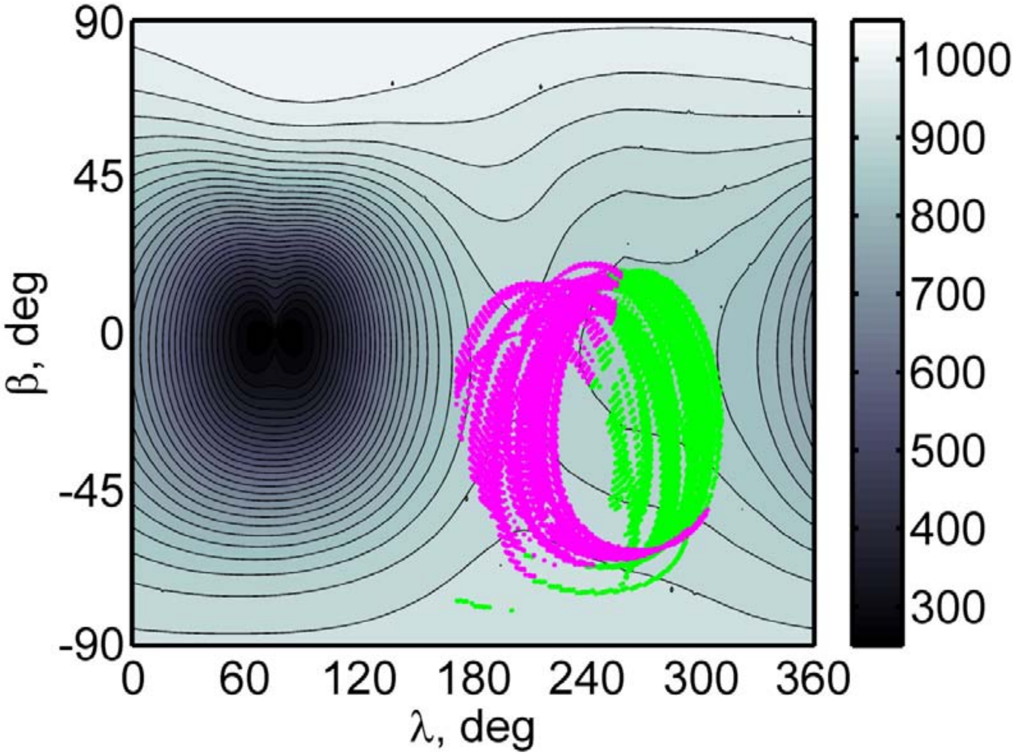

Figure 11. Interplanetary glow on 11 June 2008, derived from SWAN measurements (W. Pryor and R. Gladstone, personal communication, 2011). Green and pink dots are line-of-sight directions for LAD-1 and LAD-2, respectively. The horizontal axis is ecliptic longitude *λ*, the vertical axis is ecliptic latitude *β*, and the color bar is in rayleighs.

For all line-of-sight directions covered by the TWINS-1 LADs on 11 June 2008, the interplanetary glow varied between 860 and 940 R, accounting for 20% — 65% of the LAD measured intensities. Accuracy of the interplanetary glow predictions is therefore of critical importance when extracting exospheric H densities from LAD measurements.

Chapter 5:
Lyman-α Detectors (LADs) on NASA's TWINS Mission

The LADs were primarily included on TWINS to contribute to the science reduction of ENA images by providing time-varying three-dimensional density distributions $n_H(r, \phi, \theta, t)$. Additionally, the unprecedented observational coverage provides an opportunity to significantly advance scientific understanding of the physical processes that drive exospheric H densities.

5.1 Instrumentation

The TWINS mission [*McComas et al.*, 2009] consists of two instruments, TWINS-1 and TWINS-2, on two separate satellites launched in 2006 and 2008 to stereoscopically image the magnetosphere in ENA fluxes, which are produced in charge exchange between magnetospheric energetic ions and exospheric background H atoms. To derive ion distributions from ENA measurements, knowledge of the exospheric H density distribution is necessary. Consequently, in addition to ENA imagers, each TWINS instrument includes a pair of identical Lyman-α detectors, LADs, to register line-of-sight resonance scattered intensities. LAD data became available since June 2008.

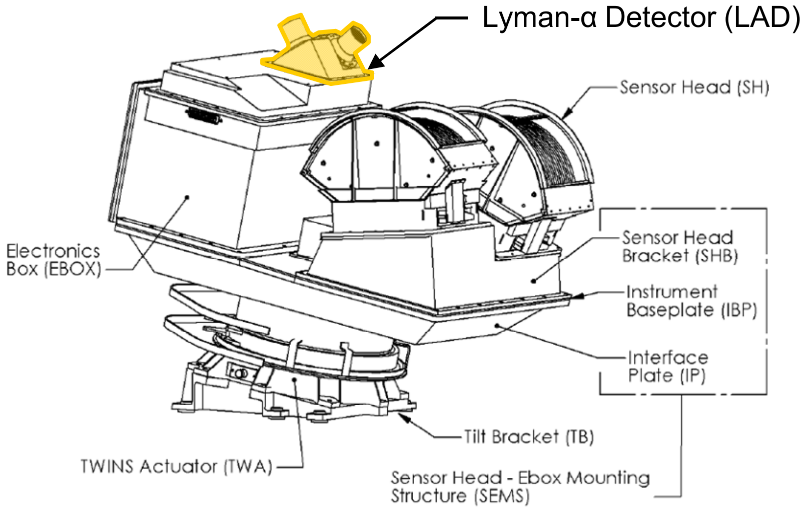

Figure 12. Each TWINS instrument, TWINS-1 and TWINS-2, includes two ENA imagers, two LADs, and environmental sensors (adapted from the Instrument Specification Document, March 2008).

In each LAD, the incident radiation passes through a collimator followed by an optical interference filter centered at the wavelength 122 nm with a bandwidth 10 nm [*Nass et al.*, 2006]. The Lyman-α photons are then counted by a channel electron multiplier. The recorded photon count rate is proportional to the incident Lyman-α intensity and the geometric factor.

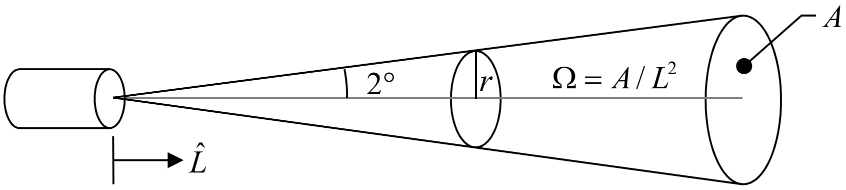

Figure 13. The field of view, Ω, of each LAD, where r is the radius and A is the area at a distance L along the line-of-sight $\hat{L}$.

The collimator on each LAD defines an aperture angle of 4° full width at half maximum. The geometric factor is obtained by first finding the radius, r, at a distance L along the line-of-sight, $\hat{L}$, using a trigonometric relationship,

$$\tan\left(\frac{4^\circ}{2}\right) = \frac{r}{L} \;\rightarrow\; r = L \tan 2^\circ . \tag{12}$$

The solid angle, Ω, of each LAD field of view is then

$$\Omega = \frac{r^2}{L^2} = \frac{\pi L^2 \tan^2 2^\circ}{L^2} = \pi \tan^2 2^\circ = 2\pi(1 - \cos 2^\circ)\,, \tag{13}$$

and the sensor sensitivity [*Nass et al.*, 2006] is approximately

$$1\,R \mathrel{\widehat{=}} \frac{10^6}{4\pi} \cdot 2\pi(1 - \cos 2^\circ) \cdot QE_f(121.6)\,\frac{cts}{s} \cong 2\,\frac{cts}{s}\,, \tag{14}$$

where $QE_f(121.6)$ is the total quantum efficiency of each detector and 1 R = 1 rayleigh = $10^6/(4\pi)$ phot cm^{-2} s^{-1} sr^{-1}. All LADs were calibrated, before the mission start, at the BESSY Synchrotron in Berlin [*Richter et al.*, 2001]. Typical intensities measured by the LADs are from 1000 to 10000 R, with corresponding count rates from 2000 to 20000 s^{-1}.

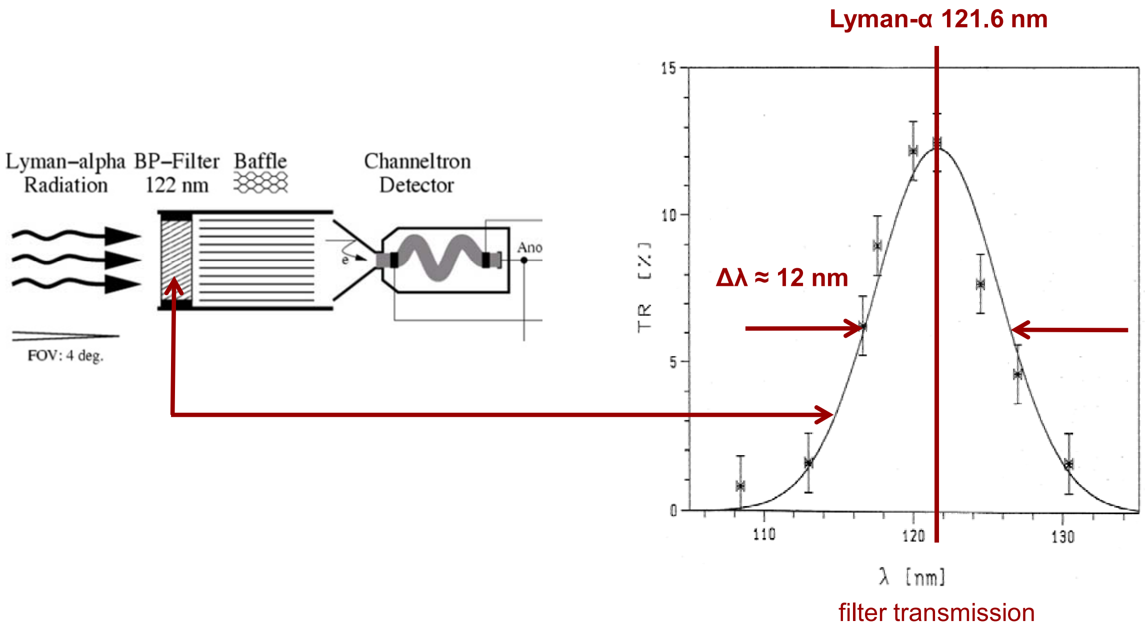

Figure 14. Lyman-α photons pass through a collimator followed by an optical interference filter before being counted by a channel electron multiplier.

5.2 Observational Coverage

The TWINS instruments fly on two satellites in widely spaced highly elliptical Molniya-type orbits, providing observational coverage from very different vantage points. On each satellite, two LADs, LAD-1 and LAD-2, observe the geocorona for several hours per orbit, where the orbital period is one half of a sidereal day. The TWINS instrument is located on a platform that rotates about a nominally nadir-pointed axis, in a windshield wiper motion, back and forth through overlapping angular limits $\Delta\omega = \pm 99°$ with a rotational rate of approximately 3˚ per second (Figure 15). Thus, it takes approximately 1 minute for LAD-1 and LAD-2, oriented 40° with respect to the actuator rotation axis, to observe a full circle around the Earth. LAD count rates are recorded every 0.67 and 1.33 sec, corresponding to $\Delta\omega = 2°$ and 4° of platform rotation. When the platform reaches $\omega = \pm 90°$, LAD-1 will point in the same direction as LAD-2 in the opposite orientation, and vice versa, allowing for cross calibration of the sensors. In general, this observational geometry provides excellent coverage of the Northern Hemisphere, where the orbit apogees are located, but may be limited in the Southern Hemisphere.

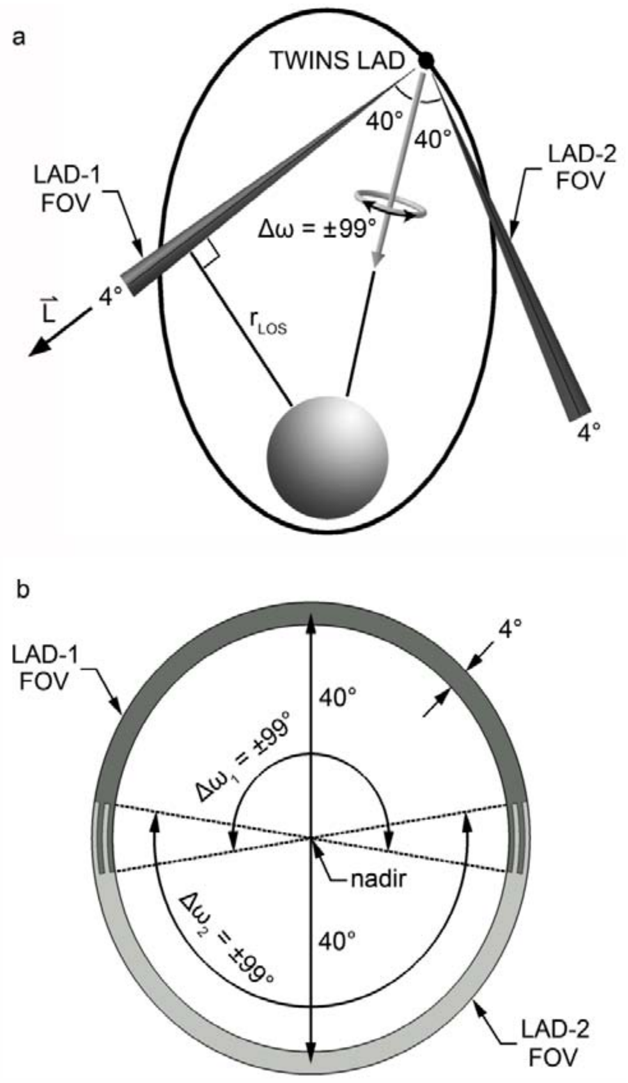

Figure 15. (a) Observational geometry of Lyman-α detectors (LAD-1 and LAD-2) on a Two Wide-angle Imaging Neutral-atom Spectrometers (TWINS) satellite in a highly elliptical Molniya-type orbit. The TWINS mission consists of two satellites, flying in similar orbits that are widely spaced. Both orbits have an apogee of 7.2 R_E over the Northern Hemisphere, an inclination of 63.4°, and an orbital period close to half a day. Variable r_{LOS} is the geocentric distance of an LAD line-of-sight, $\vec{L}$, closest approach to the Earth. Each LAD has a 4° full width half maximum field of view, pointed at 40° with respect to the rotating nominally nadir-pointed instrument platform axis. (b) LAD field of view coverage through the windshield wiper motion of the instrument platform. The light and dark shaded sections of the circle show the overlapping directions covered by LAD-1 (ω_1) and LAD-2 (ω_2), respectively, as the actuator rotates through the full motion ($\Delta\omega = \pm 99°$). Note that detector measurements are only available within the limits $\Delta\omega = \pm 90°$. The windshield wiper motion of the instrument platform results in the LAD fields of view covering a complete circle, centered on the Earth.

In total, 26 observational geometry and housekeeping limits are checked before an LAD measurement is classified as valid for scientific analysis. To avoid the hazardous environment in the Van Allen radiation belts, all instruments are turned off below an orbital radius of approximately 4.5 R_E. During the orbit, the instrument rotation axis may drift away from nadir. Consequently, the geocentric distance of an LAD line-of-sight closest approach to the Earth, r_{LOS}, varies from around 2.0 – 6.5 R_E. Below 3 R_E, the geocorona deviates substantially from being optically thin. Thus, those measurements with $r_{LOS} < 3$ R_E are excluded. To mitigate possible solar contamination [*Zoennchen et al.*, 2010], only those measurements with a detector line-of-sight pointed at > 90° from the direction to the Sun are used. Additionally, it is required that the line-of-sight does not pass through Earth's shadow, approximated by a cylinder (with 1 R_E radius) in the antisolar direction.

Consider one TWINS satellite in an orbit with typical conditions. The pair of LADs records around $2 \times 8000 = 16000$ valid measurements during the orbit. Adequate observational coverage around the Earth is essential to obtaining exospheric H density distributions because a global fitting is only sensitive to the observed regions. Figure 16 shows the observational coverage for TWINS-1 on 11 June 2008, as an example.

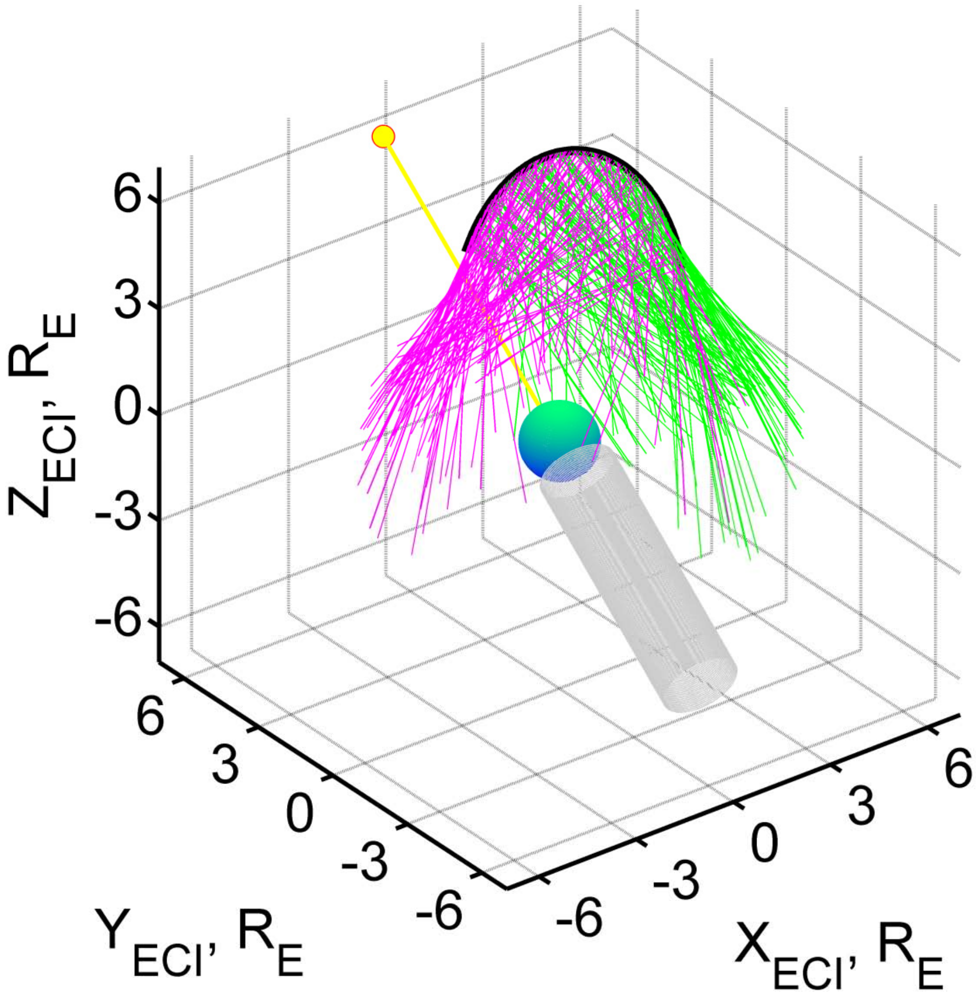

Figure 16. LAD observational coverage for TWINS-1 on 11 June 2008. The coordinate system is Earth Centered Inertial (ECI): the *x* axis points toward the vernal equinox and the *z* axis is the celestial pole. The blue sphere is the Earth, the yellow line and dot show the direction to the Sun, the shaded cylinder is Earth's shadow, the black curve is the spacecraft trajectory, and the green and pink lines represent the line-of-sight vectors for LAD-1 and LAD-2, respectively.

The observational coverage on 20 June 2008 (summer solstice) is shown in Figure 17. The requirement that lines-of-sight be pointed at > 90° eliminates only a small amount (< 1%) of LAD measurements on 11 June 2008 and 20 June 2008.

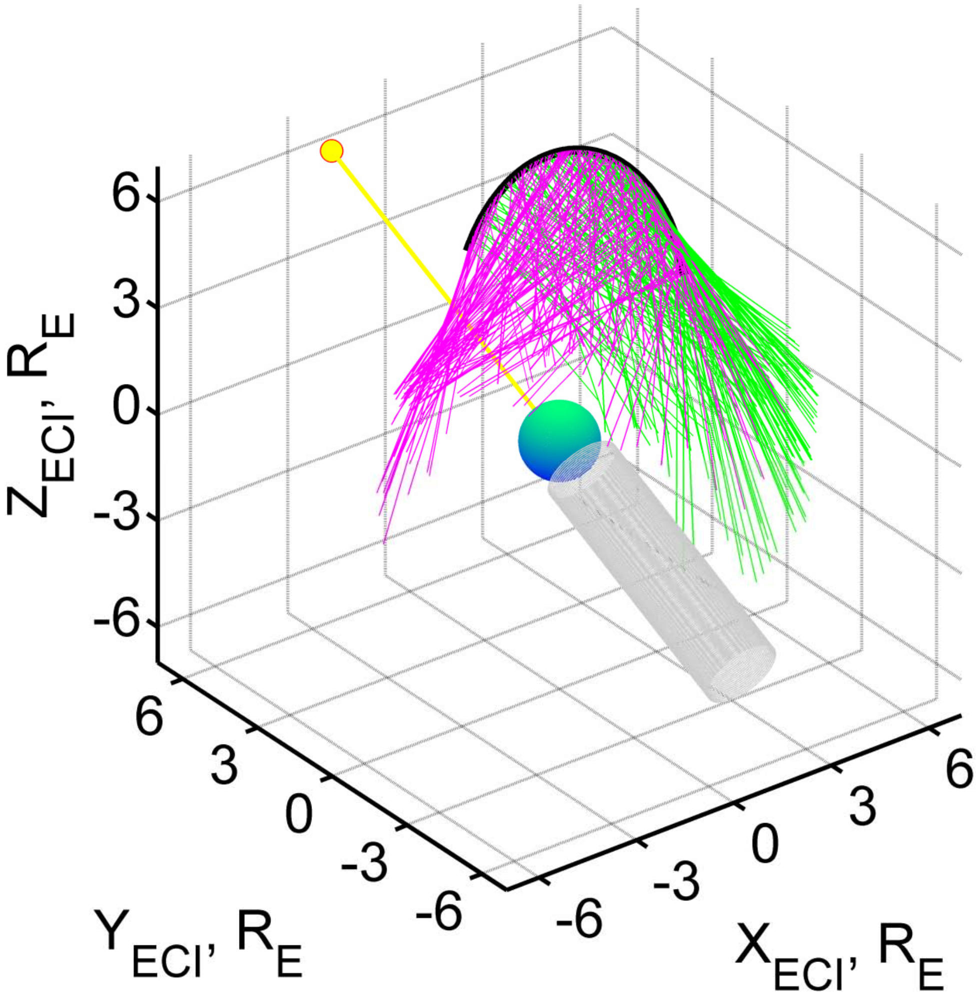

Figure 17. LAD observational coverage for TWINS-1 on 20 June 2008 (summer solstice). The coordinate system is Earth Centered Inertial (ECI): the *x* axis points toward the vernal equinox and the *z* axis is the celestial pole. The blue sphere is the Earth, the yellow line and dot show the direction to the Sun, the shaded cylinder is Earth's shadow, the black curve is the spacecraft trajectory, and the green and pink lines represent the line-of-sight vectors for LAD-1 and LAD-2, respectively.

After 20 June 2008, the favorable observational geometry continues such that all regions around the Earth are included in the next month or so of TWINS-1 orbits. Figure 18 shows the TWINS-1 coverage on 20 July 2008.

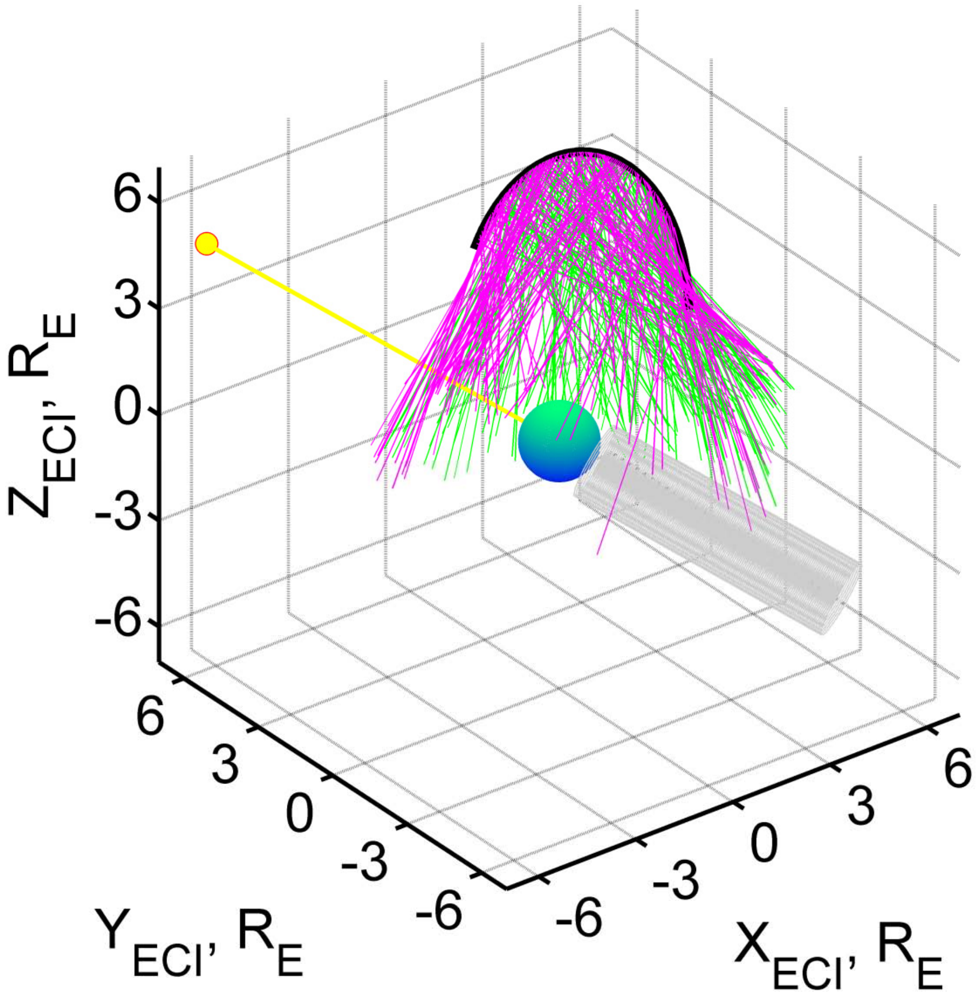

Figure 18. LAD observational coverage for TWINS-1 on 20 July 2008. The coordinate system is Earth Centered Inertial (ECI): the *x* axis points toward the vernal equinox and the *z* axis is the celestial pole. The blue sphere is the Earth, the yellow line and dot show the direction to the Sun, the shaded cylinder is Earth's shadow, the black curve is the spacecraft trajectory, and the green and pink lines represent the line-of-sight vectors for LAD-1 and LAD-2, respectively.

After 20 July 2008, the orbit orientation with respect to the seasonal position of the Sun becomes unfavorable such that > 1% of the available LAD measurements must be excluded for having lines-of-sight pointed at < 90° to the direction of the Sun. For example, by 20 August 2008 the TWINS-1 coverage (Figure 19) excludes 12.5% of the available LAD measurements to mitigate possible solar contamination.

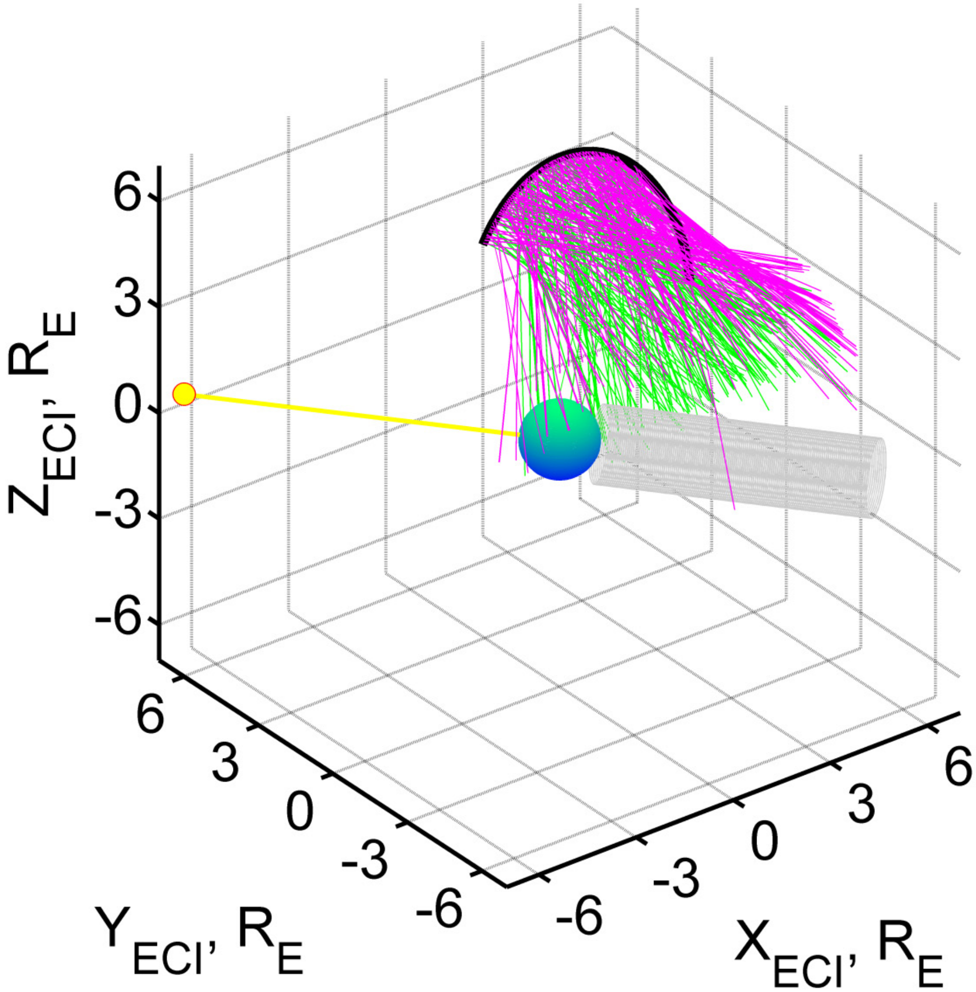

Figure 19. LAD observational coverage for TWINS-1 on 20 August 2008. The coordinate system is Earth Centered Inertial (ECI): the *x* axis points toward the vernal equinox and the *z* axis is the celestial pole. The blue sphere is the Earth, the yellow line and dot show the direction to the Sun, the shaded cylinder is Earth's shadow, the black curve is the spacecraft trajectory, and the green and pink lines represent the line-of-sight vectors for LAD-1 and LAD-2, respectively.

The lack of dayside coverage is a persistent feature for the time period after the summer months of 2008 through 2011. Two additional plots of the observational coverage on 21 July 2009 (Figure 20) and 6 August 2011 (Figure 21) are shown to further visualize the incomplete coverage.

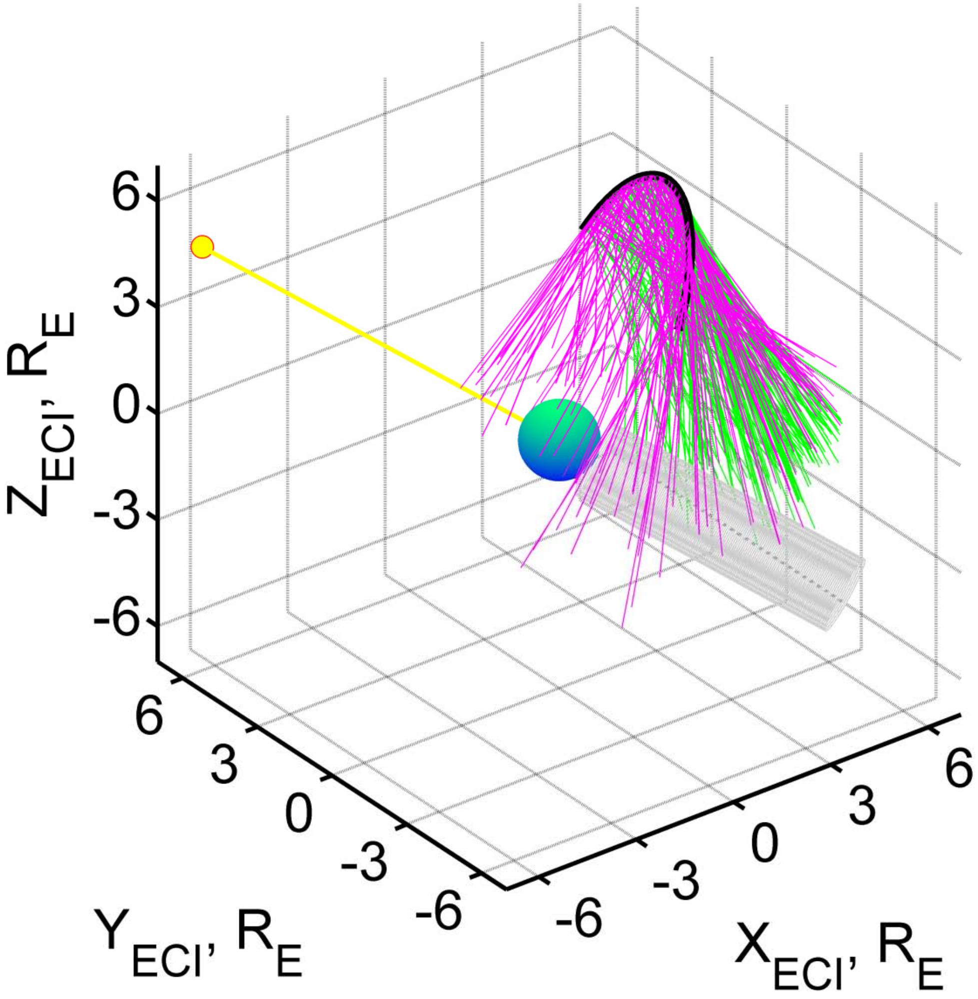

Figure 20. LAD observational coverage for TWINS-1 on 21 July 2009. The coordinate system is Earth Centered Inertial (ECI): the *x* axis points toward the vernal equinox and the *z* axis is the celestial pole. The blue sphere is the Earth, the yellow line and dot show the direction to the Sun, the shaded cylinder is Earth's shadow, the black curve is the spacecraft trajectory, and the green and pink lines represent the line-of-sight vectors for LAD-1 and LAD-2, respectively.

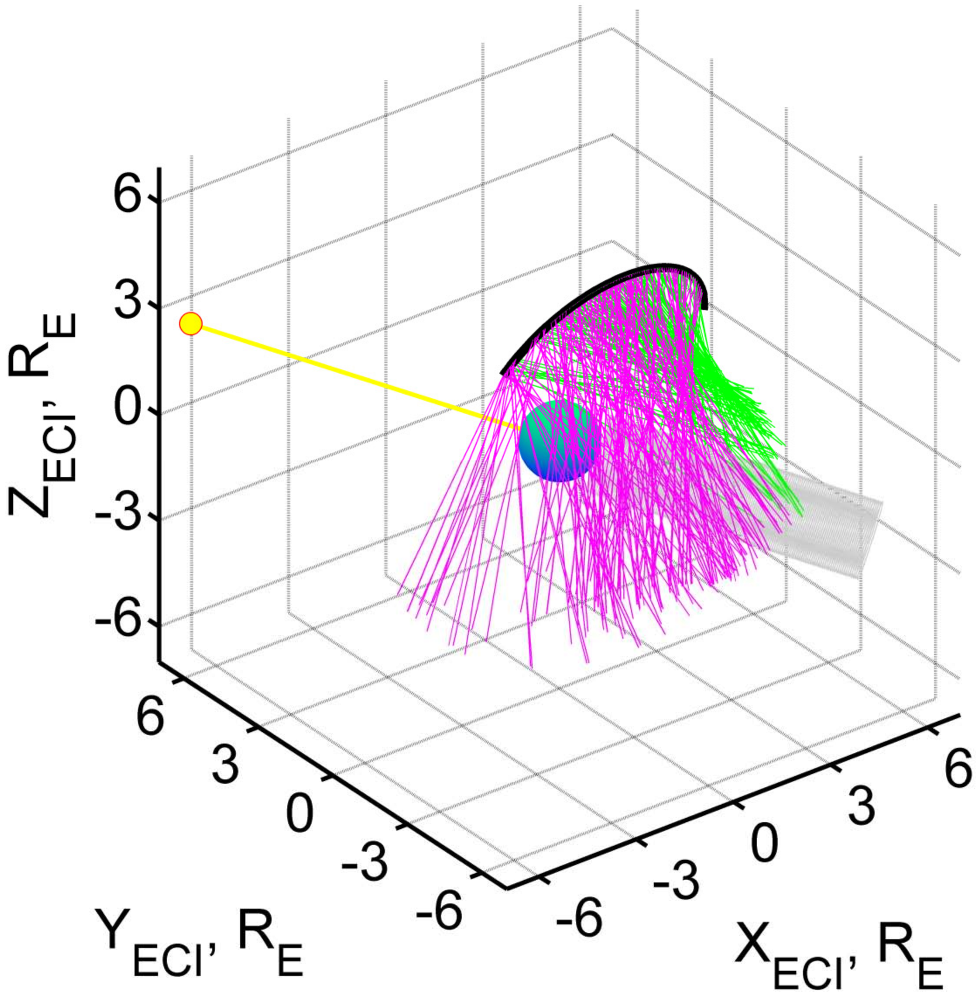

Figure 21. LAD observational coverage for TWINS-1 on 6 August 2011. The coordinate system is Earth Centered Inertial (ECI): the *x* axis points toward the vernal equinox and the *z* axis is the celestial pole. The blue sphere is the Earth, the yellow line and dot show the direction to the Sun, the shaded cylinder is Earth's shadow, the black curve is the spacecraft trajectory, and the green and pink lines represent the line-of-sight vectors for LAD-1 and LAD-2, respectively.

The incomplete coverage that persists after the summer months of 2008 is a result of unfavorable observational geometry with respect to the solar direction. A few orbital elements for both the TWINS-1 and TWINS-2 satellites were calculated to better understand the relationship between the orbit precession and the seasonal position of the Sun. The orbital angular momentum vector, $\vec{h}$, was calculated by taking the cross product,

$$\vec{h} = \vec{r} \times \vec{v}\,, \tag{15}$$

of the spacecraft position vector, $\vec{r} = \vec{r}_{S/C}$, and velocity vector, $\vec{v} = \vec{v}_{S/C}$, for a point along the orbit. Note, the spacecraft velocity vector is determined by taking the difference divided by the elapsed time between two consecutive position vectors. A vector $\vec{n}$ pointing to the ascending node,

$$\vec{n} = \hat{k} \times \vec{h} = \left(-h_x, h_y, 0\right), \tag{16}$$

where $\hat{k} = (0, 0, 1)$, is needed to obtain the longitude of the ascending node, Ω, with vernal equinox as the origin of longitude, also known as the right ascension of the ascending node (RAAN),

$$\Omega = \cos^{-1}\frac{n_x}{|\vec{n}|}. \tag{17}$$

If $n_y < 0$, then $\Omega = 2\pi - \Omega$. Next, the eccentricity vector, $\vec{e}$, is calculated,

$$\vec{e} = \frac{\vec{v} \times \vec{h}}{\mu} - \frac{\vec{r}}{|\vec{r}|} = \frac{|\vec{v}|^2 r}{\mu} - \frac{(\vec{r} \cdot \vec{v})\vec{v}}{\mu} - \frac{\vec{r}}{|\vec{r}|}, \tag{18}$$

where μ is the standard gravitational parameter of Earth. The argument of perigee, ω, is then

$$\omega = \cos^{-1} \frac{\vec{n} \cdot \vec{e}}{|\vec{n}||\vec{e}|}, \tag{19}$$

where if $e_z < 0$, $\omega = 2\pi - \omega$. The beta angle, β, between the orbit plane and the direction to the Sun, is

$$\beta = \sin^{-1} \frac{\vec{r}_{Sun} \cdot \vec{h}}{|\vec{r}_{Sun}||\vec{h}|}, \tag{20}$$

where $\vec{r}_{Sun} = (x_{Sun}, y_{Sun}, z_{Sun})$ is the solar vector. The angles right ascension, α_{Sun}, and declination, δ_{Sun}, of the solar vector,

$$\alpha_{Sun} = \tan^{-1}\left(\frac{y_{Sun}}{x_{Sun}}\right), \tag{21}$$

$$\delta_{Sun} = \sin^{-1}\left(\frac{z_{Sun}}{\sqrt{x_{Sun}^2 + y_{Sun}^2 + z_{Sun}^2}}\right), \tag{22}$$

are defined from $0^0 \leq \alpha \leq 180^0$ if $y_{Sun} \geq 0$, $180^0 \leq \alpha \leq 360^0$ if $y_{Sun} \leq 0$, and $-90^0 \leq \delta \leq 90^0$.

The orbital elements defined above are plotted for each orbit of the TWINS-1 and TWINS-2 satellite in Figure 22 and Figure 23, respectively. The change per orbit revolution for the longitude of ascending node, $\Delta\Omega$, is -0.07° and for the argument of perigee, $\Delta\omega$, is zero. The beta angle β varies by ± 90°, defined for an imaginary observer at the Sun as positive for counter clockwise and negative for clockwise rotation. The right ascension, α_{Sun}, and declination, δ_{Sun}, of the Sun vary yearly from 0° to 360° and seasonally from ± 23.5°, respectively.

The regions shaded in yellow highlight when orbit apogees are on the dayside of the Earth. This orientation provides favorable coverage as the nominally nadir-pointed axis of the instrument is generally looking away from the Sun and the amount of LAD lines-of-sight excluded for pointing at > 90° to the solar vector is minimal. The ideal observational conditions would be when the orbit apogee is on the dayside of the Earth, directly above the solar vector, during summer solstice when the Sun's declination is 23.5°. The most similar observational geometry to the ideal conditions occurred in the summer months of 2008.

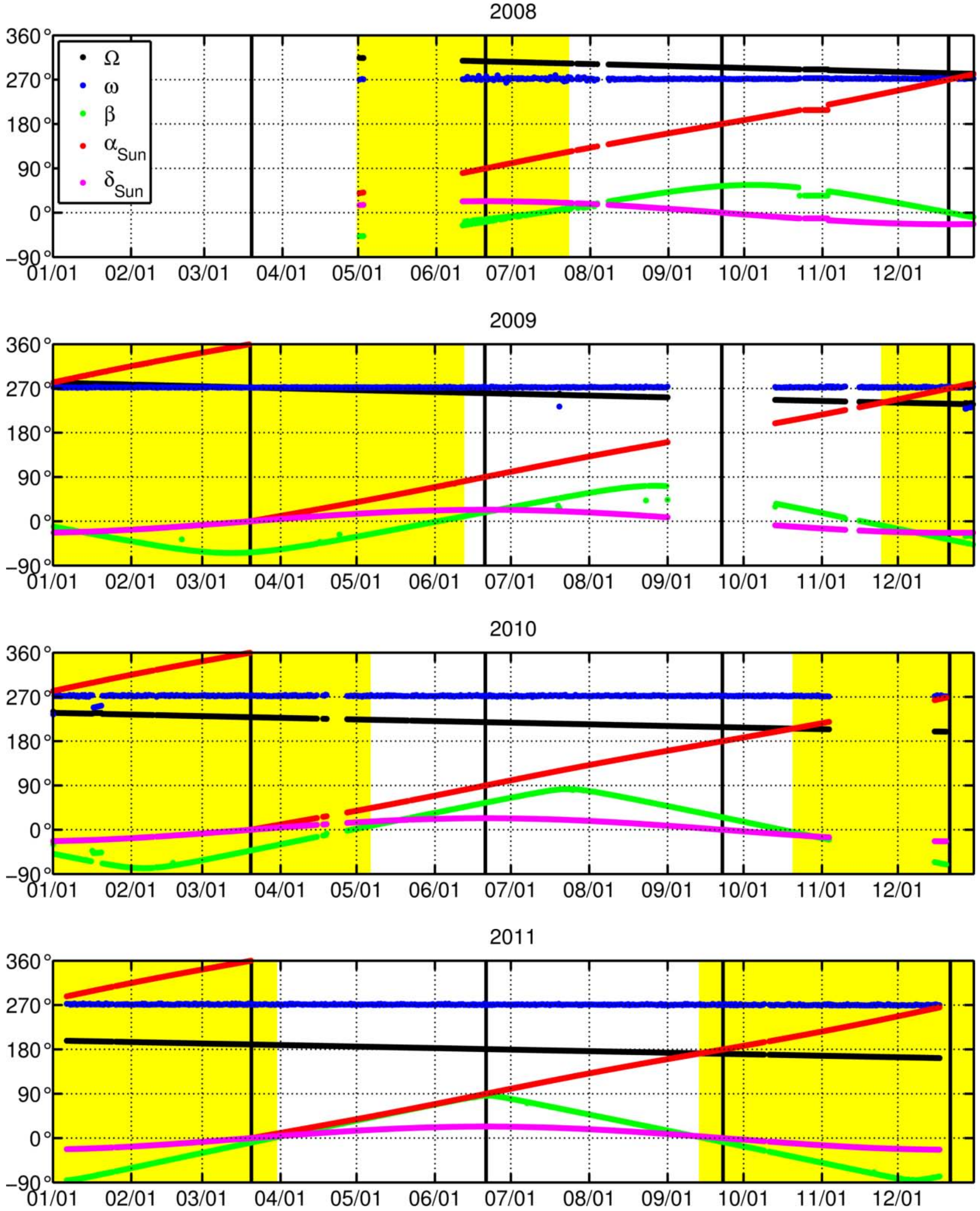

Figure 22. The longitude of the ascending node Ω (black dots), argument of perigee ω (blue dots), beta angle β (green dots), right ascension of the Sun α_{Sun}(red dots), and declination of the Sun δ_{Sun} (pink dots) for each orbit of the TWINS-1 satellite in 2008 (top) through 2011 (bottom). The 4 black vertical lines in each year mark vernal equinox, summer solstice, autumnal equinox, and winter solstice. The yellow shaded regions highlight when the orbit apogees are on the dayside of the Earth.

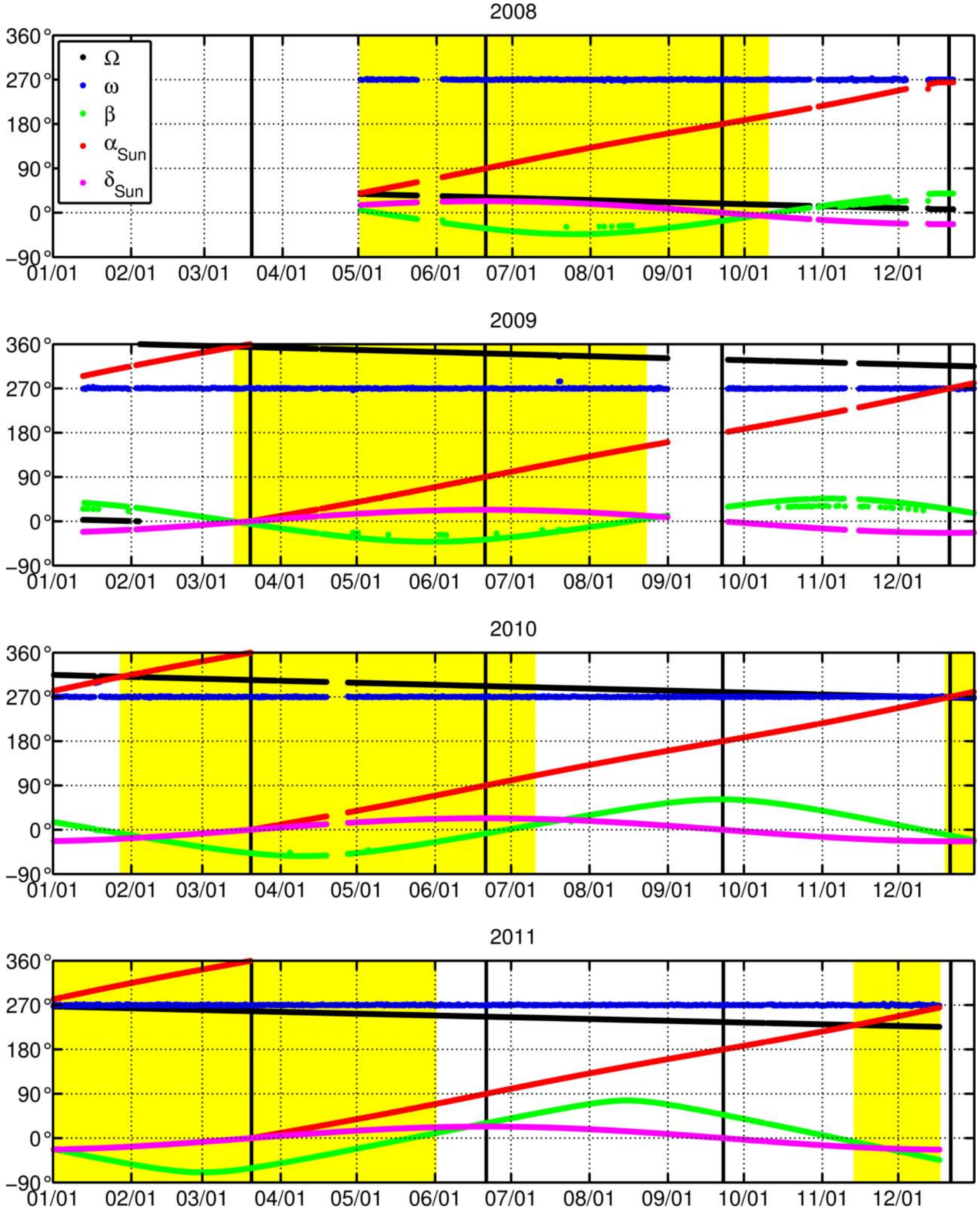

Figure 23. The longitude of the ascending node Ω (black dots), argument of perigee ω (blue dots), beta angle β (green dots), right ascension of the Sun α_{Sun}(red dots), and declination of the Sun δ_{Sun} (pink dots) for each orbit of the TWINS-2 satellite in 2008 (top) through 2011 (bottom). The 4 black vertical lines in each year mark vernal equinox, summer solstice, autumnal equinox, and winter solstice. The yellow shaded regions highlight when the orbit apogees are on the dayside of the Earth.

5.3 Data Library

LAD data was routinely downloaded from the TWINS program website (http://twins.swri.edu/) and processed into a convenient format for scientific analysis. Each downloaded packet includes four daily text files – telemetry, attitude, ephemeris, and housekeeping – for each satellite, totaling eight text files. The telemetry, attitude, and ephemeris data are recorded on Science Packet Time (SPT) that closely but not exactly matches the housekeeping data on Flight Housekeeping Time (FHT). Each line of SPT was therefore assigned the closest line (must be within 0.25 s) of FHT and merged into a single text file.

Various observational geometry and housekeeping limits are checked before an LAD measurement is classified as valid for scientific analysis and available for use in obtaining exospheric H density distributions. The observational geometry limits consist of 3 primary criteria. First, since the geocorona deviates substantially from being optically thin below a geocentric distance of 3 R_E, those measurements with a line-of-sight closest approach to the Earth, r_{LOS}, that is less than 3 R_E are excluded. Second, to mitigate possible solar contamination, only those measurements with a detector line-of-sight pointed at > 90° from the direction to the Sun are used. Third, it is required that the line-of-sight does not pass through Earth's shadow, approximated by a cylinder (with 1 R_E radius) in the antisolar direction.

The housekeeping limits are primarily associated with verifying nominal conditions for the actuator motion and LAD high voltage monitor. Additionally, LAD count rates are recorded for 0.67 and 1.33 sec in each sector, corresponding to $\Delta\omega = 2°$

and 4° of actuator rotation. It is required that the 1.33 sec measurement be between a factor of 1.8 to 2.2 of the corresponding 0.67 sec measurement.

The number of measurements with respect to the total available on each day that meet all 26 criteria were compiled. Figure 24 and Figure 25 show the percentages for each LAD on TWINS-1 and TWINS-2, respectively. The actuators on both instruments stopped rotating smoothly at the start of 2009 due to a faulty command sequence. A fix was uploaded on 21 July 2009 and the result is noticeable in both Figure 24 and Figure 25 with percentage increases on that day. The performance of the LADs on TWINS-2 degraded shortly thereafter, such that both detectors started recording very low and unrealistic values. An attempt to correct the problem occurred on 21 March 2011 when the high voltage commanding for the channel electron multipliers, on both TWINS-1 and TWINS-2, was increased from 199 V to 225 V.

In general, at least 10% of measurements are needed to obtain a global H number density distribution with three-dimensional asymmetries for any given day. However, a global fitting is only sensitive to the observed regions and therefore adequate observational coverage around the Earth is also needed to avoid artifacts in reconstructed distributions.

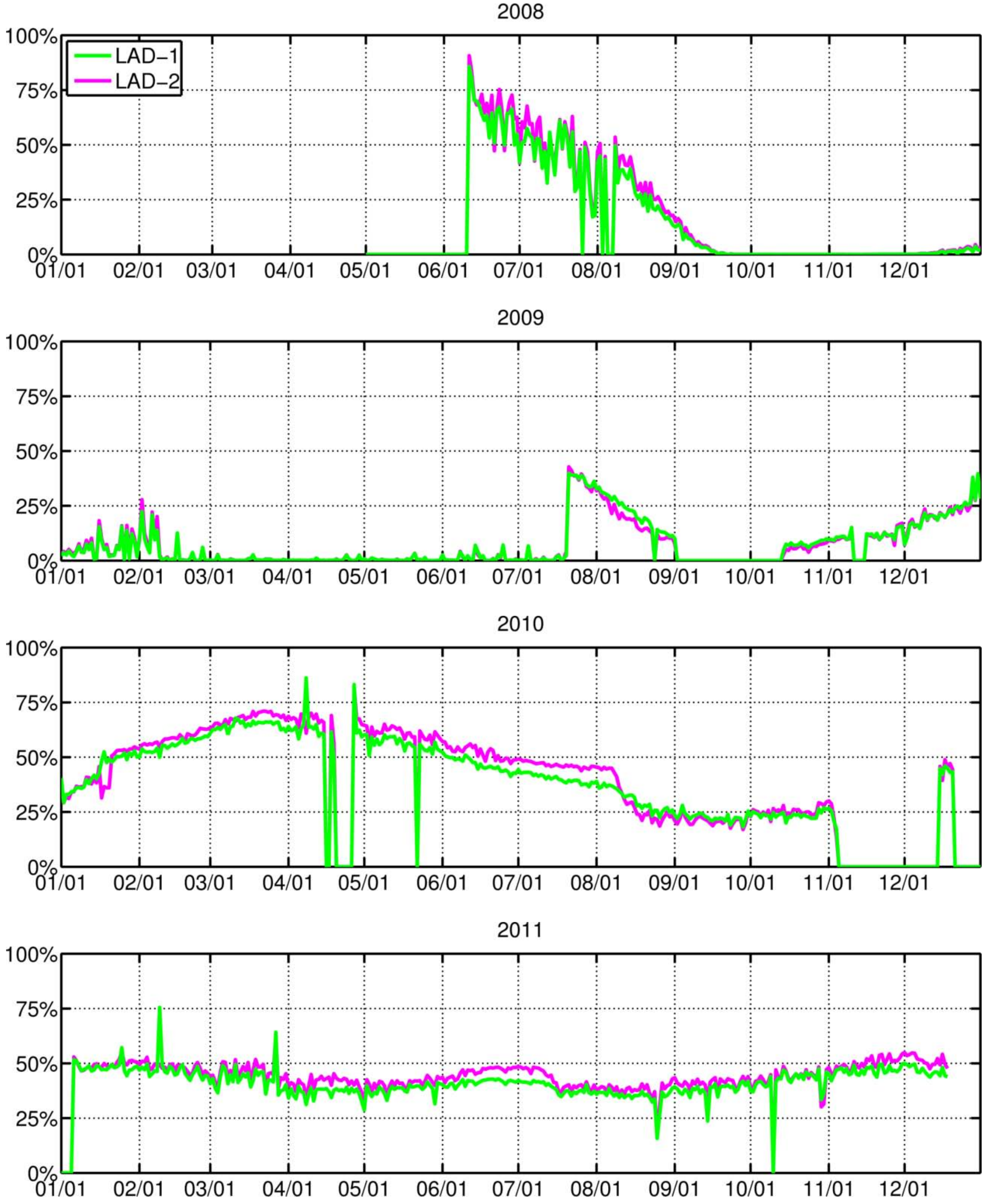

Figure 24. The percentage of TWINS-1 LAD measurements from each day in 2008 (top) through 2011 (bottom) that, based on various observational geometry and housekeeping criteria, have been classified as valid for scientific analysis and available for use in obtaining exospheric H density distributions. Note, data was unavailable for 3 weeks in September 2009.

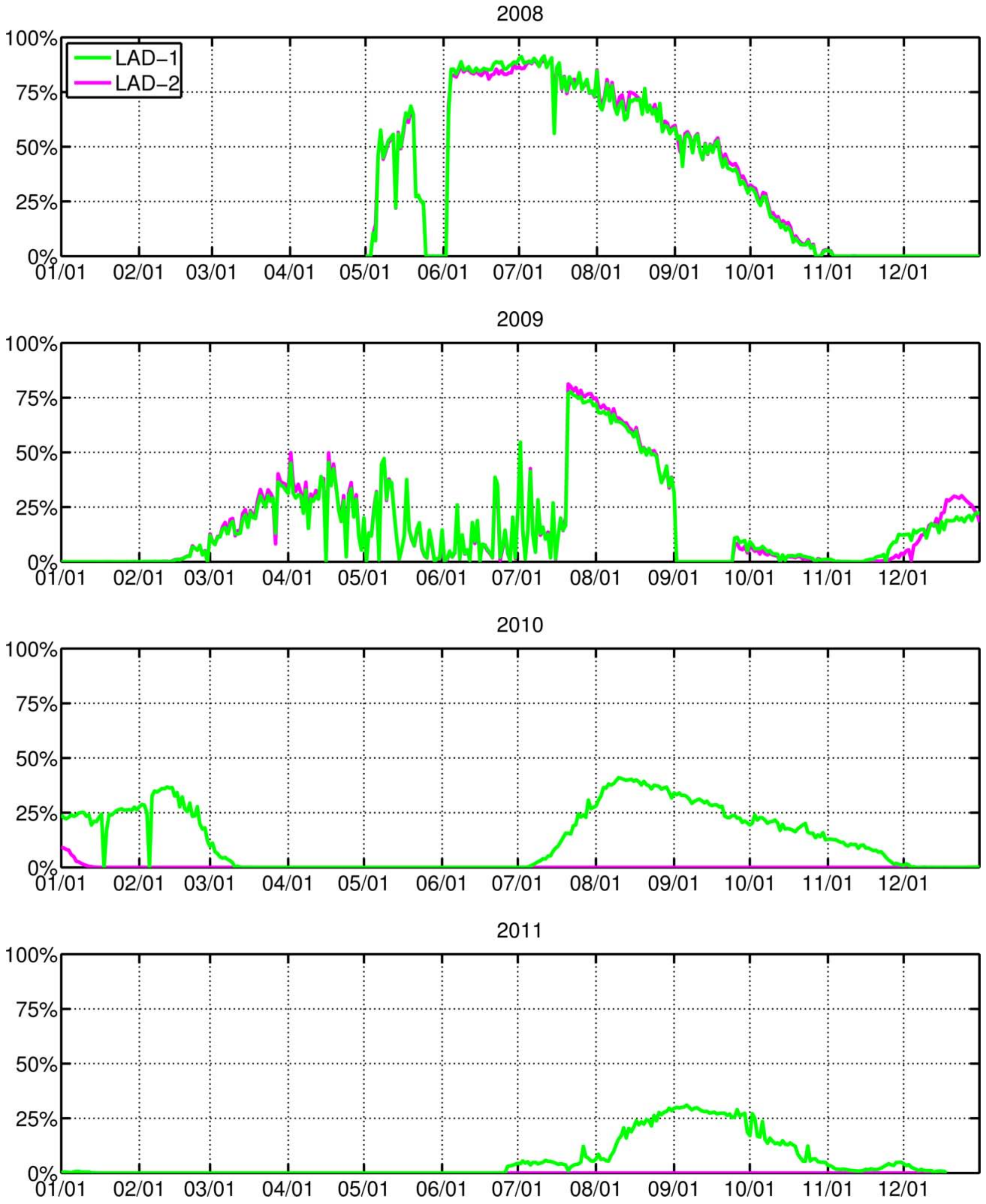

Figure 25. The percentage of TWINS-2 LAD measurements from each day in 2008 (top) through 2011 (bottom) that, based on various observational geometry and housekeeping criteria, have been classified as valid for scientific analysis and available for use in obtaining exospheric H density distributions. Note, data was unavailable for 2 weeks in September 2009.

Chapter 6: Model

The process of preparing TWINS data such that LAD measurements can be used to obtain global H density distributions with three-dimensional asymmetries requires coordinate transformations of the spacecraft position and attitude (Section 6.1 and 6.2) as well as a routine to approximate Earth's shadow (Section 6.3). A spherical harmonic expansion is used for the three-dimensional representation of exospheric H density distributions (Section 6.4). This expansion contains free parameters that are best fit to the LAD observational data using a least squares curve fitting (Section 6.5). The results of a relative cross calibration between LAD-1 and LAD-2 are applied in fittings to account for any offset in the measured intensities (Section 6.6). Finally, a distribution for an example day of 11 June 2008 is shown (Section 6.7) with a detailed error analysis (Section 6.8).

6.1 Geophysical Coordinate Systems

The TWINS program website provides attitude and ephemeris data primarily in Earth Centered Inertial (ECI) coordinates. This system is geocentric, with the x axis pointed in the direction of the vernal equinox, the z axis is parallel to Earth's rotation axis, and the y axis completes the orthogonal triad. The angles right ascension, α, and declination, δ, define a spherical coordinate system,

$$\alpha = \tan^{-1}\left(\frac{y_{ECI}}{x_{ECI}}\right), \tag{23}$$

$$\delta = \sin^{-1}\left(\frac{z_{ECI}}{\sqrt{x_{ECI}^2 + y_{ECI}^2 + z_{ECI}^2}}\right), \tag{24}$$

where $0^0 \leq \alpha \leq 180^0$ if $y_{ECI} \geq 0$, $180^0 \leq \alpha \leq 360^0$ if $y_{ECI} \leq 0$, and $-90^0 \leq \delta \leq 90^0$.

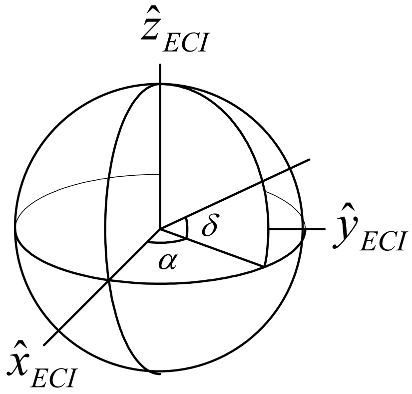

Figure 26. Angles right ascension α and declination δ defined in the Earth Centered Inertial (ECI) coordinate system.

A solar aligned coordinate system, making one complete rotation with Earth's motion around the Sun, is used to obtain global H density distributions because geocoronal symmetry along the Earth-Sun line is expected. One such system, Geocentric Equatorial Noon (GEN), has the *x* axis pointed towards the intersection of the equator and noon meridian (equatorial noon) and the *z* axis is the celestial pole; the *y* axis completes the orthogonal triad. The longitudinal angle ϕ is measured from the *x* axis in the *XY* plane and the co-latitude angle θ is counted from the z axis, such that ϕ = 0° and θ = 90° points towards equatorial noon.

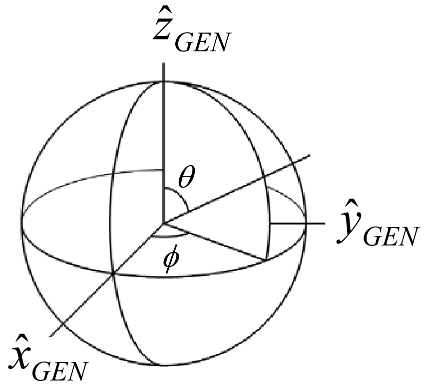

Figure 27. Longitudinal angle θ and co-latitudinal angle ϕ defined in the Geocentric Equatorial Noon (GEN) coordinate system.

A second system, Geocentric Solar Ecliptic (GSE), was used to obtain the TWINS simplified operational exospheric model for solar minimum conditions (Section 7.4) because it is more convenient than GEN for ENA modelers. This system has the x axis pointed to the Sun, the z axis is the ecliptic pole, and the y axis completes the orthogonal triad. The longitudinal angle θ and the co-latitudinal angle ϕ are defined in the same way as for GEN shown in Figure 27.

The Interplanetary glow maps are provided in Earth Centered Ecliptic (ECE) coordinates, where the x axis is pointed towards the vernal equinox and the z axis is the ecliptic pole; the y axis completes the orthogonal triad (Figure 28). Ecliptic longitude λ and ecliptic latitude β are determined in the same way that right ascension α and declination δ are calculated in ECI coordinates (Equations 23 and 24).

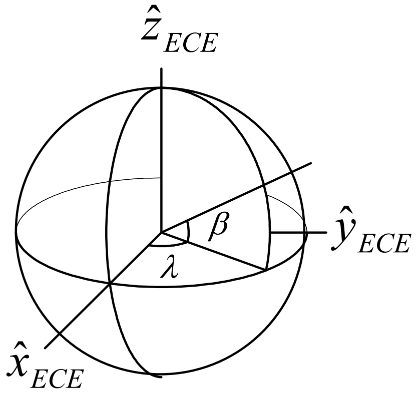

Figure 28. The ecliptic longitude λ and ecliptic latitude β defined in the Earth Centered Ecliptic (ECE) coordinate system.

6.1.1 ECI to GEN

The coordinate transformation from ECI to GEN requires only one rotation to account for Earth's motion around the Sun,

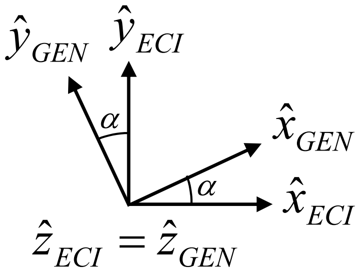

Figure 29. Rotation about the angle right ascension, α, required to transform from ECI to GEN.

$$\begin{bmatrix} x \\ y \\ z \end{bmatrix}_{GEN} = \begin{bmatrix} \cos\alpha & \sin\alpha & 0 \\ -\sin\alpha & \cos\alpha & 0 \\ 0 & 0 & 1 \end{bmatrix} \begin{bmatrix} x \\ y \\ z \end{bmatrix}_{ECI}, \tag{25}$$

where α is the right ascension.

6.1.2 ECI to GSE

The direction of the ecliptic pole ($\hat{z}_{GSE}$) is nearly constant in the ECI system,

$$\hat{z}_{GSE} = \hat{\psi} = -sin\psi\ \hat{y}_{ECI} + cos\psi\ \hat{z}_{ECI}\ , \tag{26}$$

where a constant value is used for Earth's obliquity, ψ = 23.44°.

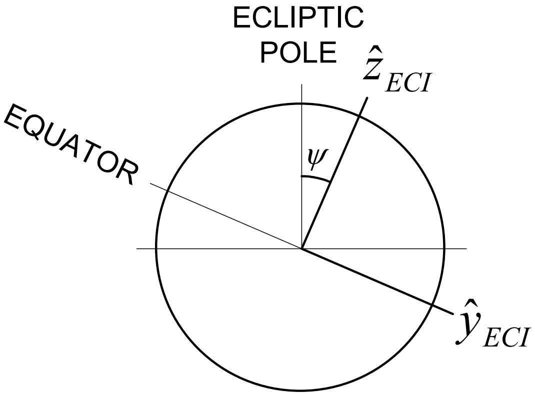

Figure 30. The transformation from ECI to GSE coordinates includes a rotation about the ecliptic pole ($\hat{z}_{GSE}$), which is fixed in the ECI system.

The conversion from ECI to GSE coordinates can be expressed in a transformation matrix [*Kivelson and Russell*, 1995],

$$\begin{bmatrix} x \\ y \\ z \end{bmatrix}_{GSE} = \begin{bmatrix} \hat{S}_1 & \hat{S}_2 & \hat{S}_3 \\ \hat{y}_1 & \hat{y}_2 & \hat{y}_3 \\ \hat{\psi}_1 & \hat{\psi}_2 & \hat{\psi}_3 \end{bmatrix} \begin{bmatrix} x \\ y \\ z \end{bmatrix}_{ECI} , \tag{27}$$

where $\hat{S}$ is the solar unit vector, $\hat{\psi}$ is the direction of the ecliptic pole, and $\hat{y}$ completes the orthogonal triad,

$$\hat{y} = \hat{\psi} \times \hat{S} \ . \tag{28}$$

6.1.3 ECI to ECE

The coordinate transformation from ECI to ECE requires only one rotation from the equatorial to the ecliptic plane about their common *x* axis,

$$\begin{bmatrix} x \\ y \\ z \end{bmatrix}_{ECE} = \begin{bmatrix} 1 & 0 & 0 \\ 0 & \cos\psi & -\sin\psi \\ 0 & \sin\psi & \cos\psi \end{bmatrix} \begin{bmatrix} x \\ y \\ z \end{bmatrix}_{ECI} , \tag{29}$$

where a constant value is used for Earth’s obliquity, $\psi = 23.44°$.

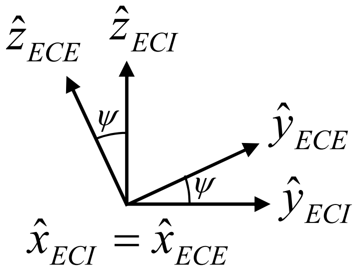

Figure 31. The rotation about Earth's obliquity, ψ, required to transform from ECI to ECE.

6.2 LAD Line-of-sight Determination

Spacecraft pointing is provided as two unit vectors, polar ($\hat{p}$) and azimuthal ($\hat{a}$), and

$$\hat{z} = \hat{p} \times \hat{a} \tag{30}$$

is calculated to complete the orthogonal triad.

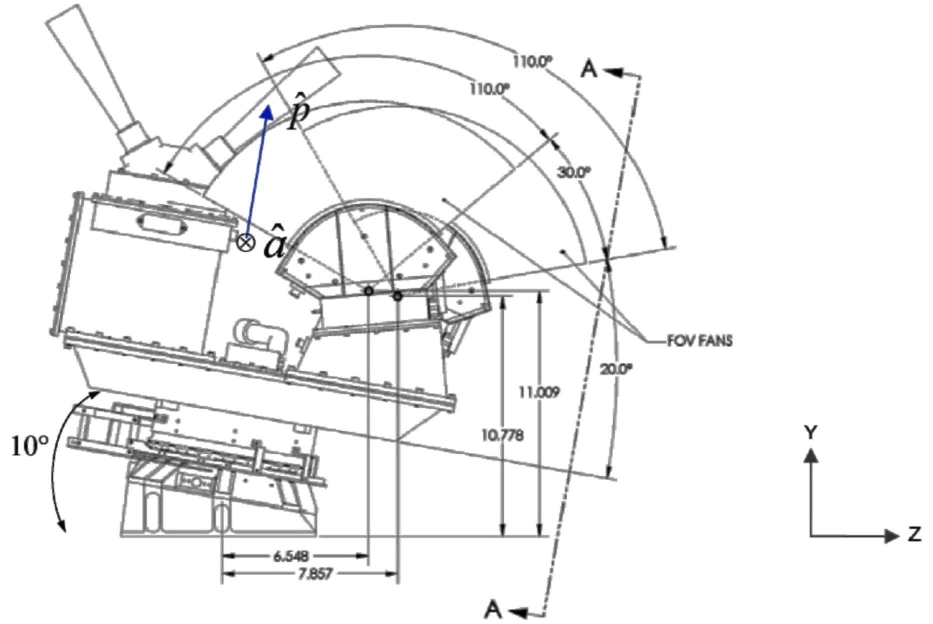

Figure 32. A side view of the TWINS instrument with the polar ($\hat{p}$) and azimuthal ($\hat{a}$) directions (Instrument Specification Document, March 2008).

With respect to the instrument frame, $\hat{p}$, $\hat{a}$, and $\hat{z}$, two rotations are required to determine each LAD line-of-sight unit vector. First, a rotation about the polar vector by the actuator angle, ω, is performed,

$$\hat{a}_\omega = \cos\omega\,\hat{a} - \sin\omega\,\hat{z}\,, \tag{31}$$

$$\hat{z}_\omega = \sin\omega\,\hat{a} + \cos\omega\,\hat{z}\,, \tag{32}$$

such that an actuator frame is defined, which can be expressed in terms of a rotation matrix,

$$\begin{bmatrix} \hat{p} \\ \hat{a} \\ \hat{z} \end{bmatrix}_{\omega} = \begin{bmatrix} 1 & 0 & 0 \\ 0 & \cos\omega & -\sin\omega \\ 0 & \sin\omega & \cos\omega \end{bmatrix} \begin{bmatrix} \hat{p} \\ \hat{a} \\ \hat{z} \end{bmatrix}. \tag{33}$$

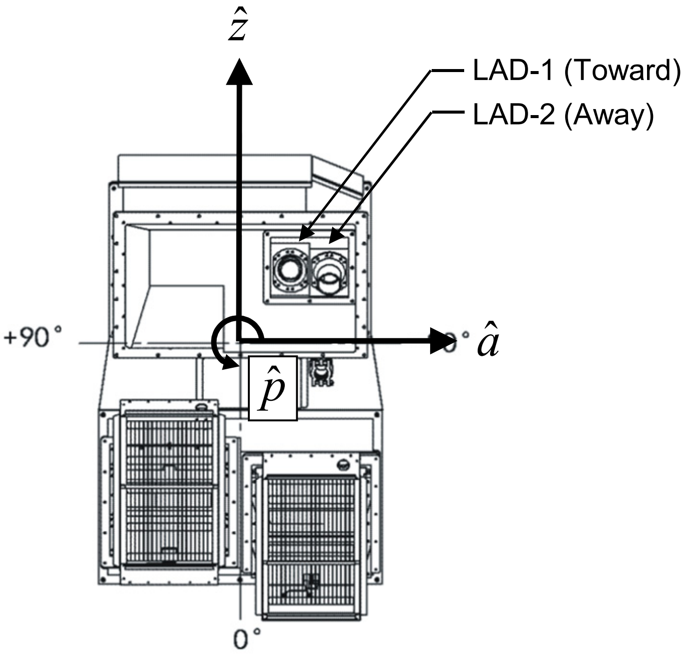

Figure 33. Top view of the TWINS instrument frame, $\hat{p}$, $\hat{a}$, and $\hat{z}$. The Toward and Away directions are defined for the ENA sensor heads that look toward or away from the electronics box. The LADs are named in a similar respect to be consistent with the ENA sensor head directions. For example, the LAD sensor head that looks predominately in the direction of the ENA Toward is termed the LAD Toward, also known as LAD-1 (adapted from the Instrument Specification Document, March 2008).

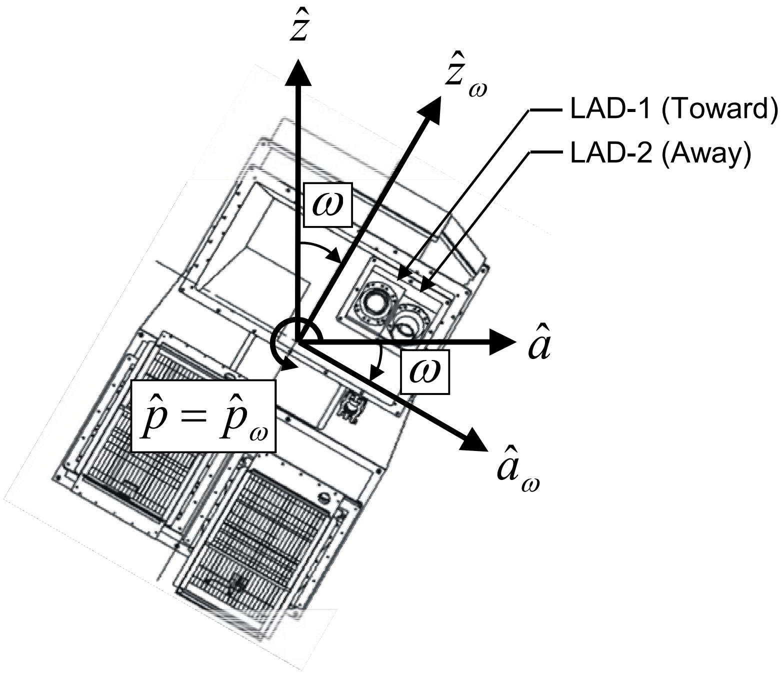

Figure 34. Top view of TWINS showing the rotation about the actuator angle ω from the instrument frame ($\hat{p}$, $\hat{a}$, $\hat{z}$) to the actuator frame ($\hat{p}_\omega$, $\hat{a}_\omega$, $\hat{z}_\omega$) (adapted from the Instrument Specification Document, March 2008).

Second, to obtain the LAD boresight unit vectors, $\hat{L}_1$ and $\hat{L}_2$, a rotation about $\hat{a}_\omega$ by ±40° is performed,

$$\hat{L}_1 = \cos 40^0\, \hat{p}_\omega + \sin 40^0\, \hat{z}_\omega \,, \tag{34}$$

$$\hat{L}_2 = \cos 40^0\, \hat{p}_\omega - \sin 40^0\, \hat{z}_\omega \,, \tag{35}$$

shown in Figure 35.

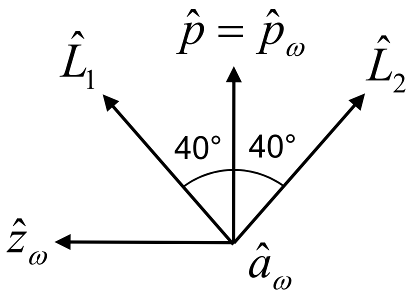

Figure 35. The LAD boresights are fixed in the actuator frame ($\hat{p}_\omega$, $\hat{a}_\omega$, $\hat{z}_\omega$) by a rotation of ±40° about $\hat{a}_\omega$.

The above transformations (Equations 31 – 35) can be combined into a product of rotation matrices,

$$\begin{bmatrix} x \\ y \\ z \end{bmatrix}_{GEN/GSE} = \begin{bmatrix} \hat{p}_x & \hat{p}_y & \hat{p}_z \\ \hat{a}_x & \hat{a}_y & \hat{a}_z \\ \hat{z}_x & \hat{z}_y & \hat{z}_z \end{bmatrix}^{-1} \begin{bmatrix} 1 & 0 & 0 \\ 0 & cos\,\omega & -sin\,\omega \\ 0 & sin\,\omega & cos\,\omega \end{bmatrix}^{-1} \left(\begin{bmatrix} cos\,40° \\ 0 \\ sin\,40° \end{bmatrix} and \begin{bmatrix} cos\,40° \\ 0 \\ -sin\,40° \end{bmatrix} \right). \tag{36}$$

The geocentric distance of an LAD line-of-sight closest approach to the Earth, r_{LOS}, is determined in two steps. The angle η between the LAD line-of-sight, $\vec{L}$, and spacecraft position vector, $\vec{r}_{S/C}$, is calculated,

$$\eta = \cos^{-1}\left(\hat{L} \circ -\hat{r}_{S/C}\right), \tag{37}$$

and finally

$$r_{LOS} = r_{S/C} \sin \eta \,. \tag{38}$$

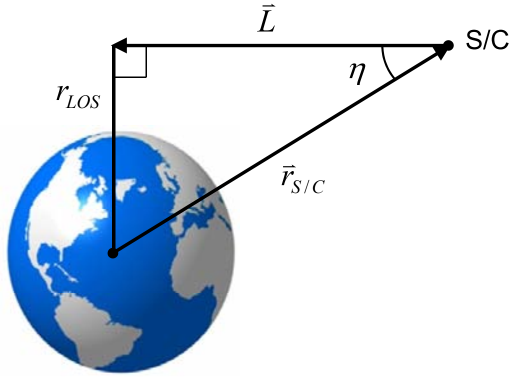

Figure 36. The observational geometry used to calculate the geocentric distance of an LAD line-of-sight closest approach to the Earth, r_{LOS}. The angle η is between the LAD line-of-sight, $\vec{L}$, and the spacecraft position, $\vec{r}_{S/C}$.

The variable r_{LOS}, which represents the closest approach to the Earth where H densities are highest along a typical LAD line-of-sight, opens a way of characterizing the observed Lyman-α intensities. Figure 37 shows the LAD-1 and LAD-2 measurements on TWINS-1 for 11 June 2008, as an example. The width of each curve is in part a result of geocoronal asymmetry over the observed regions.

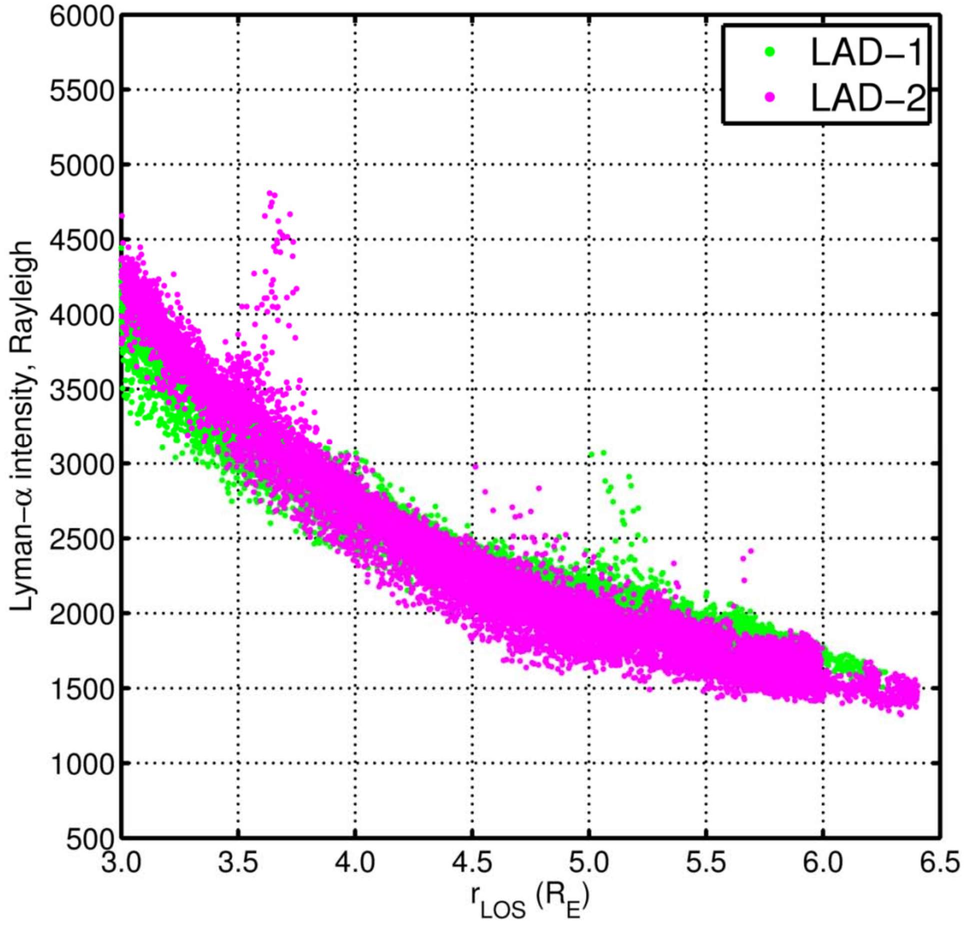

Figure 37. The Lyman-α intensity in rayleighs observed by both LAD-1 (green dots) and LAD-2 (pink dots) on TWINS-1 for 11 June 2008 versus the geocentric distance of each line-of-sight closest approach to the Earth, r_{LOS}.

Figure 38 shows another example of LAD-1 and LAD-2 measurements observed on 20 June 2008.

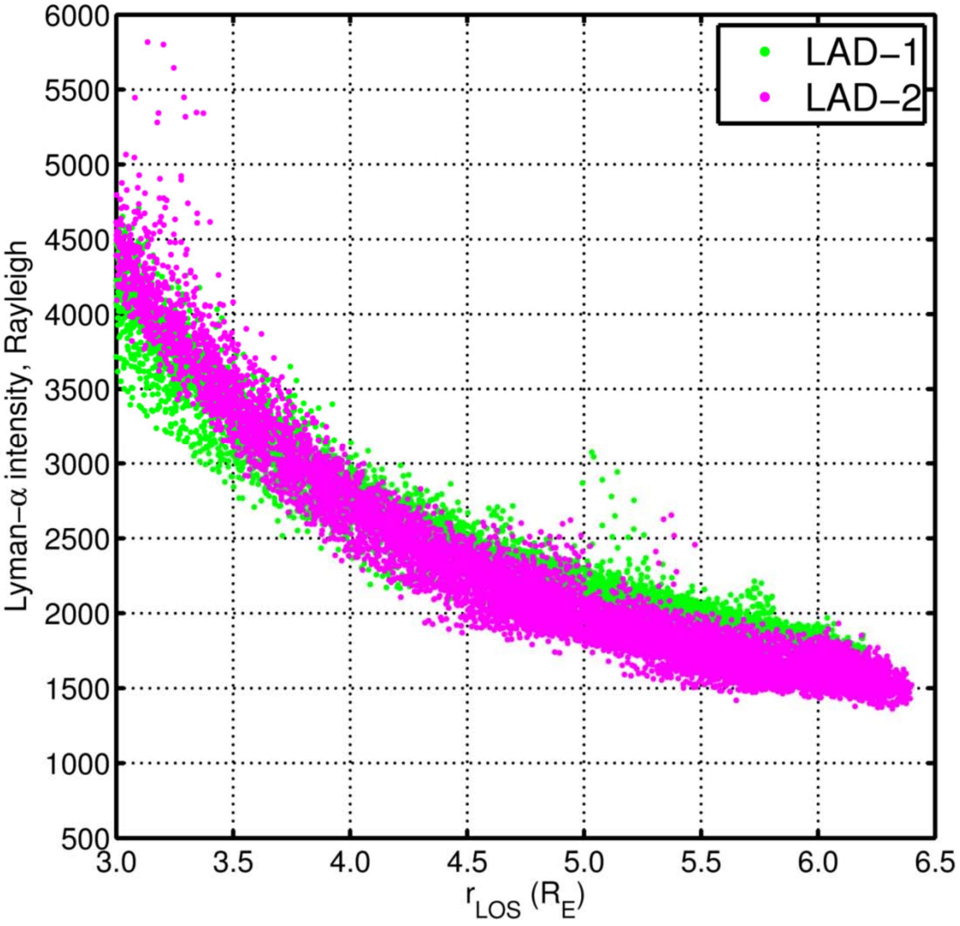

Figure 38. The Lyman-α intensity observed by both LAD-1 (green dots) and LAD-2 (pink dots) on TWINS-1 for 20 June 2008 versus the geocentric distance of each line-of-sight closest approach to the Earth, r_{LOS}.

The LADs are sensitive to certain classes of stars, specifically O and B, that have prominent hydrogen emissions in Lyman-α. Consequently, star sightings can be used to validate detector pointing. An example of this capability was performed using LAD measurements from TWINS-1 on 16 June 2008. Figure 39 shows that LAD-2 repeatedly registered a higher signal at certain times while the actuator was sweeping back and forth through the windshield wiper motion ($\Delta\omega$ ± 90°).

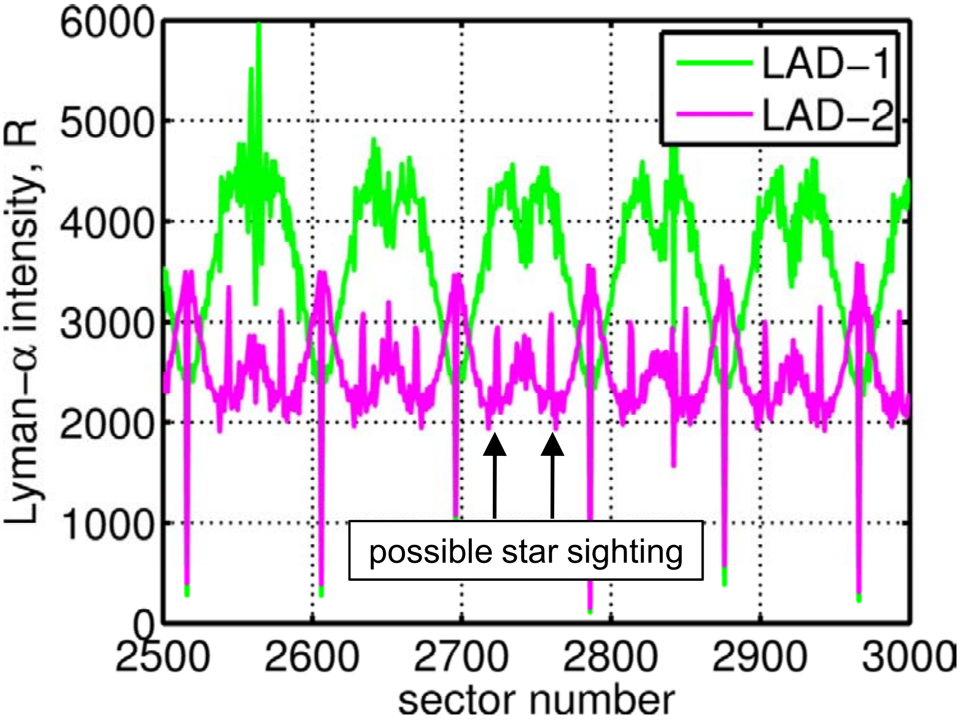

Figure 39. A sequence of LAD-1 (green) and LAD-2 (pink) measurements from TWINS-1 on 16 June 2008 that includes a possible star sighting. The horizontal axis is the sector number for the day and the vertical axis is the measured Lyman-α intensity in rayleighs.

The brightest star in the constellation Virgo, Spica (α Virginis), was within the LAD-2 field of view (Figure 40) at the times of increased Lyman-α intensities. Spica has an apparent magnitude of +0.96 and spectral type of B1.

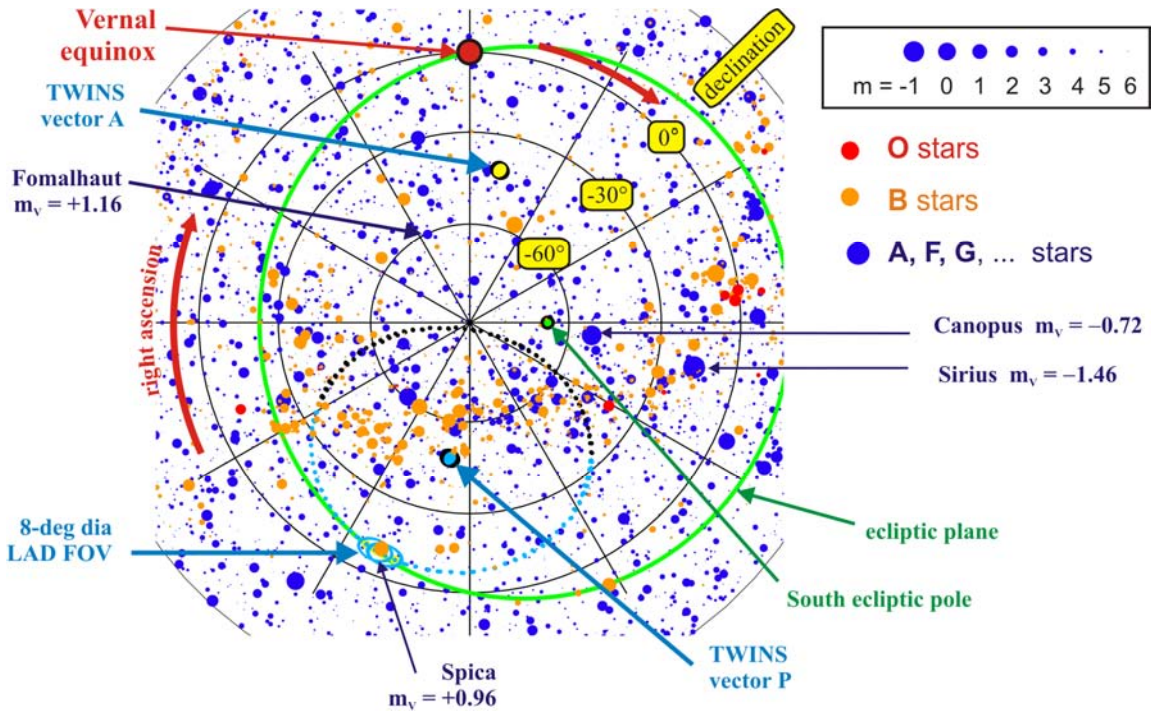

Figure 40. A sky map with the spectral classes of stars in the Southern Hemisphere. The dotted circle around the polar vector ($\hat{p}$) are the lines-of-sight for LAD-1 (dark blue) and LAD-2 (light blue) for one rotation of the actuator.

6.3 Earth's Shadow Approximation

Only LAD lines-of-sight that do not pass through Earth's shadow, approximated by a cylinder (with 1 R_E radius) in the antisolar direction (Figure 41), are used to obtain exospheric H density distributions. A routine to determine the minimum distance between two skew lines is used to find the minimum distance from a vector in the antisolar direction, $-\vec{S}$, to each LAD line-of-sight, $\vec{L}$. First, the infinite line distance, *l*, is obtained using the relationship

$$l = \left| (L_0 - S_0) + \frac{(be - cd)\hat{L} - (ae - bd)\hat{S}}{ac - b^2} \right|, \tag{39}$$

where L_0 is the spacecraft position, S_0 is the center of the Earth, $a = \hat{L} \cdot \hat{L}$, $b = \hat{S} \cdot \hat{L}$, $c = \hat{S} \cdot \hat{S}$, $d = \hat{n} \cdot \hat{n}$, and $e = \hat{s} \cdot \hat{n}$. If $l < 1$ R_E, the location of the minimum distance on each vector,

$$L_c = \frac{be - cd}{ac - b^2}, \tag{40}$$

$$S_c = \frac{ae - bd}{ac - b^2}, \tag{41}$$

must be checked such that $L_c > 0$ and $S_c > 0$. If both conditions are met, then the line-of-sight is flagged as passing through Earth's shadow. The requirement that lines-of-sight do not pass through earth shadow typically excludes less than 2% of LAD measurements for any given orbit.

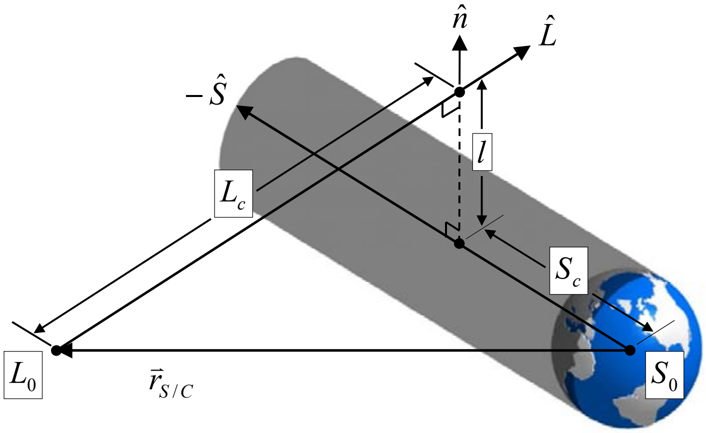

Figure 41. The observational geometry used to approximate Earth's shadow as a cylinder. The variables L_0 and S_0 are the spacecraft and Earth positions, respectively. The variable L_c is the distance along the LAD line-of-sight, $\hat{L}$, and the variable S_c is the distance along the antisolar direction, $-\hat{S}$, where the minimum distance between the two lines, l, occurs along the unit vector $\hat{n}$.

6.4 3D Representation of Exospheric H Density Distributions

Hodges [1994] modeled exospheric H number density distributions, $n_H(r, \phi, \theta)$, by a third-order spherical harmonic expansion in the form

$$n_H(r, \phi, \theta) = N(r)\sqrt{4\pi}\sum_{l=0}^{3}\sum_{m=0}^{l}(A_{lm}(r)\cos(m\phi) + B_{lm}(r)\sin(m\phi))Y_{lm}(\theta)\,, \tag{42}$$

where $N(r)$ is the radial function; $A_{lm}(r)$ and $B_{lm}(r)$ are the radius-dependent coefficients of the expansion; and $Y_{lm}(\theta)$ are the spherical harmonic Legendre functions

$$Y_{00} = \sqrt{\frac{1}{4\pi}} \tag{43}$$

$$Y_{10} = \sqrt{\frac{3}{4\pi}}\cos(\theta) \tag{44}$$

$$Y_{11} = -\sqrt{\frac{3}{4\pi}}sin(\theta) \tag{45}$$

$$Y_{20} = \sqrt{\frac{5}{4\pi}}\left(\frac{3}{2}cos^2(\theta) - \frac{1}{2}\right) \tag{46}$$

$$Y_{21} = -\sqrt{\frac{15}{8\pi}}in(\theta)cos(\theta) \tag{47}$$

$$Y_{22} = \frac{1}{4}\sqrt{\frac{15}{2\pi}}sin^2(\theta) \tag{48}$$

$$Y_{30} = \sqrt{\frac{7}{4\pi}}\left(\frac{5}{2}\cos^3(\theta) - \frac{3}{2}cos(\theta)\right) \tag{49}$$

$$Y_{31} = -\frac{1}{4}\sqrt{\frac{21}{4\pi}}\sin(\theta)\,(5\cos^2(\theta) - 1) \tag{50}$$

$$Y_{32} = \frac{1}{4}\sqrt{\frac{105}{2\pi}} sin^2(\theta)\cos(\theta) \tag{51}$$

$$Y_{33} = -\frac{1}{4}\sqrt{\frac{35}{4\pi}} sin^3(\theta) \tag{52}$$

with excluded imaginary parts. He divided the geocentric distance *r* into 40 steps, which resulted in a total of 640 free parameters. Considering only the observational geometry limit with r_{LOS} > 3 R_E reduces the number of free parameters to 96. This number of free parameters is still computationally impractical for a curve fitting procedure. *Nass et al.* [2006] suggested important simplifications — the Bonn model — that reduced the number of free parameters to 12. First, they reduced the order of the expansion, *l*, from 3 to 2. Second, they approximated the mean density, $N(r)$, by a power law

$$N(r) = pr^{-k} \,. \tag{53}$$

Finally, for $A_{lm}(r)$ a linear approximation was used

$$A_{lm}(r) = a_{lm} + b_{lm}r \,, \tag{54}$$

and all $B_{lm}(r)$ were set to zero. Computer simulations [*Nass et al.*, 2006] showed that the Bonn model was able to conveniently reproduce major features of the *Hodges* [1994] model.

This work expands the Bonn model in an important way by adding $B_{lm}(r)$ as free parameters, using a linear approximation

$$B_{lm}(r) = c_{lm} + d_{lm} r \,, \tag{55}$$

which would open the opportunity to account for dawn-dusk asymmetry in the distribution, impossible if $B_{lm}(r) = 0$. This addition increases the number of free parameters to 18, compared to 12 in the Bonn model.

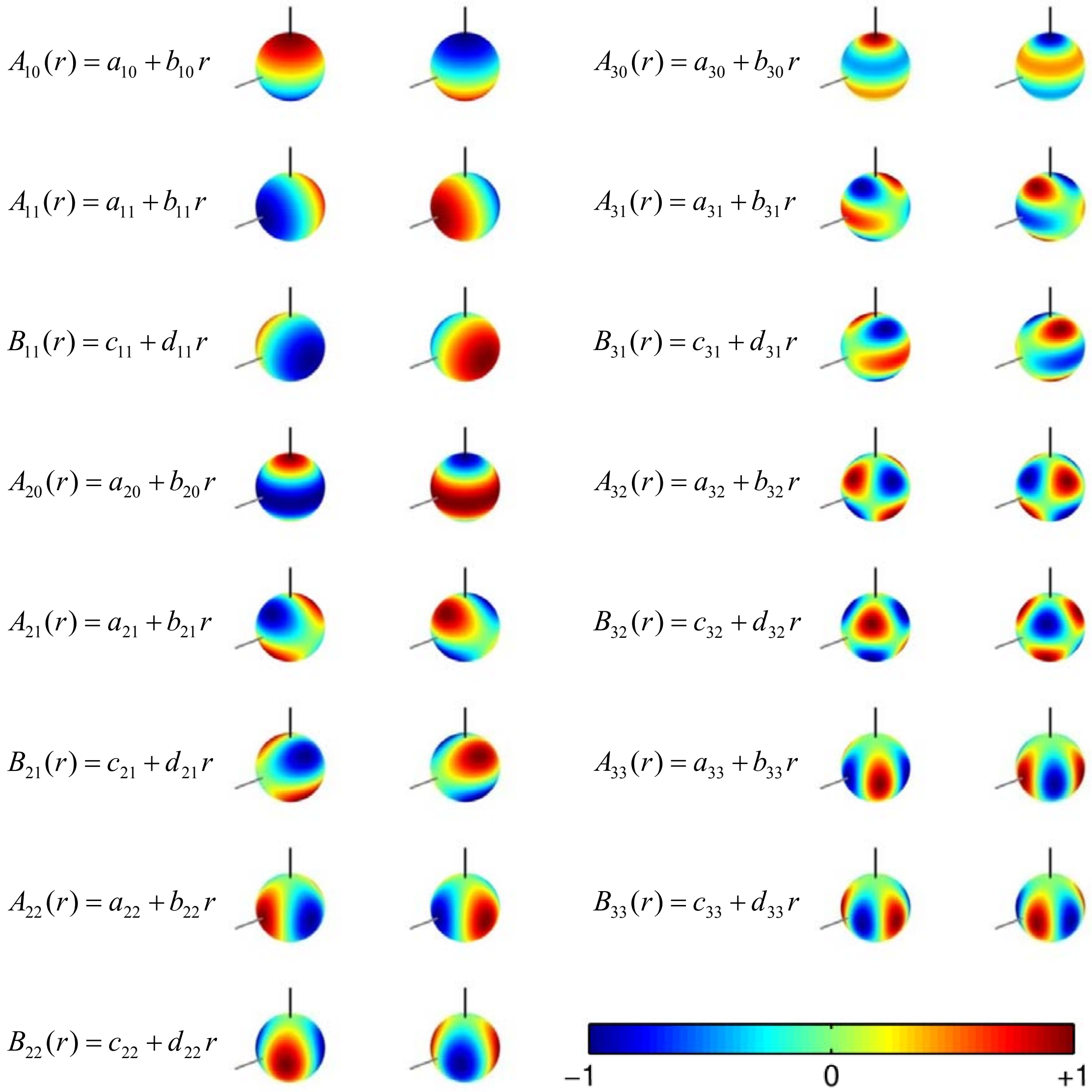

Figure 42. Three-dimensional color plots of the asymmetry introduced for positive (left) and negative (right) values of each expansion coefficient with respect to an *x* axis (gray line) and *z* axis (black line). Setting a particular coefficient to zero during the fitting procedure eliminates the possibility for the corresponding asymmetry in the obtained three-dimensional H density distribution.

6.5 Least Squares Curve Fitting Procedure

A process of forward modeling starts with an analytical expression for the three-dimensional H number density distribution. This expression contains free parameters that are best fit to the observational data using a least squares curve fitting. The solution to the fitting minimizes the sum of squared residuals,

$$min \sum_{i} (C_a - C_f)^2 , \tag{56}$$

where a residual is the difference between an observed intensity (C_a) and corresponding fitted intensity provided by the model (C_f). The Levenberg-Marquardt algorithm [*Levenberg*, 1944; *Marquardt*, 1963; *Coleman and Li*, 1994, 1996], which interpolates between the Gauss-Newton algorithm and the method of gradient descent, is used such that in each iteration step the fitting parameters $\boldsymbol{P} = (p, k, a_{lm}, b_{lm}, c_{lm}, d_{lm})$ are replaced by new estimates, $\boldsymbol{P} + \boldsymbol{\delta}$. To determine $\boldsymbol{\delta}$, the functions $f(x_i, \boldsymbol{P} + \boldsymbol{\delta})$ are approximated by their linearizations,

$$f(x_i, \boldsymbol{P} + \boldsymbol{\delta}) \approx f(x_i, \boldsymbol{P}) + J_i \boldsymbol{\delta} , \tag{57}$$

where $J_i = \partial f(x_i, \boldsymbol{P}) / \partial \boldsymbol{P}$ is the gradient of f with respect to $\boldsymbol{P}$. The sum of squares becomes

$$\sum_i (y_i - f(x_i, \boldsymbol{P}) - J_i \boldsymbol{\delta})^2 , \tag{58}$$

or in vector notation,

$$\| \boldsymbol{y} - \boldsymbol{f}(\boldsymbol{\delta}) - \boldsymbol{J}\boldsymbol{\delta} \|^2 . \tag{59}$$

Taking the derivative with respect to $\boldsymbol{\delta}$ of Equation 59 and setting the result to zero gives

$$(\boldsymbol{J}^T \boldsymbol{J})\boldsymbol{\delta} = \boldsymbol{J}^T [\boldsymbol{y} - \boldsymbol{f}(\boldsymbol{\delta})] , \tag{60}$$

which is the Gauss-Newton algorithm. The Levenberg-Marquardt algorithm introduces a (non-negative) damping factor, λ, that is adjusted at each iteration,

$$(\boldsymbol{J}^T \boldsymbol{J} + \lambda \boldsymbol{I})\boldsymbol{\delta} = \boldsymbol{J}^T [\boldsymbol{y} - \boldsymbol{f}(\boldsymbol{\delta})] , \tag{61}$$

such that if the reduction in the sum of squares is rapid, a smaller value of λ is used bringing the algorithm closer to the Gauss-Newton algorithm. Alternatively, if an iteration results in minimal reduction, λ is increased bringing the algorithm closer to the method of gradient descent. Each component of the gradient is scaled according to the curvature by replacing the identity matrix, $\boldsymbol{I}$, on the left hand side of Equation 61 with

$\boldsymbol{diag}(\boldsymbol{J}^T\boldsymbol{J})$, which results in larger movement along directions where the gradient is smaller. Formally, the Levenberg-Marquardt algorithm is

$$\left(\boldsymbol{J}^T\boldsymbol{J} + \lambda\, \boldsymbol{diag}(\boldsymbol{J}^T\boldsymbol{J})\right)\boldsymbol{\delta} = \boldsymbol{J}^T[\boldsymbol{y} - \boldsymbol{f}(\boldsymbol{\delta})]\,. \tag{62}$$

Table 2 lists the initial and boundary values used in the fitting procedure. Initial parameter values are selected at the start to be equidistant from the lower and upper boundaries. The boundary conditions are chosen to far exceed, by a factor of 10, values that would be expected in obtaining exospheric H number densities.

Table 2: Initial and boundary values for the least squares curve fitting parameters $(p, k, a_{lm}, b_{lm}, c_{lm}, d_{lm})$; n_H is in cm^{-3} and r is in R$_E$.

Parameter	Initial Value	Lower Bound	Upper Bound
p	10^4	10^3	10^5
k	-3	-1	-5
$a_{lm}, b_{lm}, c_{lm}, d_{lm}$	0	-10^4	10^4

First, the simple r-dependent spherically symmetric density profile, $N(r) = pr^{-k}$, is fit, using the method of nonlinear least squares, with the 16 angular coefficients $(a_{lm}, b_{lm}, c_{lm}, d_{lm})$ set to zero. Second, once p and k have been obtained, their values are set and another fit is performed to obtain the angular coefficients.

Next, a new fit for p and k is conducted using the first pass values for the angular dependence coefficients. The new values for p and k are then used in another fit for a_{lm}, b_{lm}, c_{lm}, and d_{lm}, completing the second pass. The process was tested in an iterative fashion and one pass is usually sufficient to obtain the coefficients with accuracies better than 1%. A typical fit consists of around 10000 measurements and takes between 4 to 6 hours to converge on a solution.

6.6 Relative Cross Calibration of the LADs

As discussed in Section 5.2, each TWINS instrument is located on a platform that rotates about a nominally nadir-pointed axis, in a windshield wiper motion, back and forth through overlapping angular limits $\Delta\omega = \pm 99°$ (Figure 1). When the platform reaches $\omega = \pm 90°$, LAD-1 points in the same direction as LAD-2 in the opposite orientation, and vice versa, which opens a possibility for cross calibration. This capability is important to verify that the detectors are operating normally.

The LADs on TWINS-1 registered nearly the same cross calibration signals through 2008, but eventually LAD-1 started recording systematically lower Lyman-α intensities than LAD-2 for select time periods. Figure 43 shows LAD-1 ($\omega = -90°$) and LAD-2 ($\omega = 90°$) measurements for both TWINS-1 orbits on 6 August 2011, as an example.

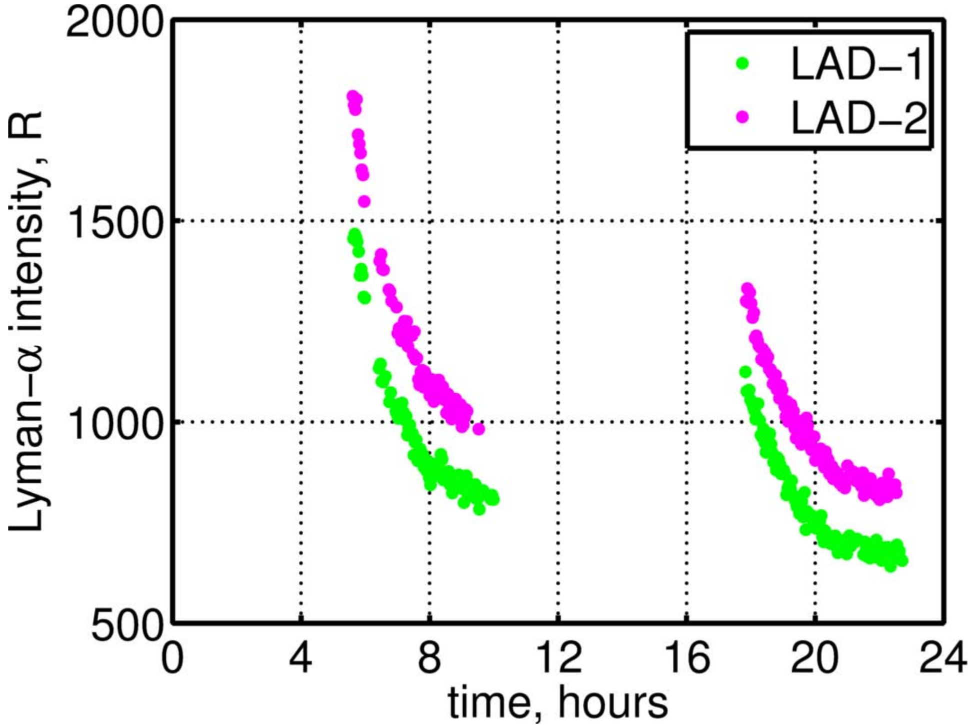

Figure 43. LAD-1 (green dots) and LAD-2 (pink dots) measured Lyman-α intensities at ω = -90°and ω = 90°, respectively, for both TWINS-1 orbits on 6 August 2011.

The difference between LAD-1 and LAD-2 measured intensities at the cross calibration orientations on 6 August 2011 is reflected in all measurements from that day, as shown in Figure 44

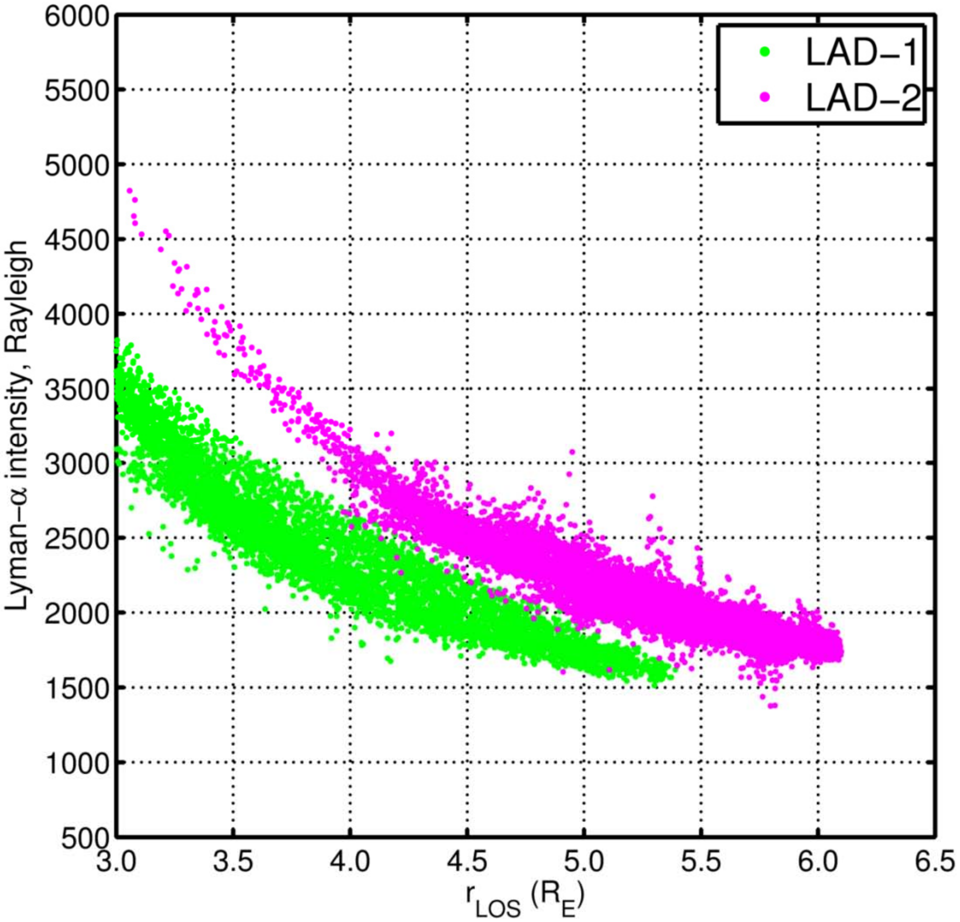

Figure 44. The Lyman-α intensity observed by both LAD-1 (green dots) and LAD-2 (pink dots) on TWINS-1 for 6 August 2011 versus the geocentric distance of each line-of-sight closest approach to the Earth, r_{LOS}.

The ratio between LAD-1 to LAD-2 measured intensities at the cross calibration orientations was calculated to be 0.80 for 6 August 2011. Figure 45 shows LAD-1 (ω = -90°) and LAD-2 (ω = 90°) measurements for both TWINS-1 orbits on 6 August 2011 with LAD-1 intensities that have been increased by a factor of 1 / 0.80 = 1.25.

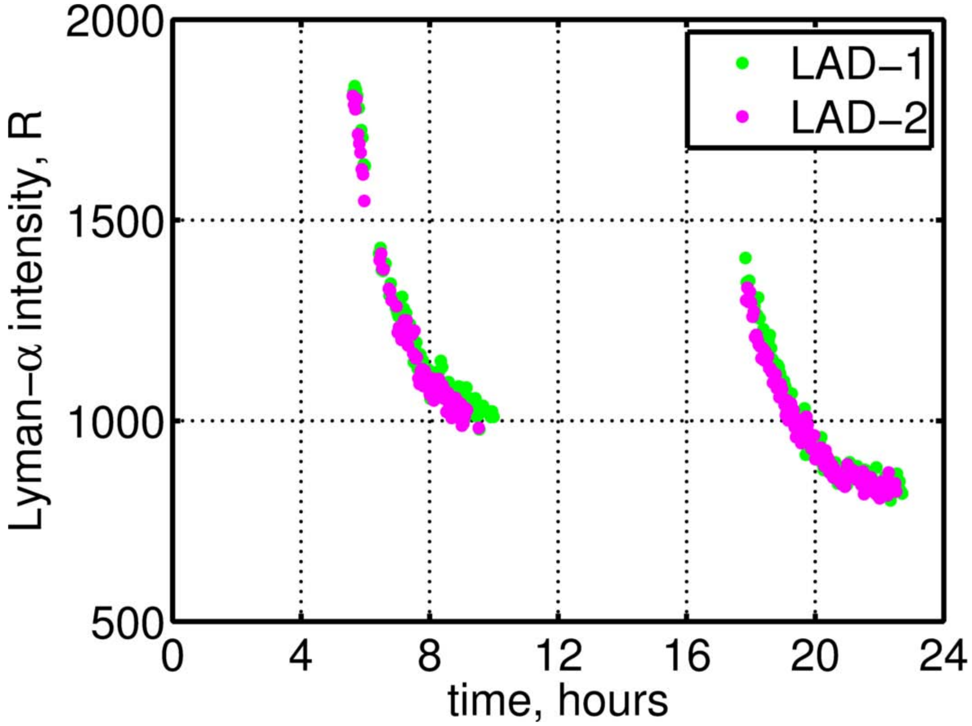

Figure 45. LAD-1 (green dots) and LAD-2 (pink dots) measured Lyman-α intensities at ω = -90°and ω = 90°, respectively, for both TWINS-1 orbits on 6 August 2011; the LAD-1 measurements have been increased by a factor of 1 / 0.80 = 1.25.

Applying the cross calibration ratio to all LAD-1 measurements on 6 August 2011 appears to correct a possible offset in all measurements, as shown in Figure 46.

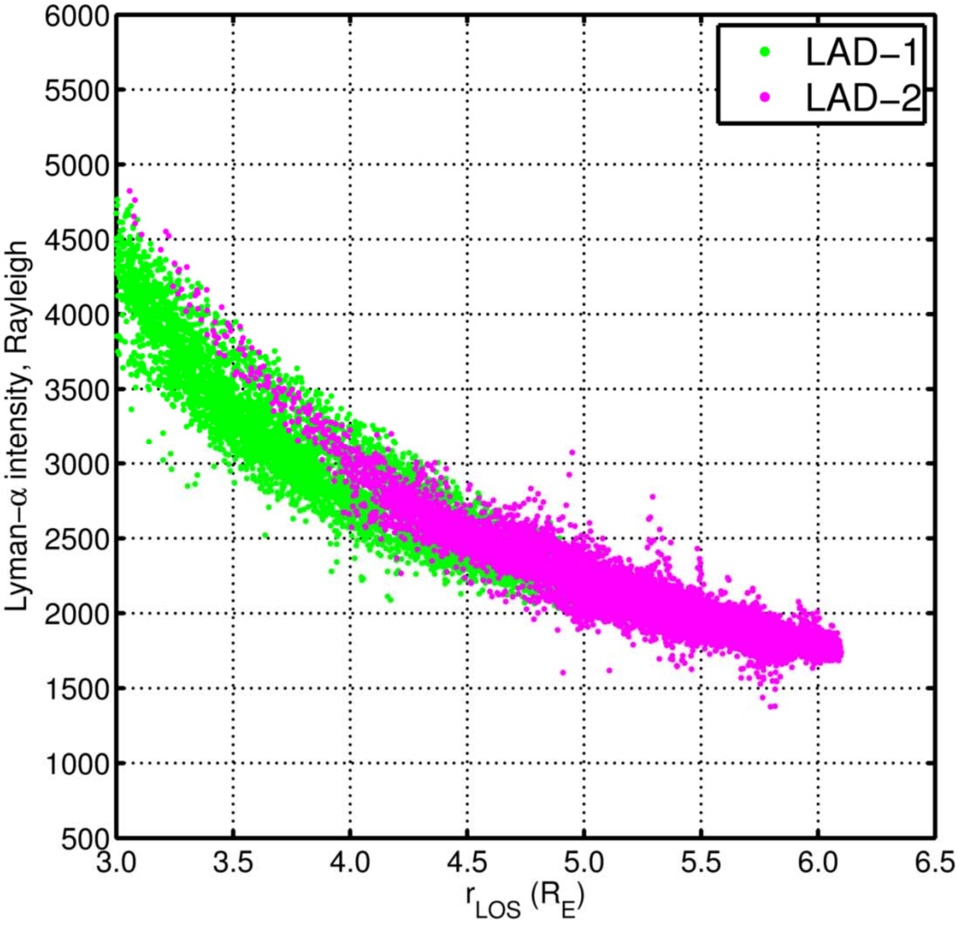

Figure 46. The Lyman-α intensity observed by both LAD-1 (green dots) and LAD-2 (pink dots) on TWINS-1 for 6 August 2011 versus the geocentric distance of each line-of-sight closest approach to the Earth, r_{LOS}; the LAD-1 measurements have been increased by a factor of 1 / 0.80 = 1.25.

The cross calibration ratio between LAD-1 and LAD-2 for all orbits from the start of TWINS-1 (Figure 47) and TWINS-2 (Figure 48) operations in 2008 through 2011 was calculated. The ratio is only near unity in the summer months of 2008 for TWINS-1 and in September and October of 2008 for TWINS-2. The obtained times series is always applied when reconstructing exospheric H density distributions.

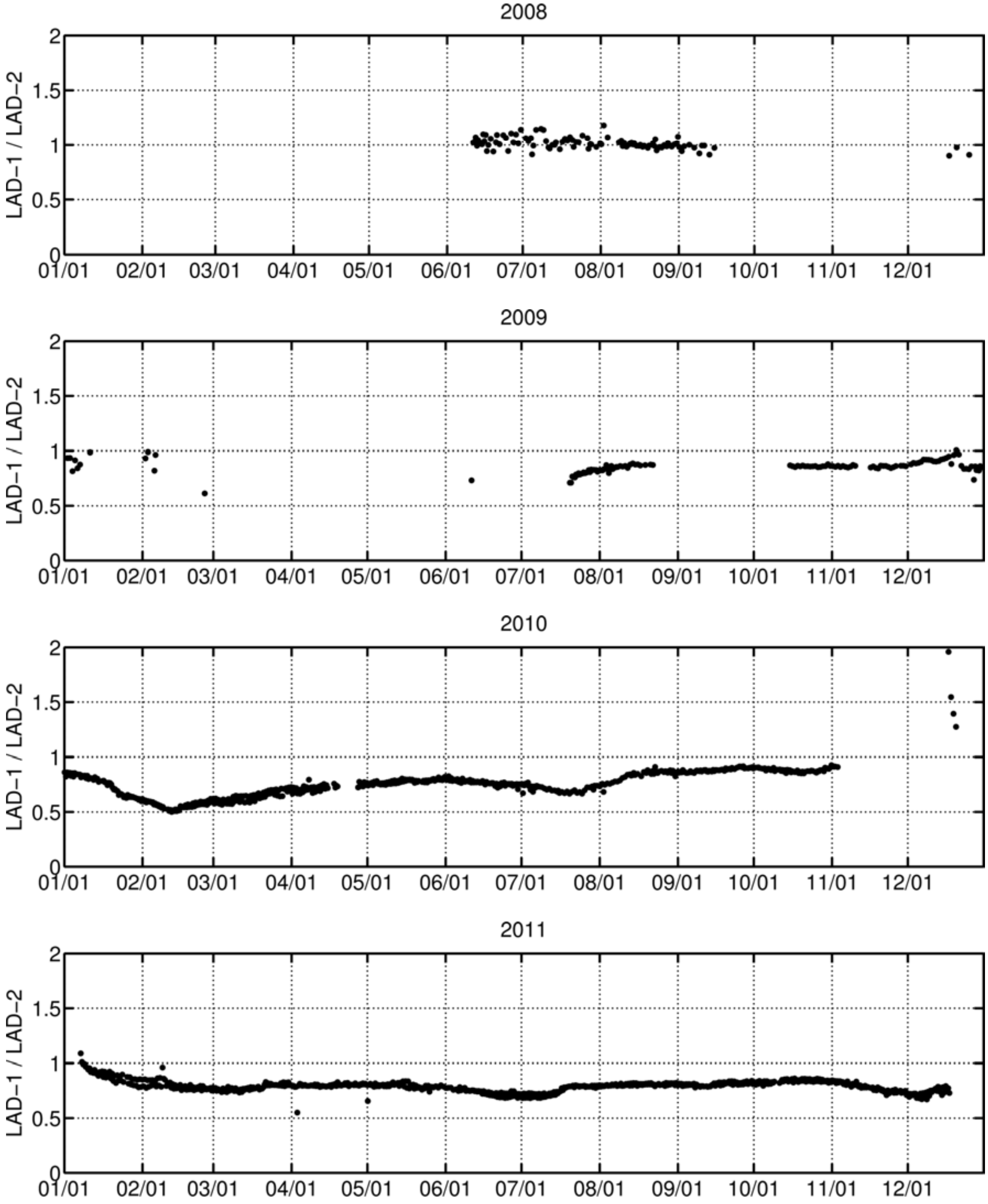

Figure 47. The ratio of cross calibration, LAD-1 / LAD-2, for TWINS-1 from 2008 (top) through 2011 (bottom).

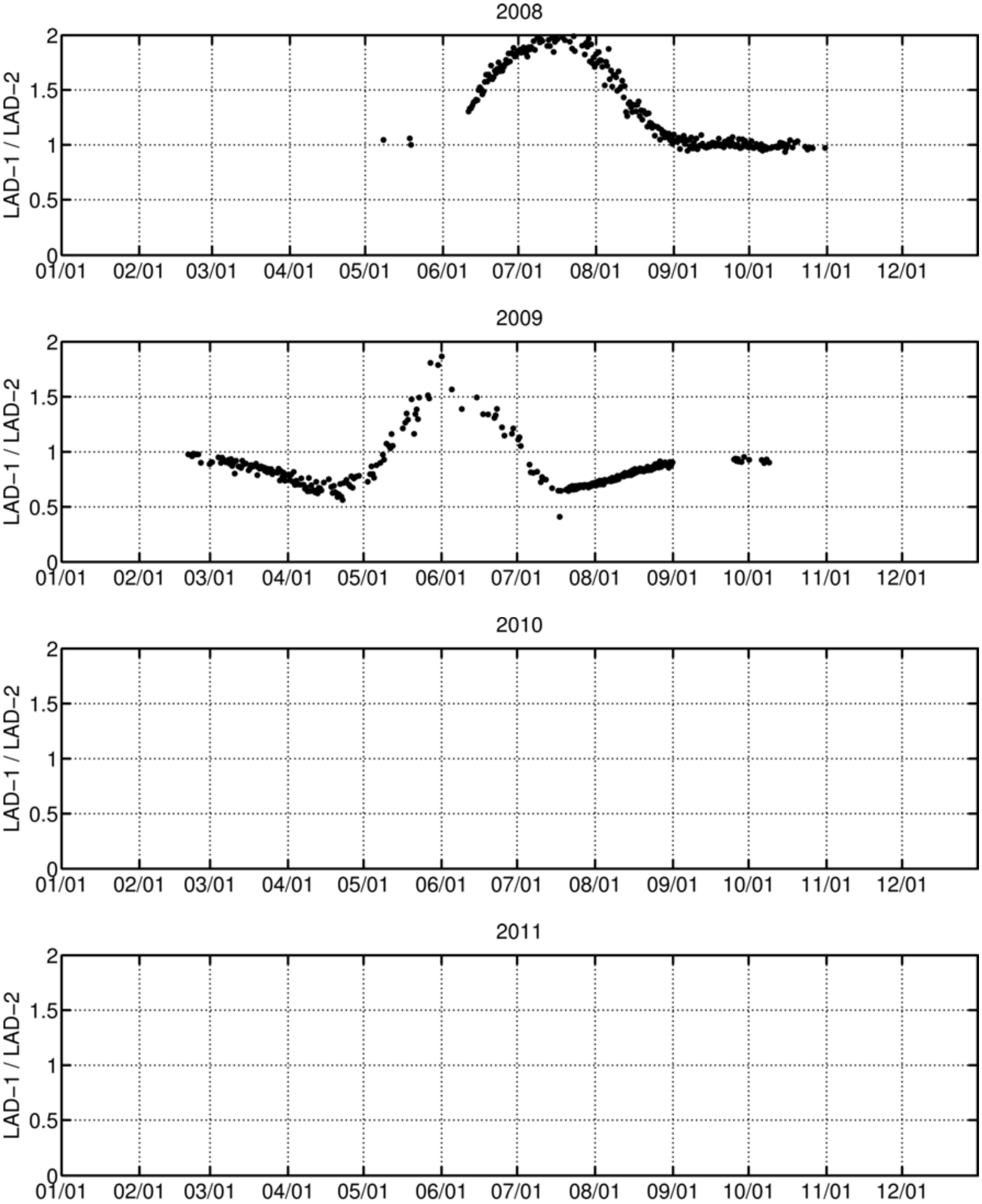
2008

2009

2010

2011

Figure 48. The ratio of cross calibration, LAD-1 / LAD-2, for TWINS-2 from 2008 (top) through 2011 (bottom).

6.7 Example Day, 11 June 2008

Using LAD data from TWINS-1 on 11 June 2008, a three-dimensional exospheric H number density distribution was obtained, as an example. The corresponding parameter values in Equations 53 – 55 are listed in Table 3, where n_H is in cm^{-3} and r is in R$_E$.

Table 3. Parameters of the exospheric H number density distribution (Equations 53 – 55) obtained using LAD data from TWINS-1 on 11 June 2008 in Geocentric Equatorial Noon (GEN) coordinates; n_H is in cm^{-3} and r is in R$_E$.

Radial and Angular Parameters	June to September 2008
p	8.5886×10^{3}
k	-2.5446
a_{10}	-4.8992×10^{-2}
b_{10}	-1.1927×10^{-2}
a_{11}	-3.8248×10^{-1}
b_{11}	5.7744×10^{-2}
c_{11}	-4.8547×10^{-2}
d_{11}	-1.3753×10^{-2}
a_{20}	1.5739×10^{-1}
b_{20}	-3.9474×10^{-2}
a_{21}	-6.9198×10^{-2}
b_{21}	2.8973×10^{-2}
c_{21}	2.1922×10^{-1}
d_{21}	-4.5158×10^{-2}
a_{22}	-1.0148×10^{-1}
b_{22}	9.4756×10^{-3}
c_{22}	-8.8242×10^{-2}
d_{22}	2.7003×10^{-2}

Figure 49 shows cross sections of the obtained 11 June 2008 distribution. The left panel shows a contour plot in the equatorial plane; day-night and dawn-dusk asymmetries are clearly visible. The right panel shows a contour plot in the meridional Earth-Sun plane, where one can see day-night and north-south asymmetries. For larger geocentric distances, the inferring of density values becomes more challenging as the geocentric distance of an LAD line-of-sight closest approach to the Earth, r_{LOS}, where densities are highest, never exceeds 6.5 R_E.

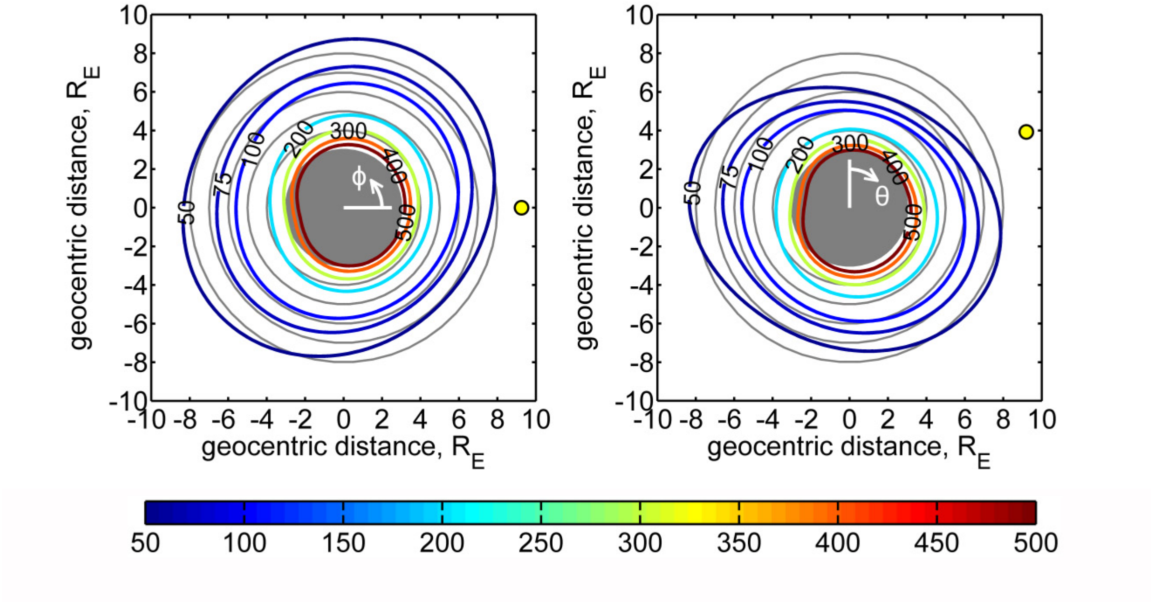

Figure 49. Contour plots of the exospheric H number density distribution on 11 June 2008: (left) an equatorial (*XY* plane) cross section and (right) a meridional (*XZ* plane) cross section. Also shown are the definitions of the angles ϕ and θ. Contours are lines of constant neutral hydrogen number density (cm^{-3}); the color bar is for the contour lines; the yellow dot is the projection of the direction to the Sun (left) and the direction to the Sun (right); the filled shaded circle represents the region with radius 3 R_E; and the grid of shaded concentric circles for $r > 3$ R_E, with a 1 R_E step, highlights the asymmetry of the distribution.

The global distribution exhibits asymmetry in the day-night, dawn-dusk, and north-south directions. Figure 50 presents the angular variation of the distribution at geocentric distances 3 R_E, 6 R_E, and 8 R_E. Similar to Figure 49, the left plots show number densities in the equatorial plane and the right plots in the meridional Earth-Sun plane.

For lower geocentric distances, the dayside has noticeably higher densities than the nightside. This dayside maximum can be seen at 3 R_E (Figure 50, top) with $\phi \approx 60°$ and $\theta \approx 155°$. A nightside enhancement appears at 6 R_E (Figure 50, middle) with $\phi \approx 235°$ and $\theta \approx 280°$. At 8 R_E (Figure 50, bottom), this nightside enhancement becomes almost as pronounced as the dayside maximum. As the geocentric distance increases beyond 8 R_E, the nightside densities become increasingly more pronounced than the dayside densities, consistent with the location of a geotail.

The duskside has noticeably higher densities than the dawnside. This asymmetry can be seen in the left plots of Figure 49 as, compared to the dawnside with ϕ between 180° and 360°, generally higher densities exist on the duskside with ϕ between 0° and 180°.

The right plots of Figure 49 clearly show that the Southern Hemisphere has noticeably higher densities than the Northern Hemisphere. This observed asymmetry is consistent with the *Hodges* [1994] solstice distributions.

The coverage of the exosphere by LAD observations is incomplete, as determined by the mission geometry. The obtained asymmetry of the H distribution should be more sensitive to the incomplete coverage than the averaged radial density profile $N(r)$.

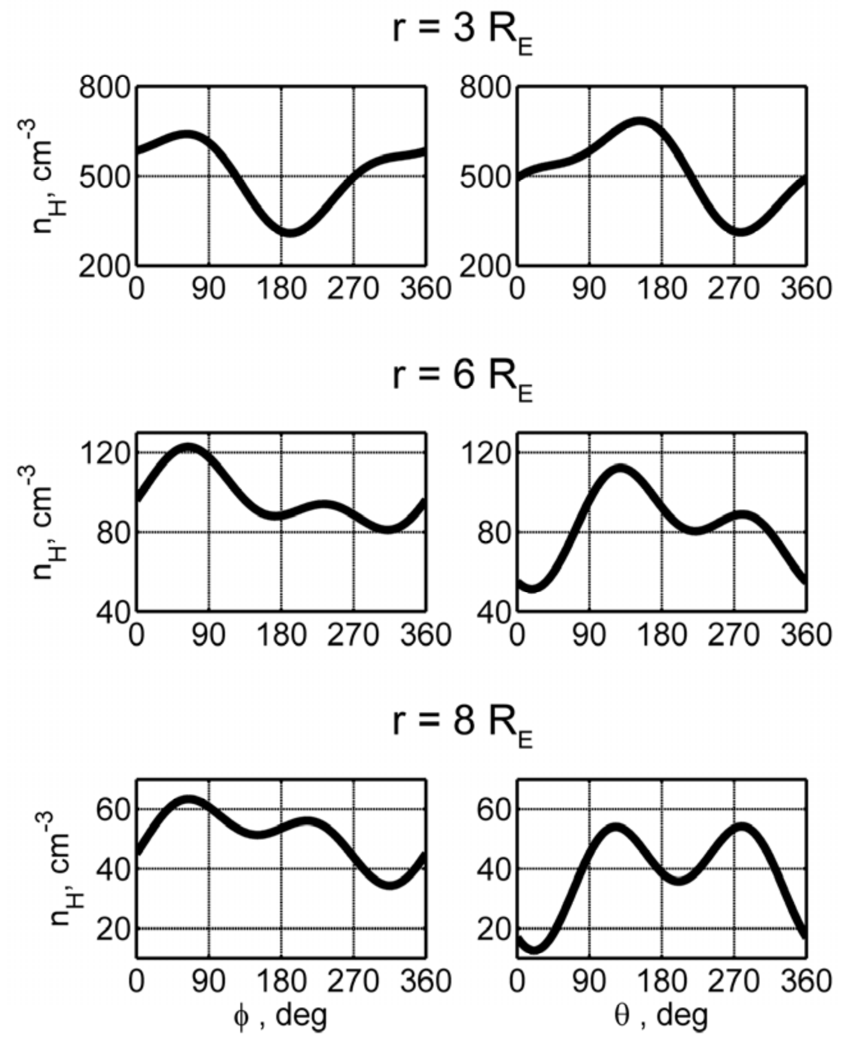

Figure 50. Exospheric H number density in the obtained 11 June 2008 distribution as a function of angles ϕ and θ for geocentric distances 3 R_E (top), 6 R_E (middle), and 8 R_E (bottom). In the left plots (θ = 90°), the angle ϕ = 0° is equatorial noon and the angle ϕ = 90° is dusk. In the right plots (ϕ = 0°), the angle θ = 0° is north and the angle θ = 90° is equatorial noon.

A visualization technique was developed to further investigate the three-dimensional asymmetry in the obtained exospheric H number density distribution on 11 June 2008. Figure 51 shows spherical H density contour plots at 6 different geocentric distances from 3 R_E to 8 R_E; the gray lines point toward equatorial noon, the black lines are the celestial pole, and the yellow lines are the direction to the Sun.

A consistent feature at all geocentric distances is that the Southern Hemisphere has noticeably higher densities than the Northern Hemisphere. The dayside has higher densities than the nightside for lower geocentric distances, but the nightside becomes increasingly more pronounced with increasing geocentric distance up to 8 R_E

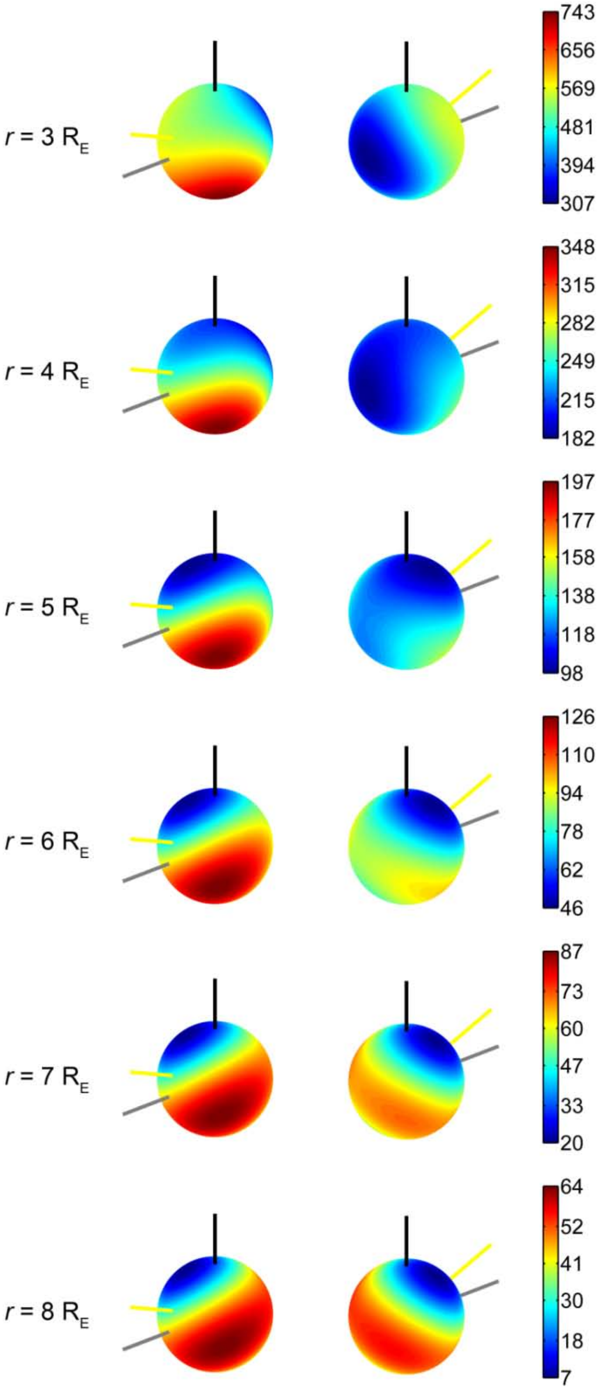

Figure 51. Three-dimensional contour plots of the exospheric H number density distribution on 11 June 2008 for spherical shells at 6 different geocentric distances from 3 R_E to 8 R_E; the gray lines point toward equatorial noon, the black lines are the celestial pole, the yellow lines are the direction to the Sun, and the color bars are in cm^{-3}.

6.7.1 H Density Radial Profile

Figure 52 compares the spherically symmetric radial component, $N(r)$, of the 11 June 2008 distribution to prior models. The density profile is remarkably close to those obtained by *Rairden et al.* [1986], *Hodges* [1994], and *Østgaard et al.* [2003], with differences less than 50% between 3 to 8 R_E.

The conditions of the observation on 11 June 2008 correspond to solar minimum. The DE 1 measurements used by *Rairden et al.* [1986] were obtained over a different phase of the solar cycle, during the solar activity increase from 1981 to 1985. *Østgaard et al.* [2003] also reported on a different phase of the solar cycle as they used GEO/IMAGE measurements near solar maximum from June 2000 to June 2001. In addition to being solar minimum with an F10.7 value of 66, the observation on 11 June 2008 was seasonally close to summer solstice. Thus, the Hodges [1994] solstice distribution with an F10.7 value of 80 represents the most similar conditions.

For geocentric distances $r > 4.5$ R_E, the *Zoennchen et al.* [2010] density profile shows somewhat higher densities than those by *Rairden et al.* [1986], *Hodges* [1994], and *Østgaard et al.* [2003], as well as in the 11 June 2008 distribution. The higher densities obtained by the Bonn group were due to much lower approximations for the interplanetary glow that have since been revised to be consistent with *Pryor et al.* [2012].

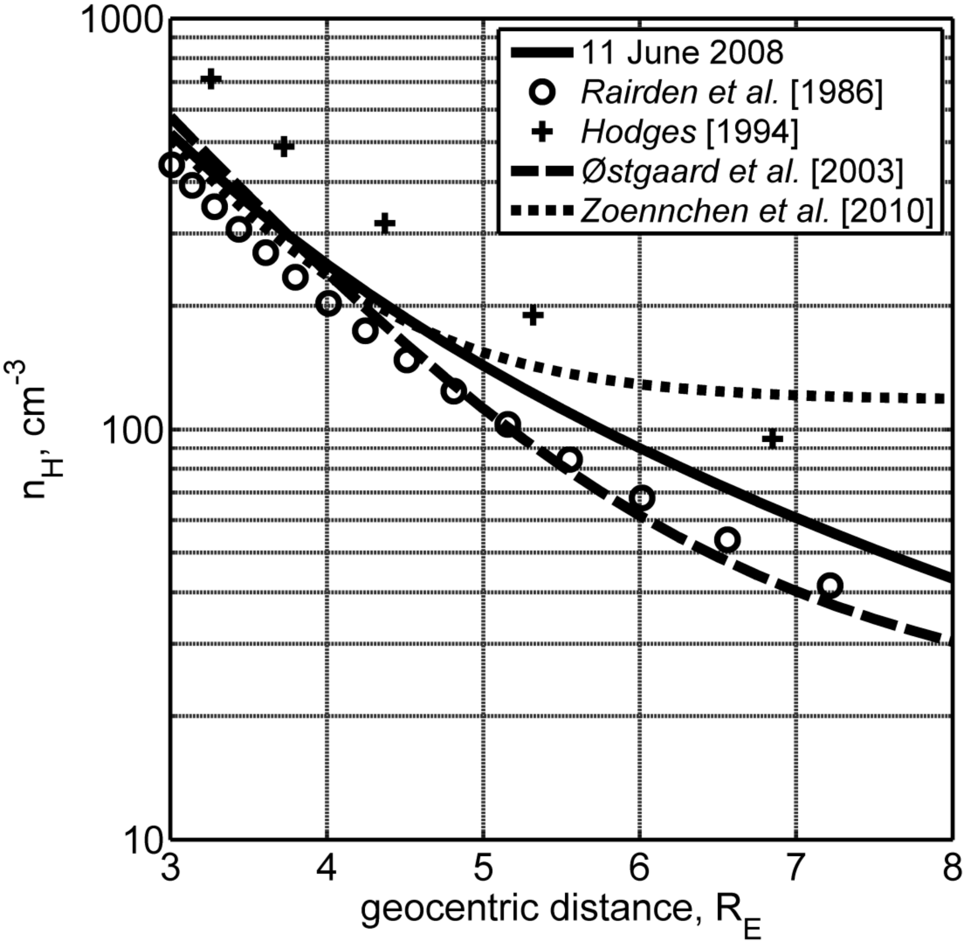

Figure 52. Comparison of different H number density profiles on 11 June 2008 from this work (solid line), *Rairden et al.* [1986] (circles), *Hodges* [1994] at solstice for F10.7 = 80 (crosses), *Østgaard et al.* [2003] for solar zenith angle 90° (long dashed line), and *Zoennchen et al.* [2010] on 11 June 2008 (short dashed line).

6.7.2 H Distribution Asymmetry

The 11 June 2008 distribution shares similar three-dimensional features to those obtained by *Hodges* [1994] in that they both exhibit an enhancement in the antisolar direction (geotail) and an enhancement in the solar direction. Figure 53 shows the density distribution along four radial directions: north, south, equatorial noon, and equatorial midnight, from 3 to 8 R_E. While the model used describes number densities at larger geocentric distances, validating the values beyond 8 R_E becomes increasingly difficult. However, it is noted that the densities are consistent with the H densities inferred from measurements by the Interstellar Boundary Explorer (IBEX) mission [*Fuselier et al.*, 2010], which carries sensitive ENA detectors. *Fuselier et al.* [2010] recently reported an H number density range of 4 – 11 cm^{-3} at the subsolar magnetopause (~ 10 R_E geocentric distance along the Earth-Sun line).

For geocentric distances $r < 6$ R_E, the density profile for equatorial noon is higher than for equatorial midnight. As the geocentric distance increases, the density profile for equatorial midnight decreases less rapidly than for equatorial noon until the former becomes dominant, similar to the asymmetry observed by *Østgaard et al.* [2003]. This asymmetry is less pronounced than that of *Zoennchen et al.* [2010].

A north-south asymmetry also exists, such that the H densities are depleted at higher geocentric distances in the Northern Hemisphere. At 4 R_E, the southern polar region has 40% higher densities than in the northern polar region; increasing to 70% at 6 R_E and 125% at 8 R_E. This asymmetry is likely caused by the Sun's position near summer solstice at this time. The *Hodges* [1994] solstice distributions exhibit similar asymmetry. While his solstice distribution for F10.7 = 80 is nearly symmetric at lower geocentric distances, beyond 4 R_E densities in the Northern Hemisphere decrease more rapidly than in the Southern Hemisphere.

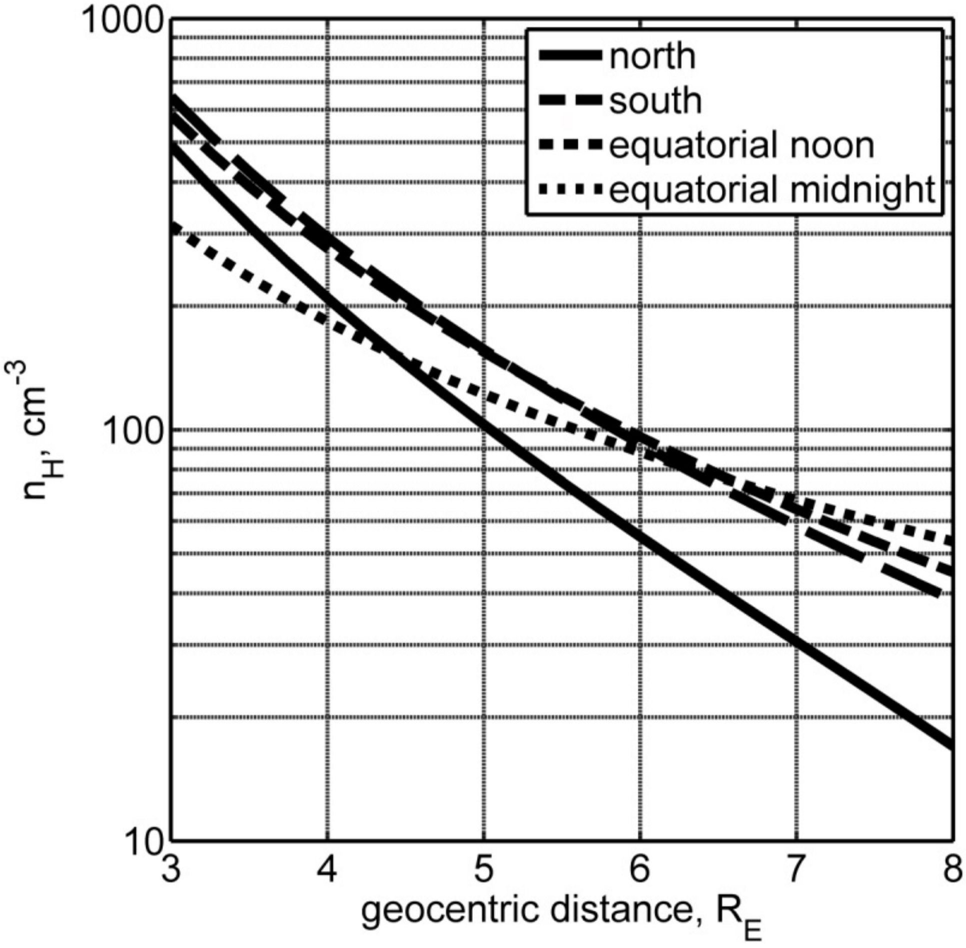

Figure 53. Exospheric H number density radial dependencies of the 11 June 2008 distribution toward north (solid line), south (long dashed line), equatorial noon (short dashed line), and equatorial midnight (dotted line).

6.8 Error Analysis

The least squares curve fit minimizes the standard deviation,

$$\sigma^2 = \frac{1}{n-m}\sum_i \left(C_a - C_f\right)^2 , \tag{63}$$

between the observed intensities C_a and the fitted intensities C_f provided by the model, where n is the number of observations and m is the number of fitting parameters ($n - m$ is the degrees of freedom). A rigorous derivation of the uncertainty in the retrieved H densities is needed to demonstrate the validity of the fitting procedure. An error analysis adapted from *Bevington and Robinson* [2003] was performed in two steps. First, the standard deviation for each model parameter, σ_z, was obtained using the relationship

$$\sigma_z^2 = \sum_i \left[{\sigma_f}^2 \left(\frac{\partial z}{\partial C_f} \right)^2 \right], \tag{64}$$

where σ_f is the standard deviation of each observation and $\partial z/\partial C_f$ is the partial derivative of the z$^{\text{th}}$ parameter $(p, k, a_{lm}, b_{lm}, c_{lm}, d_{lm})$ of each observation. This operation is performed such that the covariance matrix, $\boldsymbol{C}$, is determined,

$$\boldsymbol{C} = \boldsymbol{\sigma}^2 \boldsymbol{J}\boldsymbol{J}^{-1} , \tag{65}$$

where $\boldsymbol{J}$ is the Jacobian matrix (all 1st order partial derivatives). Second, with the propagated standard deviation of each fitted parameter, the total can be calculated using the propagation of errors,

$$\sigma^2 = \sigma_p^2 \left(\frac{\partial C_f}{\partial p}\right)^2 + \sigma_k^2 \left(\frac{\partial C_f}{\partial k}\right)^2 + \ldots + 2\sigma_{pk}^2 \left(\frac{\partial C_f}{\partial p}\right)\left(\frac{\partial C_f}{\partial k}\right) + \ldots . \tag{66}$$

A successful fit predicts the measured intensities to within a standard deviation of around 125 R, which would be, for example, less than 5% and 10% of typical intensities at distances < 4 R_E and < 6 R_E, respectively. The random Poissonian error for the range of measured detector counts does not exceed 2%. The estimated uncertainty in the obtained 11 June 2008 distribution (Figure 54) slowly increases from 7% to 9% from 3 R_E to 6 R_E and then rapidly increases up to 25% at 8 R_E.

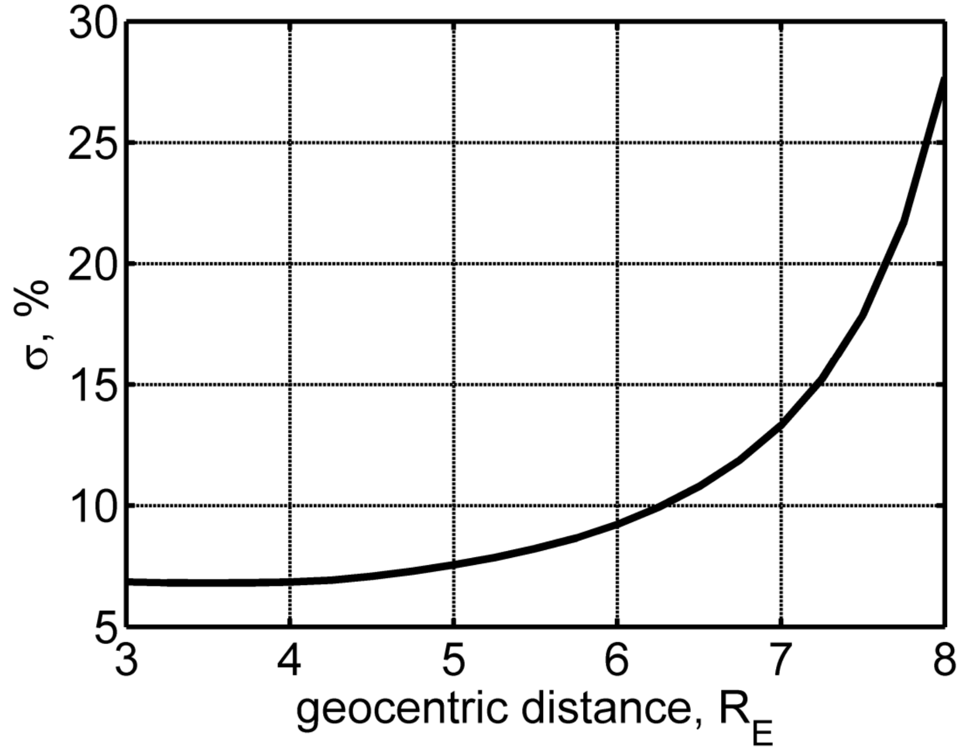

Figure 54. The estimated uncertainty in the obtained 11 June 2008 distribution. The distribution should be restricted to $r < 8\ R_E$, or used with appropriate caution for higher geocentric distances.

Figure 55 shows the spherically symmetric radial component, $N(r)$, of the 11 June 2008 distribution with error bars plotted at regular intervals along the density profile.

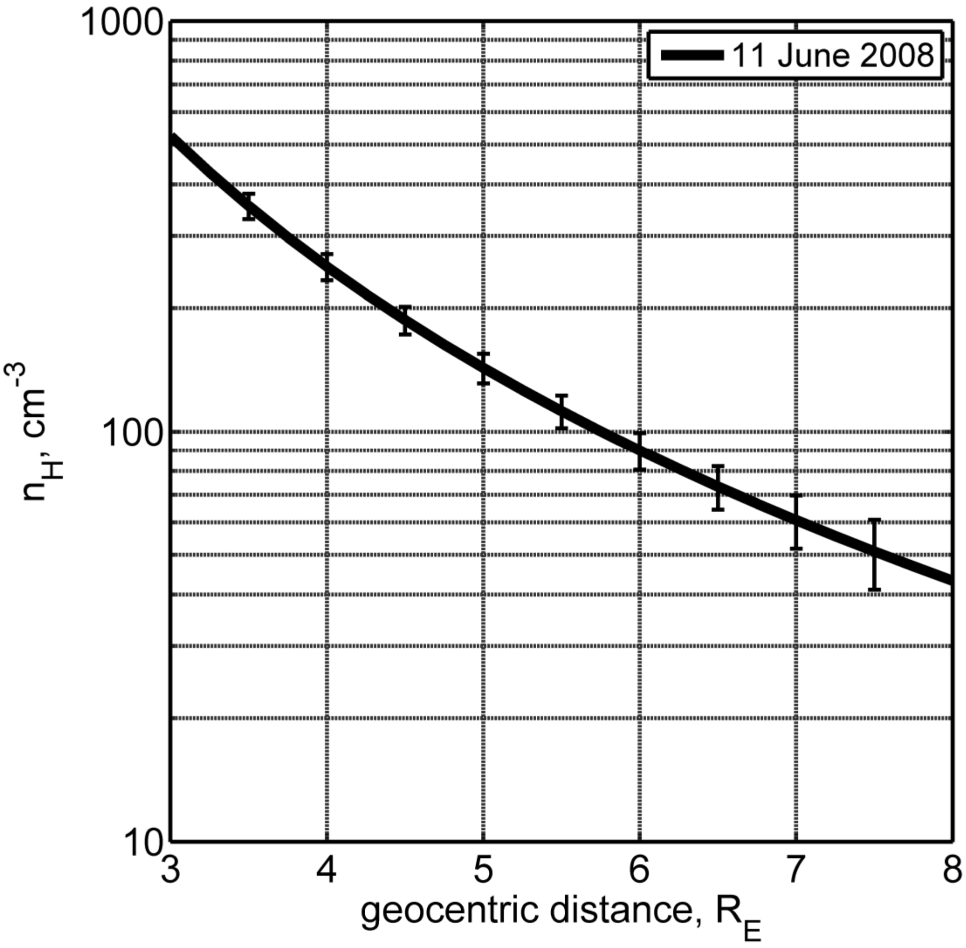

Figure 55. The H number density profile for the obtained 11 June 2008 distribution with error bars to represent the fitting uncertainty.

Chapter 7: Spatial and Temporal Response of the Exosphere

The TWINS mission provides unprecedented observational coverage of the geocorona such that global distributions with three-dimensional asymmetries can be obtained without having to average over extended periods of time. However, detector lines-of-sight on the dayside are often pointed at < 90° from the solar direction, due to the satellite orbit orientation with respect to the seasonal position of the Sun, and must therefore be excluded to mitigate possible solar contamination – resulting in only partial coverage around the Earth. Consequently, only selected TWINS-1 observations in the summer months of 2008 are used for obtaining global distributions.

A sequence of distributions was obtained to study the dynamic exosphere responding to seasonal variation from a summer solstice to autumnal equinox (Section 7.1). Additionally, since the averaged radial density profile, $N(r)$, should be less sensitive to the incomplete coverage than asymmetry in the three-dimensional distributions, a sequence of density profiles for a time period that includes four magnetic storms has been obtained to investigate the effect of geomagnetic variation (Section 7.2).

7.1 Seasonal Variation

Heating of the upper atmosphere on the dayside, by solar X-ray and EUV radiation, causes asymmetry of the exosphere. For example, a seasonal north-south asymmetry occurs as solar illumination differs between the summer and winter polar regions. A very low solar cycle minimum with minimal 27-day variation (< 5%)

persisted, and additionally the geomagnetic conditions were quiet, through the summer months of 2008. Consequently, three time periods (18-22 June, 18-22 July, and 18-22 August) were chosen to investigate seasonal variation from the summer solstice to autumnal equinox in 2008. The TWINS-1 observational coverage for 18-22 June 2008 and 18-22 July 2008 was excellent, but for 18-22 August 2008 the dayside is excluded to mitigate possible solar contamination because lines-of-sight are pointed at < 90° from the direction to the Sun. The parameter values in Equations 53 – 55 for the 18-22 June 2008 distribution are listed in Table 4, where n_H is in cm^{-3} and r is in R$_E$.

Table 4. Parameters of the exospheric H number density distribution (Equations 53 – 55) obtained using LAD data from TWINS-1 on 18-22 June 2008 in Geocentric Equatorial Noon (GEN) coordinates; n_H is in cm^{-3} and r is in R$_E$.

Radial and Angular Parameters	18-22 June 2008
p	1.0505×10^{4}
k	-2.7418
a_{10}	1.5782×10^{-2}
b_{10}	-1.0551×10^{-3}
a_{11}	-4.2828×10^{-1}
b_{11}	5.1883×10^{-2}
c_{11}	-2.7034×10^{-2}
d_{11}	-5.4775×10^{-3}
a_{20}	2.3120×10^{-1}
b_{20}	-5.3657×10^{-2}
a_{21}	1.2715×10^{-1}
b_{21}	-3.9517×10^{-2}
c_{21}	5.0743×10^{-2}
d_{21}	-8.0776×10^{-3}
a_{22}	-1.9040×10^{-1}
b_{22}	4.2901×10^{-2}
c_{22}	1.0511×10^{-1}
d_{22}	-1.4176×10^{-2}

Figure 56 shows cross sections of the obtained 18-22 June 2008 distribution. The left panel shows a contour plot in the equatorial plane and the right panel shows a contour plot in the meridional Earth-Sun plane. The solar-antisolar asymmetry is remarkably similar to the *Hodges* [1994] solstice distributions and *Carruthers et al.* [1976] images.

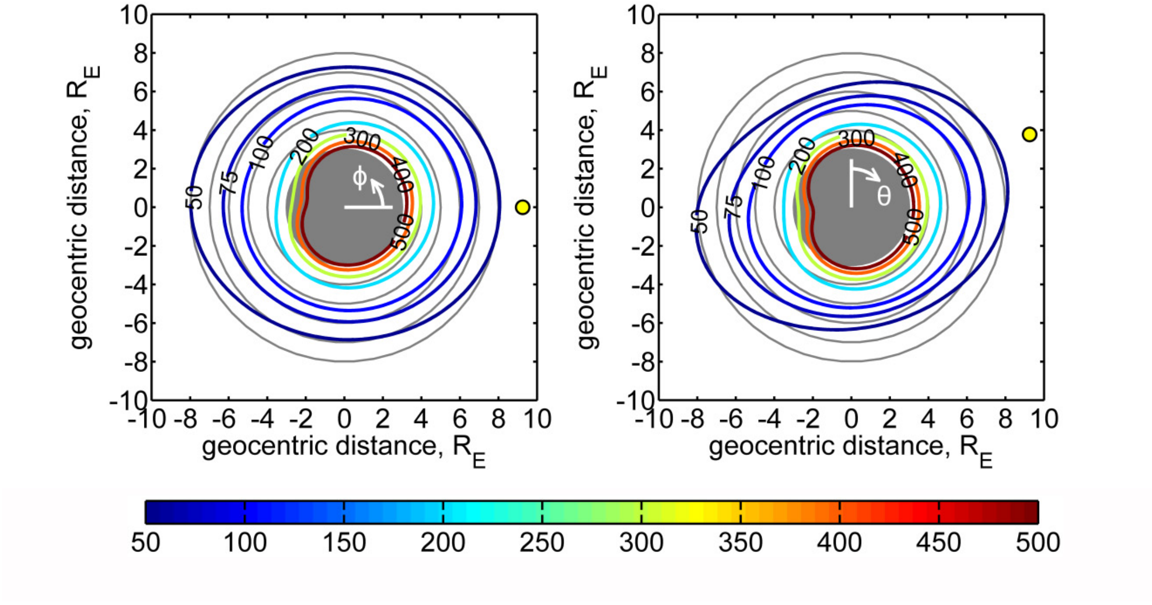

Figure 56. Contour plots of the exospheric H number density distribution on 18-22 June 2008: (left) an equatorial (*XY* plane) cross section and (right) a meridional (*XZ* plane) cross section. Also shown are the definitions of the angles ϕ and θ. Contours are lines of constant neutral hydrogen number density (cm^{-3}); the color bar is for the contour lines; the yellow dot is the projection of the direction to the Sun (left) and the direction to the Sun (right); the filled shaded circle represents the region with radius 3 R_E; and the grid of shaded concentric circles for $r > 3$ R_E, with a 1 R_E step, highlights the asymmetry of the distribution.

The global distribution exhibits three-dimensional asymmetries. Figure 57 presents the angular variation of the distribution at geocentric distances 3 R_E, 6 R_E, and 8 R_E. Similar to Figure 56, the left plots show number densities in the equatorial plane and the right plots in the meridional Earth-Sun plane.

For lower geocentric distances, the dayside has noticeably higher densities than the nightside. This dayside maximum can be seen at 3 R_E (Figure 57, top) with $\phi \approx 45°$ and θ between 0° and 155°. A nightside enhancement appears at 6 R_E (Figure 57, middle) with $\phi \approx 180°$ and $\theta \approx 250°$. At 8 R_E (Figure 57, bottom), the nightside enhancement becomes almost as pronounced as the dayside maximum. As the geocentric distance increases beyond 8 R_E, the nightside densities become increasingly more pronounced than the dayside densities, consistent with the location of a geotail.

The dawn-dusk asymmetry is minimal, visible in the left plots of Figure 57 as, compared to the dawnside with ϕ between 180° and 360°, the same general densities exist on the duskside with ϕ between 0° and 180°.

The right plots of Figure 57 show that the northern and Southern Hemispheres have similar densities, but at 6 R_E and 8 R_E enhancements in the solar ($\theta \approx 75°$) and antisolar ($\theta \approx 255°$) direction are clearly visible. This observed asymmetry is remarkably consistent with the *Hodges* [1994] solstice distributions.

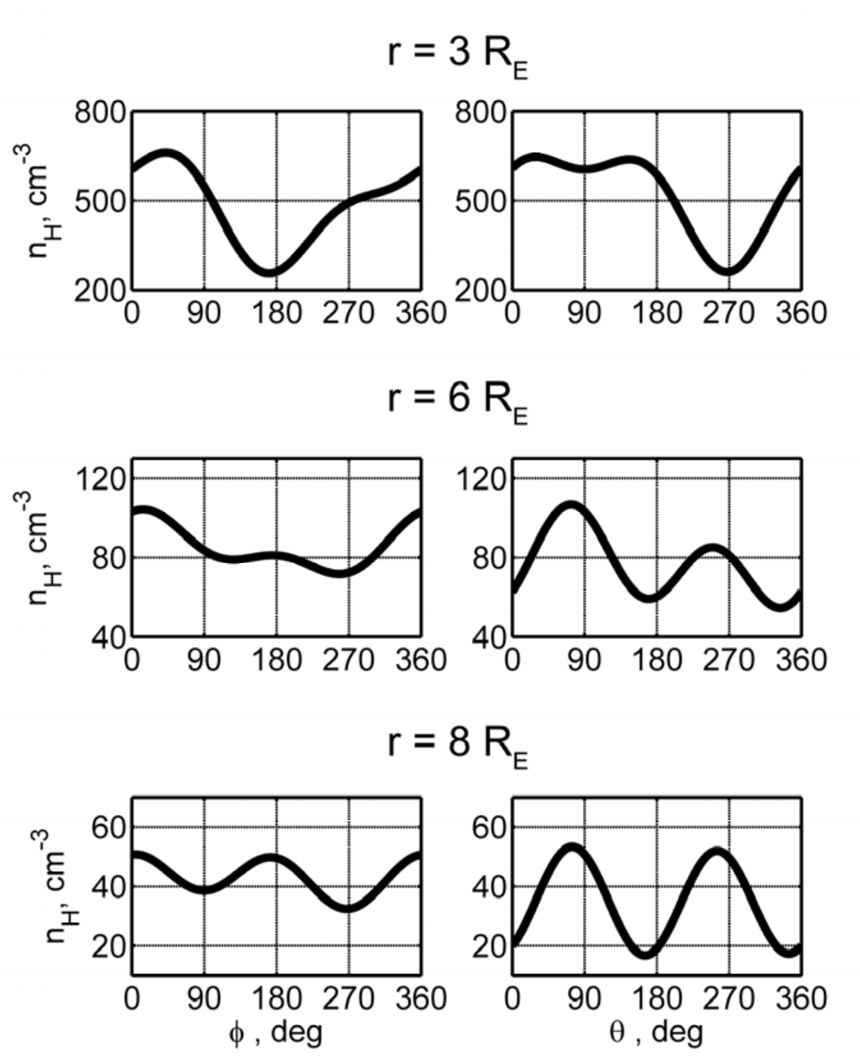

Figure 57. Exospheric H number density in the obtained 18-22 June 2008 distribution as a function of angles ϕ and θ for geocentric distances 3 R_E (top), 6 R_E (middle), and 8 R_E (bottom). In the left plots ($\theta = 90°$), the angle $\phi = 0°$ is equatorial noon and the angle $\phi = 90°$ is dusk. In the right plots ($\phi = 0°$), the angle $\theta = 0°$ is north and the angle $\theta = 90°$ is equatorial noon.

Asymmetry in the day-night direction is the dominant feature visible in all the spherical contour plots shown in Figure 58. As the geocentric distance increases, asymmetry along the solar-antisolar direction emerges and additionally the pole-equator asymmetry becomes more pronounced. The dawn-dusk asymmetry is minimal.

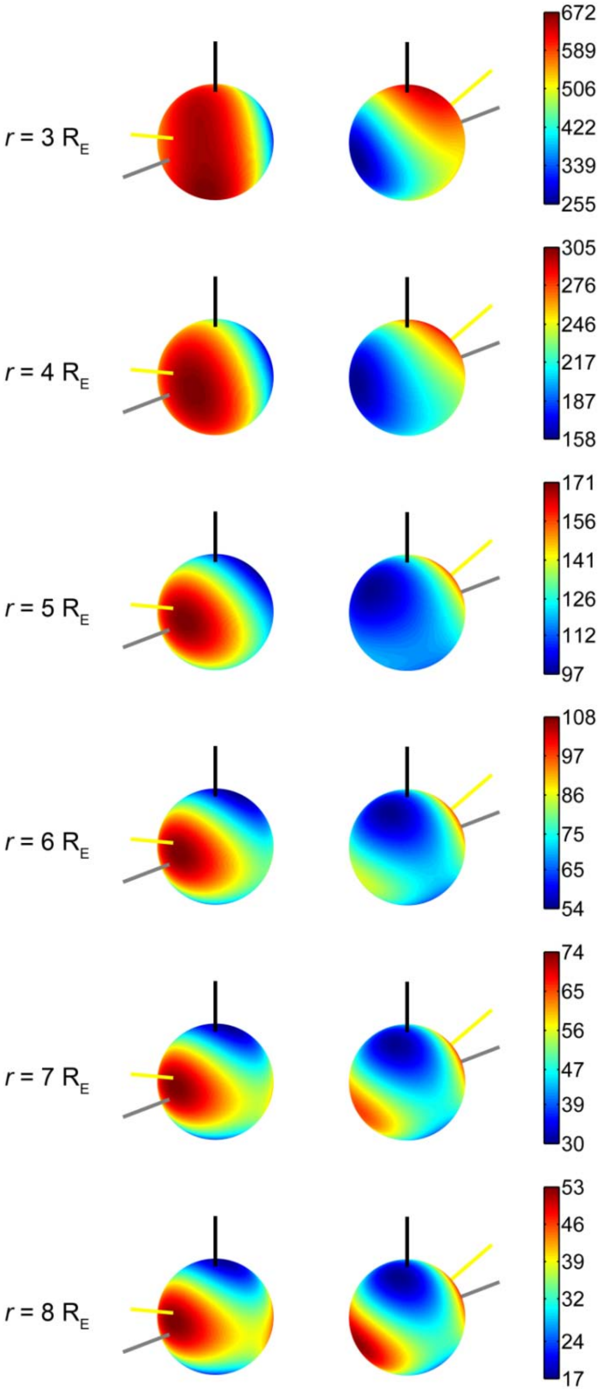

Figure 58. Three-dimensional contour plots of the exospheric H number density distribution on 18-22 June 2008 for spherical shells at 6 different geocentric distances from 3 R_E to 8 R_E; the gray lines point toward equatorial noon, the black lines are the celestial pole, the yellow lines are the direction to the Sun, and the color bars are in cm^{-3}.

The 18-22 June 2008 distribution shares similar three-dimensional features to those obtained by *Hodges* [1994] in that they both exhibit pronounced enhancements in the antisolar direction (geotail) and in the solar direction. Figure 59 shows the density distribution along four radial directions, north, south, equatorial noon, and equatorial midnight, from 3 R_E to 8 R_E. For geocentric distances $r < 6$ R_E, the density profile for equatorial noon is higher than for equatorial midnight. As the geocentric distance increases, the density profile for equatorial midnight decreases less rapidly than for equatorial noon until the former becomes dominant, similar to the asymmetry observed by *Østgaard et al.* [2003]. At 8 R_E, the density profiles for equatorial noon and equatorial midnight are significantly higher for north and south.

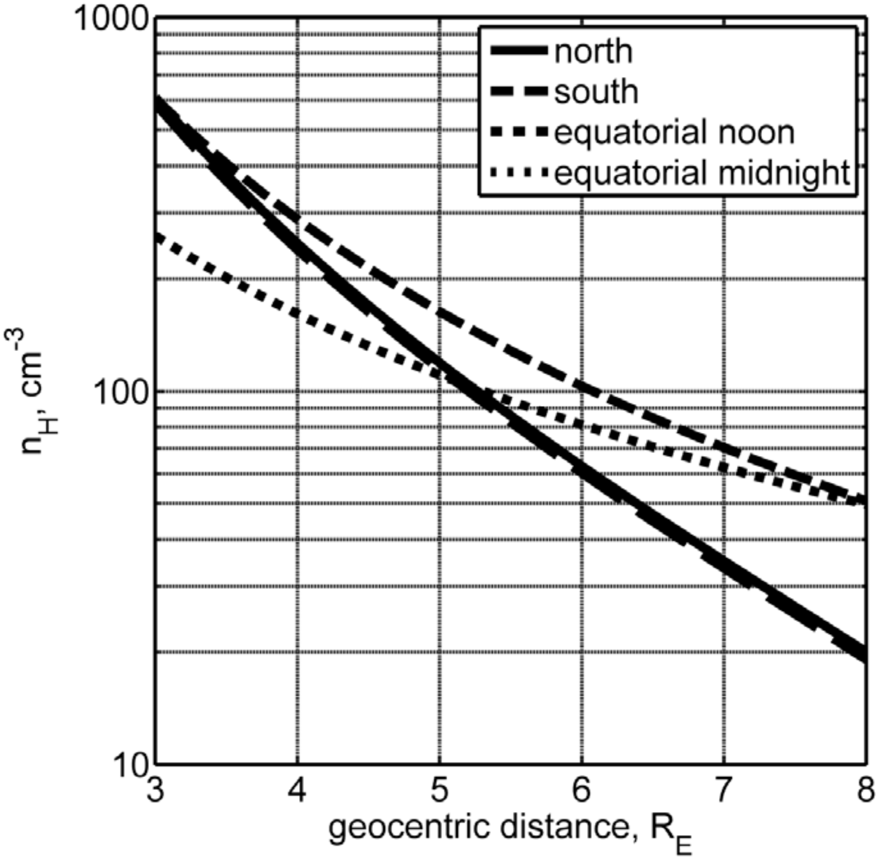

Figure 59. Exospheric H number density radial dependencies of the 18-22 June 2008 distribution toward north (solid line), south (long dashed line), equatorial noon (short dashed line), and equatorial midnight (dotted line).

The three-dimensional asymmetry on 18-22 June 2008 is compared to two other distributions obtained using TWINS-1 LAD data on 18-22 July 2008 and 18-22 August 2008 in Figure 60. All three distributions exhibit asymmetry that appears oriented with respect to the solar-antisolar direction such that there are enhancements on the dayside and nightside that is remarkably consistent with the spatial variation in the *Hodges* [1994] solstice distributions and *Carruthers et al.* [1976] images.

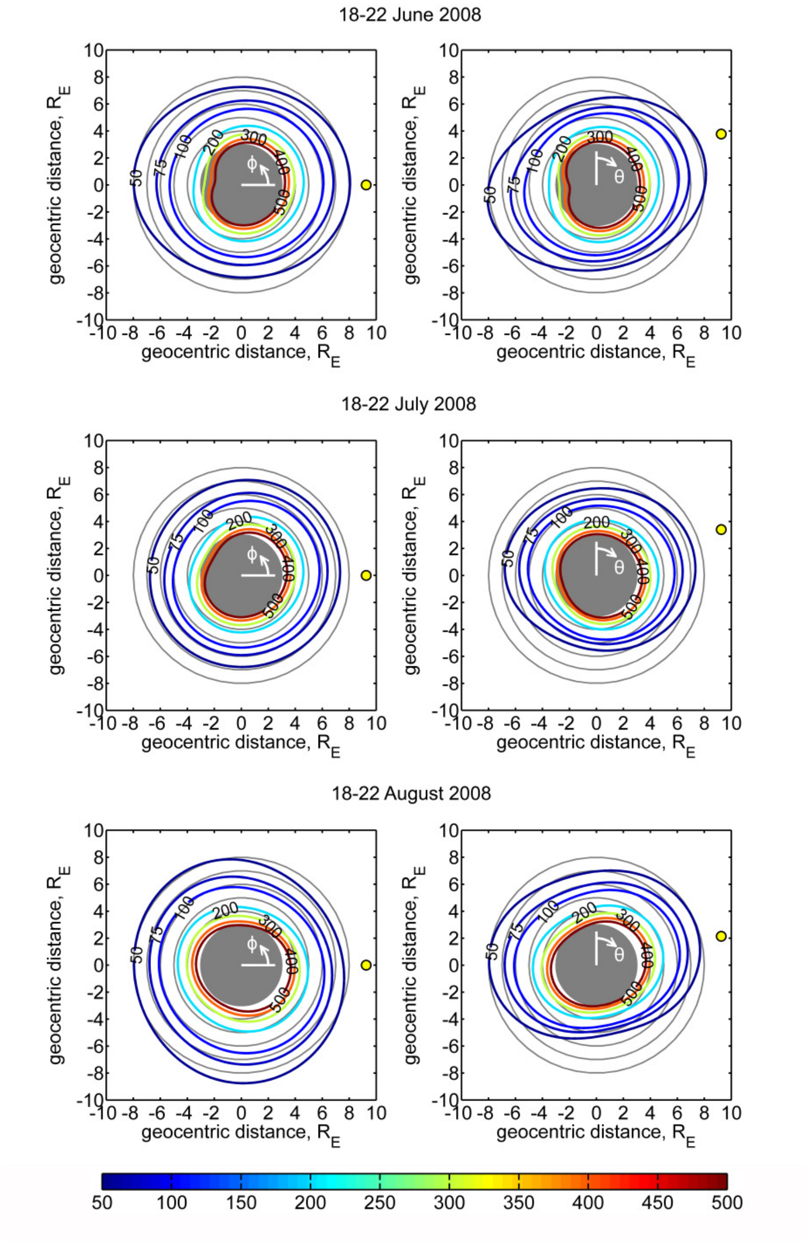

Figure 60. Contour plots of the exospheric H number density distribution on 18-22 June 2008 (top), 18-22 July 2008 (middle), and 18-22 August 2008 (bottom). The left plots are an equatorial (*XY* plane) cross section and the right plots are a meridional (*XZ* plane) cross section. Also shown are the definitions of the angles ϕ and θ. Contours are lines of constant neutral hydrogen number density (cm^{-3}); the color bar is for the contour lines; the yellow dot is the projection of the direction to the Sun (left) and the direction to the Sun (right); the filled shaded circle represents the region with radius 3 R_E; and the grid of shaded concentric circles for $r > 3$ R_E, with a 1 R_E step, highlights the asymmetry of the distribution.

7.2 Geomagnetic Variation

A coupling effect via charge exchange exists between the exosphere and plasmasphere, but the response of the exosphere to geomagnetic variation has yet to be quantitatively completely understood yet. The disturbance storm time, Dst, index is a global average of the horizontal component of Earth's magnetic field at the magnetic equator used to characterize geomagnetic activity. For a typical magnetic storm, the Dst briefly rises, corresponding to the initial phase known as the storm sudden commencement, and then decreases sharply as the ring current intensifies. Once the interplanetary magnetic field (IMF) turns northward again, the Dst slowly rises back to quiet time levels near zero as magnetospheric features such as the ring current recover. The plasmapause is systematically closer to Earth during times of high geomagnetic activity, recovering gradually, such that the outer plasmasphere is observed to refill over a period of several days [*Carpenter and Park*, 1973]. Figure 61 shows hourly Dst values from 2008 through 2011 (available at the World Data Center for Geomagnetism website, http://wdc.kugi.kyoto-u.ac.jp/, provided by Kyoto University).

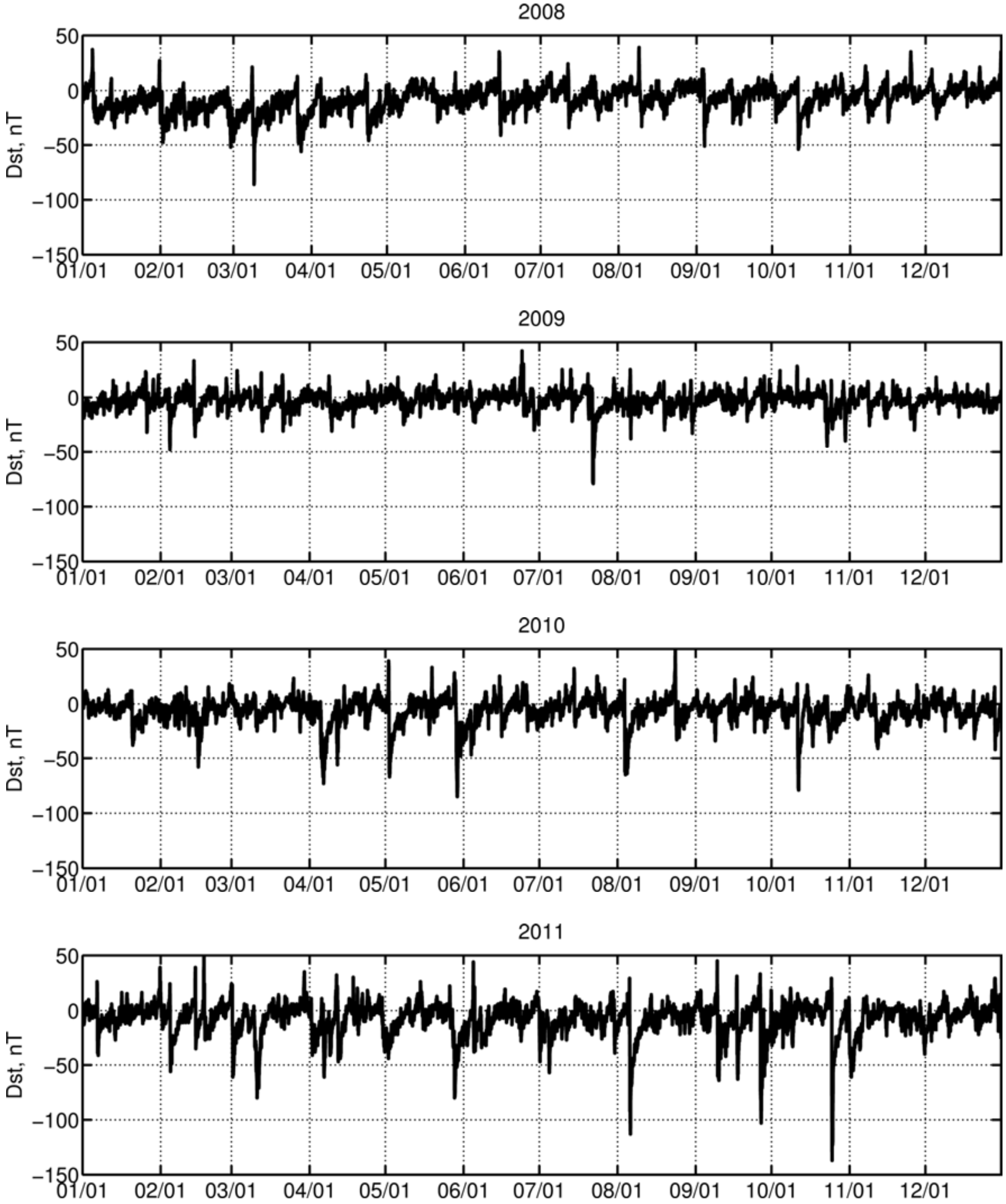

Figure 61. The disturbance storm time, Dst, index from 2008 (top) through 2011 (bottom), available at the World Data Center for Geomagnetism website, http://wdc.kugi.kyoto-u.ac.jp/, provided by Kyoto University.

The LADs on TWINS-1 only adequately covered the near-Earth region, such that global distributions with reliable three-dimensional asymmetries can be obtained, during the summer months of 2008 when no substantial geomagnetic activity occurred. Since the averaged radial density profile, $N(r)$, should be less sensitive to the incomplete coverage than asymmetry in the three-dimensional distributions, a sequence of 55 density profiles has been obtained using TWINS-1 LAD data from August and October in 2011 because four magnetic storms occurred during this time period (Figure 62, top). The number of H atoms, n_H, between a geocentric distance of 3 R_E to 8 R_E,

$$\begin{aligned} n_H &= \int_{3\,R_E}^{8\,R_E} N(r)\,4\pi r^2\,dr = \int_{3\,R_E}^{8\,R_E} p r^{-k}\,4\pi r^2\,dr \\ &= \frac{4\pi p}{3-k}\left[(8\,R_E)^{3-k} - (3\,R_E)^{3-k}\right], \end{aligned} \tag{67}$$

was calculated using the p and k values from each density profile, as a convenient way of characterizing the exosphere (Figure 62, bottom). Interestingly, single day increases in n_H from 5% to 15% are noticed at the times of the four magnetic storms on 6 August 2011, 10 September 2011, 18 September 2011, and 27 September 2011.

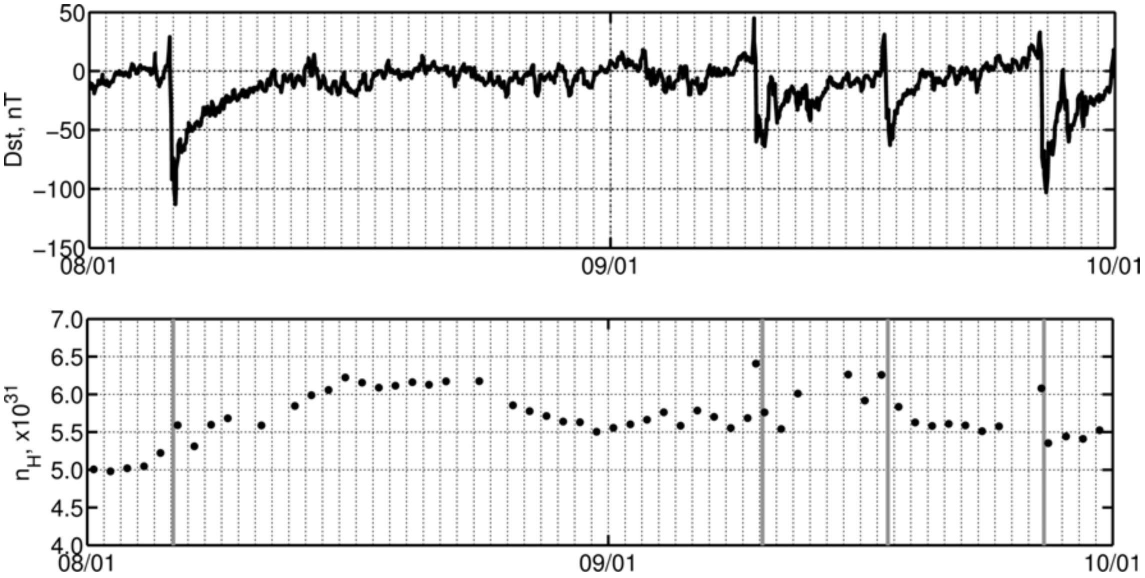

Figure 62. The Dst index (top) and number of H atoms between 3 R_E to 8 R_E calculated using the obtained density profiles (bottom) from 1 August 2011 to 1 October 2011. The four gray vertical lines in the bottom panel mark the hour of lowest Dst value for the corresponding magnetic storms.

It is not excluded that some apparent increase in the H atom population could be caused by increased detector noise due to an enhanced energetic particle environment during disturbed magnetospheric conditions. Plots of the LAD measurements on 10 September 2011 (Figure 63) and 27 September 2011 (Figure 64) versus each line-of-sight closest approach distance, r_{LOS}, have been color coded on an hourly basis to investigate the temporal response. It is anticipated that H densities, and in turn resonantly scattered Lyman-α intensities, would respond gradually to enhanced geomagnetic activity in contrast to the expectedly rapid change due to detector noise. One can see that in both Figure 63 and Figure 64 the observed intensities decrease slowly with time.

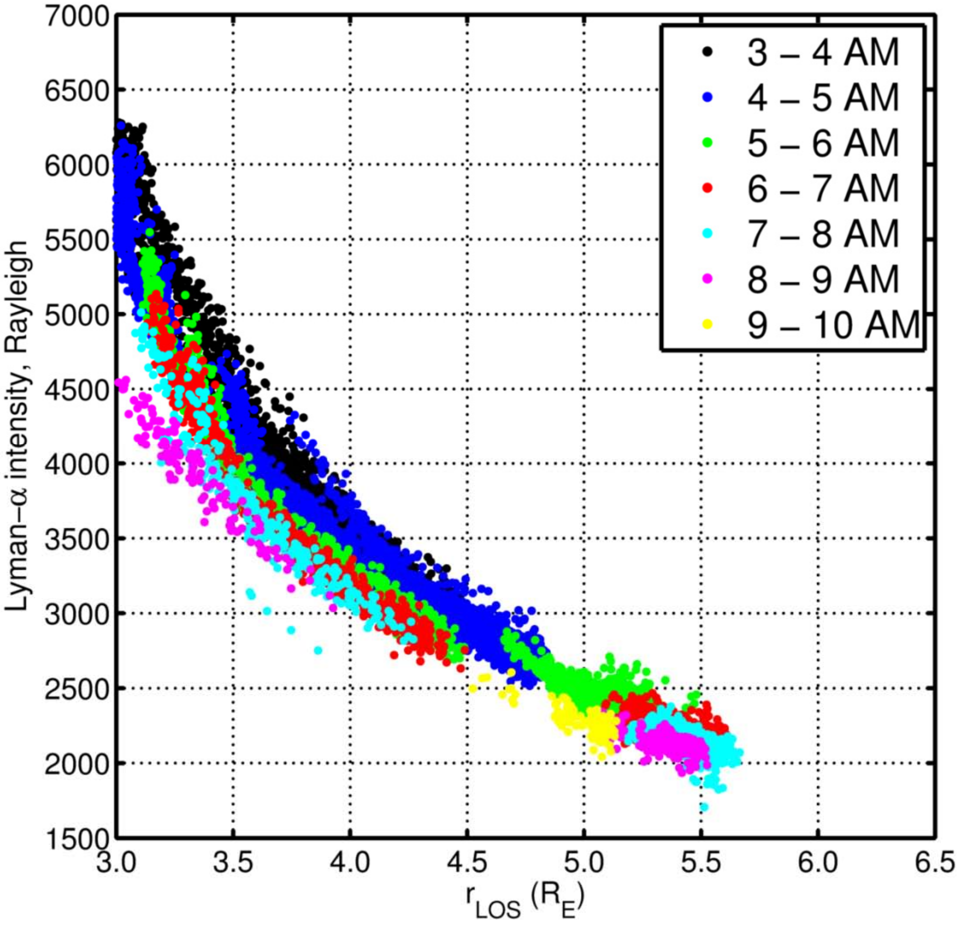

Figure 63. The Lyman-α intensity observed by both LADs on TWINS-1 for 10 September 2011 versus the geocentric distance of each line-of-sight closest approach to the Earth, r_{LOS}, color coded on an hourly basis. The storm sudden commencement occurred on 9 September 2011 at 10:00 PM. The Dst index began dropping on 10 September 2011 at 1:00 AM, reached -60 nT at 4:00 AM, and remained low before recovering from -64 nT at 4:00 PM.

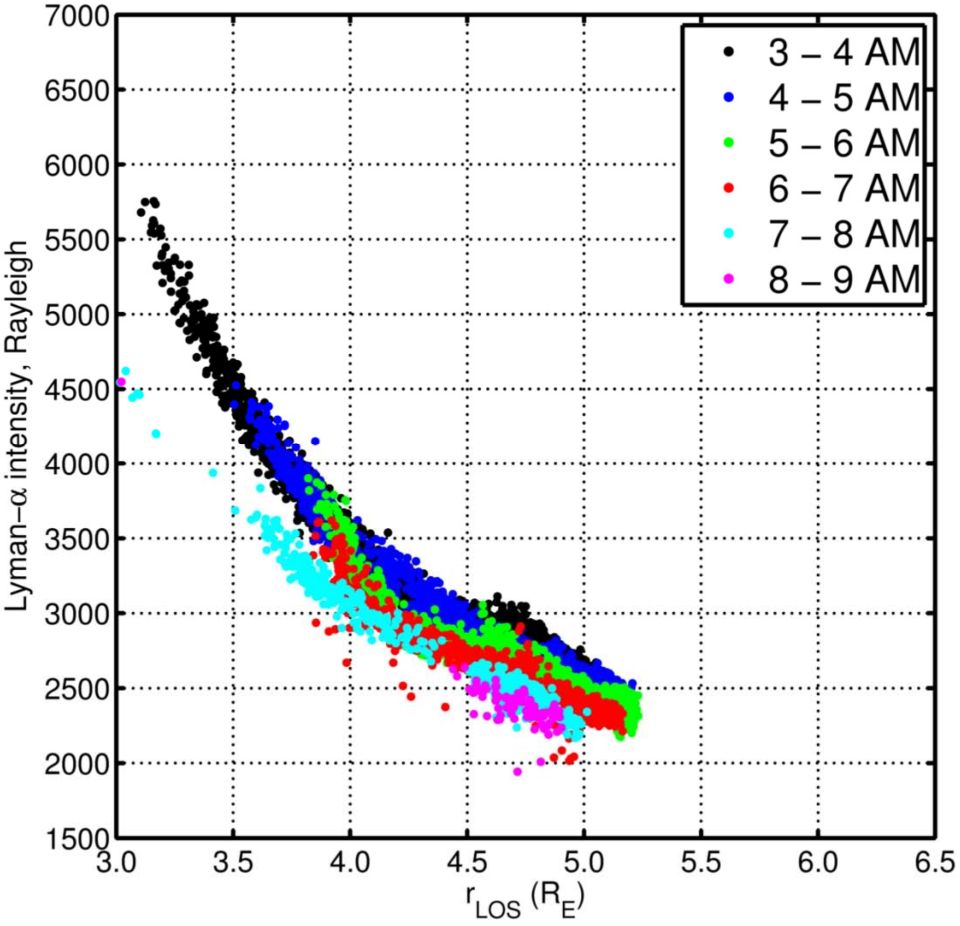

Figure 64. The Lyman-α intensity observed by both LADs on TWINS-1 for 27 September 2011 versus the geocentric distance of each line-of-sight closest approach to the Earth, r_{LOS}, color coded on an hourly basis. The storm sudden commencement occurred on 26 September 2011 at 10:00 PM. The Dst index began dropping on 27 September 2011 at 1:00 AM and reached -103 nT at 10:00 AM before recovering.

The electron and proton fluxes at geostationary orbit are measured by two of the Geostationary Operational Environmental Satellites, GOES-13 and -15, data available at the National Oceanic and Atmospheric Administration (NOAA) Space Weather Prediction Center (SWPC) website, http://www.swpc.noaa.gov/today.html. Figure 65 and Figure 66 show the electron fluxes from 9-12 September 2011 and 26-29 September 2011, respectively, since the obtained H density variation was most significant for the storms that occurred during these two time periods. The horizontal dashed line at 1000 electrons cm^{-2} s^{-1} sr^{-1} represents when deep dielectric discharging of > 2 MeV fluxes (blue and red curves) might potentially occur. The > 2 MeV fluxes only slightly exceeded the threshold value for brief periods on 9 September 2011 and 27 September 2011.

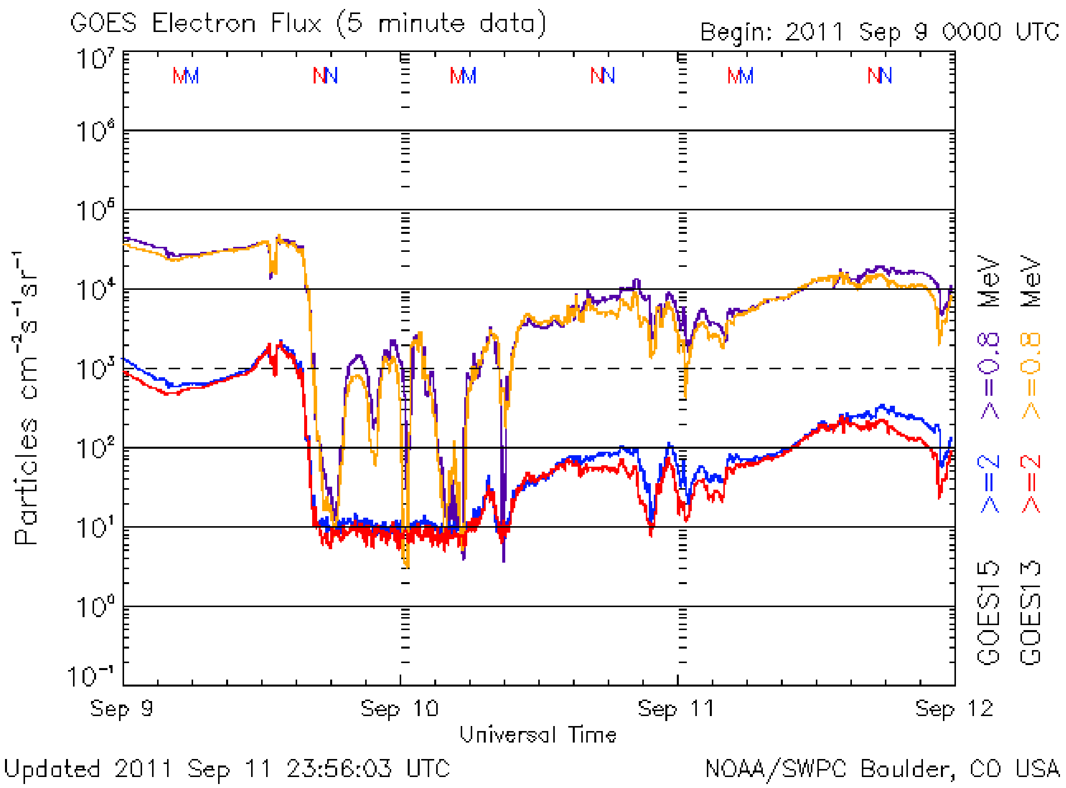

Figure 65. The intergral electron flux (electrons cm^{-2} s^{-1} sr^{-1}), averaged in 5 min intervals, with energies ≥ 0.8 MeV (purple and orange curves) and ≥ 2 MeV (blue and red curves) from 9 September 2011 to 12 September 2011, data available at the National Oceanic and Atmospheric Administration (NOAA) Space Weather Prediction Center (SWPC) website, http://www.swpc.noaa.gov/today.html.

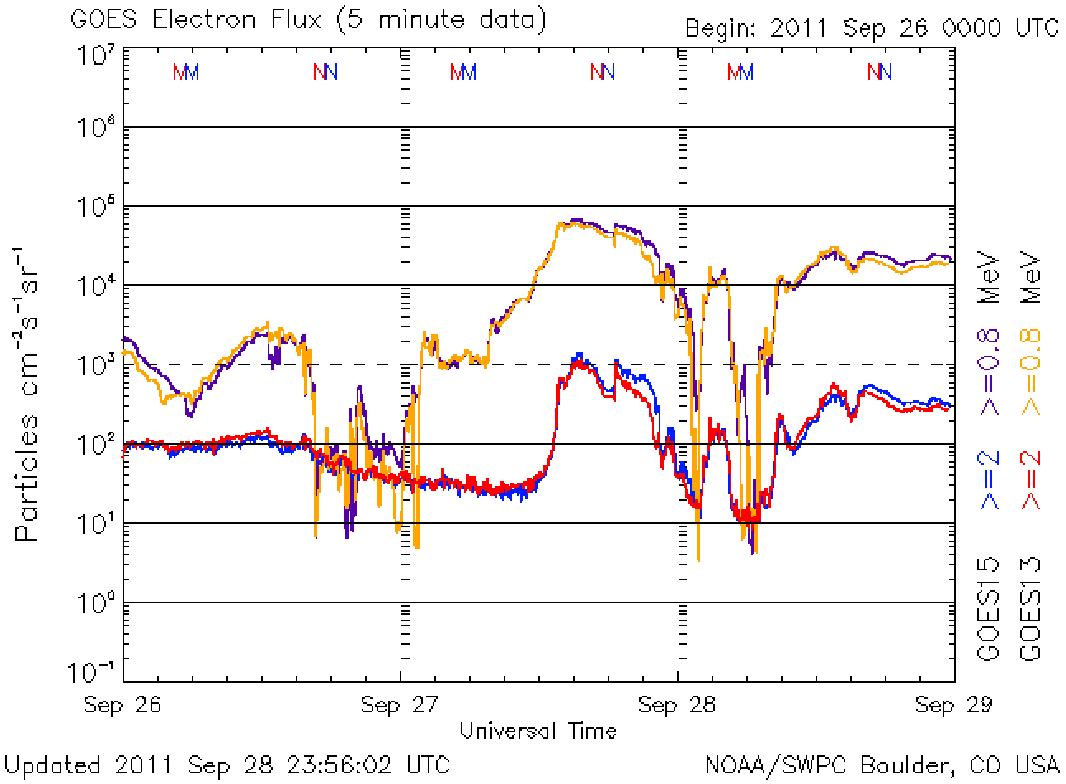

Figure 66. The intergral electron flux (electrons cm^{-2} s^{-1} sr^{-1}), averaged in 5 min intervals, with energies ≥ 0.8 MeV (purple and orange curves) and ≥ 2 MeV (blue and red curves) from 26 September 2011 to 29 September 2011, data available at the NOAA SWPC website, http://www.swpc.noaa.gov/today.html.

The proton fluxes from GOES-13 are shown for 9-12 September 2011 (Figure 67) and 26-29 September 2011 (Figure 68). The proton event threshold, represented by a horizontal dashed line at 10 protons cm^{-2} s^{-1} sr^{-1} at ≥ 10 MeV, was only slightly exceeded on 26 September 2006.

The relatively low levels of charged particle fluxes at geostationary orbit would likely be similar with respect to the TWINS-1 orbit location. However, a more accurate assessment should be performed using the environmental sensors on TWINS-1.

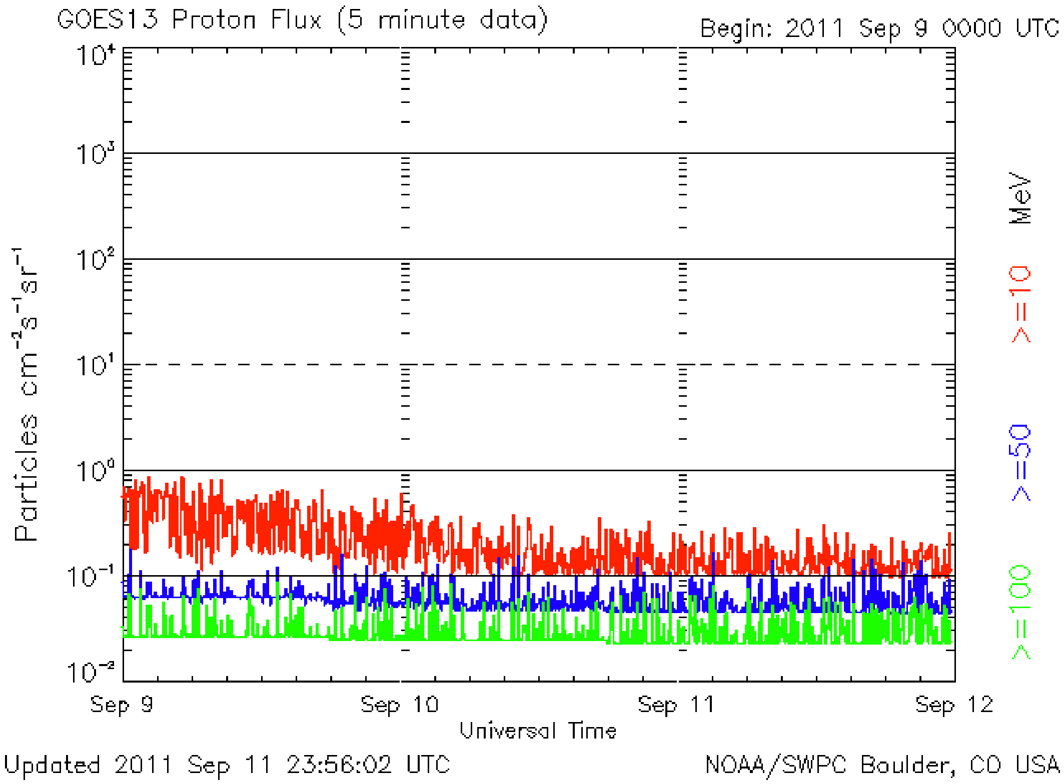

Figure 67. The integral proton flux (protons cm^{-2} s^{-1} sr^{-1}), averaged in 5 minute intervals, for energy thresholds of ≥ 10 MeV (red curves), ≥ 50 MeV (blue curves), and ≥ 100 MeV (green curves) from 9 September 2011 to 12 September 2011, data available at the NOAA SWPC website, http://www.swpc.noaa.gov/today.html.

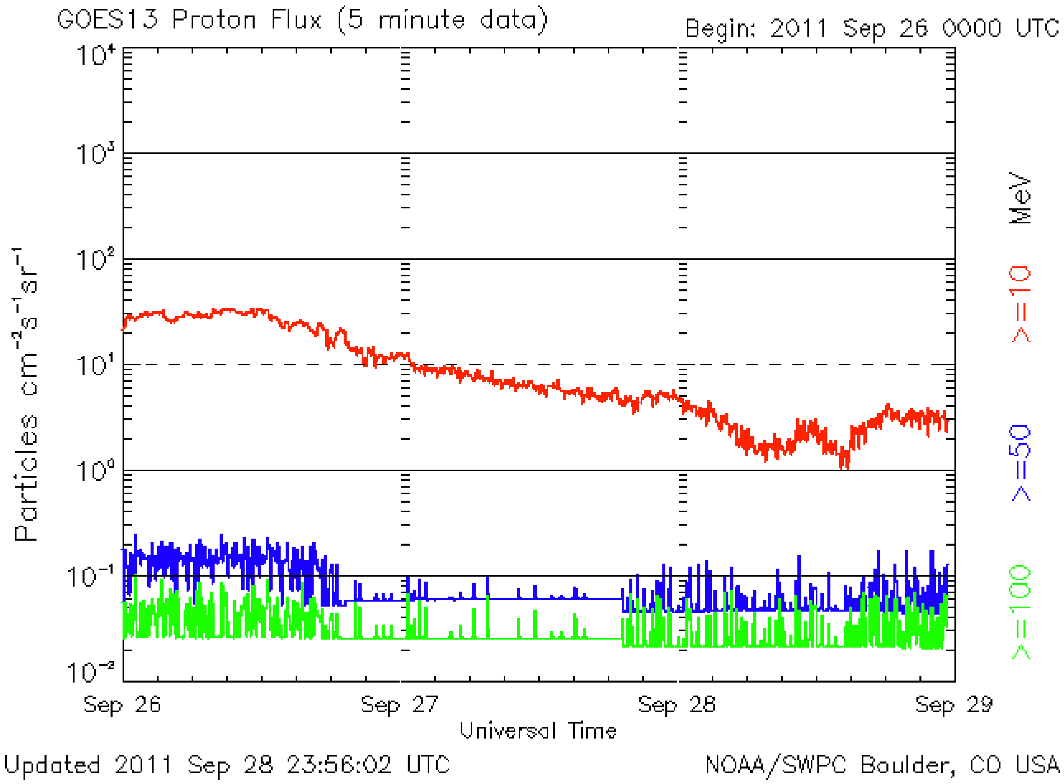

Figure 68. The integral proton flux (protons cm^{-2} s^{-1} sr^{-1}), averaged in 5 minute intervals, for energy thresholds of ≥ 10 MeV (red curves), ≥ 50 MeV (blue curves), and ≥ 100 MeV (green curves) from 26 September 2011 to 29 September 2011, data available at the NOAA SWPC website, http://www.swpc.noaa.gov/today.html.

7.3 H Densities at Larger Geocentric Distances

In addition to the propagated fitting error, the obtained exospheric H number density distribution uncertainty increases for larger geocentric distances as the intensity of the geocorona is exceeded by that of the interplanetary glow. To illustrate the effect of this uncertainty, the radial dependence of predicted intensity on the position of a hypothetical observer looking radially away from the Earth is plotted in Figure 69.

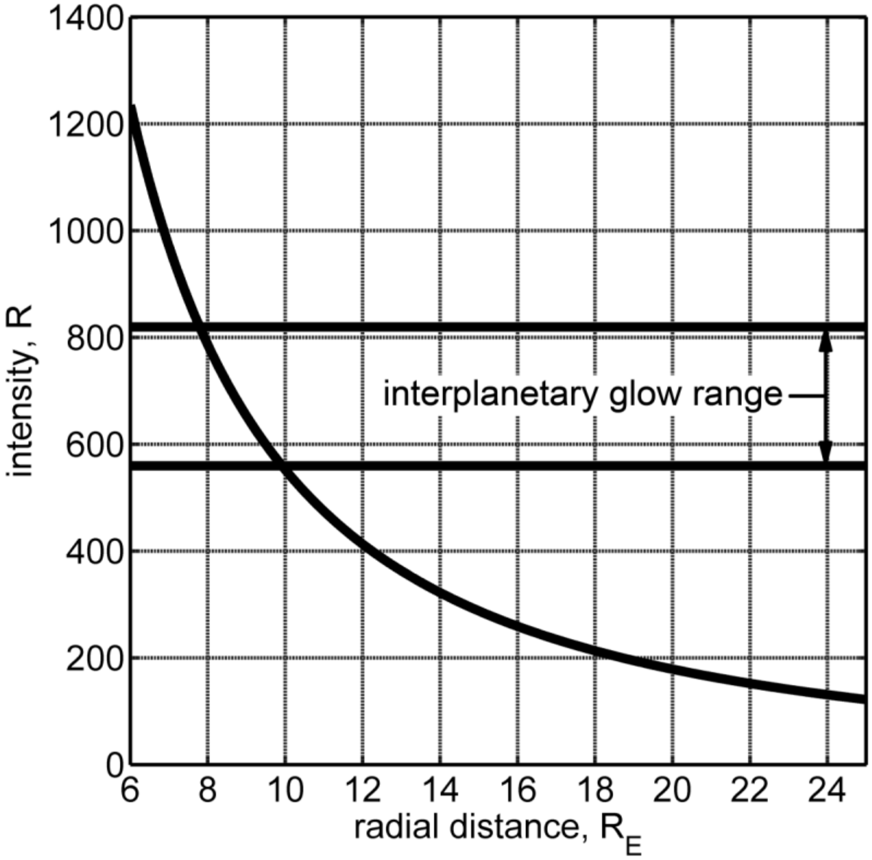

Figure 69. The radial dependence of predicted intensity on the position of a hypothetical observer looking radially away from the Earth. Two horizontal lines show the range of interplanetary glow intensities for all directions covered by the LADs on 11 June 2008.

For the TWINS-1 LAD observational geometry on 11 June 2008, the interplanetary glow intensity varied from 560 to 820 R. Thus, for geocentric distances $r > 8$ R_E, the interplanetary glow becomes comparable or dominates the observed intensities. Consequently, intrinsic uncertainty in the interplanetary glow map, which is difficult to precisely quantify as the map is obtained by complex reduction of SWAN/SOHO observations, could make the predictions of exospheric H distributions at large distances less reliable.

7.4 TWINS Simplified Operational Exospheric Model for Solar Minimum Conditions

As part of a collaborative effort with the Bonn group, published jointly [*Zoennchen et al.*, 2011], an averaged global H density distribution using LAD measurements from June to September 2008 was reconstructed since there was nearly constant solar minimum conditions for this entire three month period. The obtained distribution is an advancement in contrast to the commonly used *Rairden et al.* [1986] and *Østgaard et al.* [2003] models in that it introduces important asymmetries that impact the results of extracting ion densities from ENA images through inversion or forward modeling [e.g., *Grimes et al.*, 2010].

The solar F10.7 index, which correlates to some degree with the solar Lyman-α radiation output, fluctuated by about ± 2.5% around its average value of ~ 68×10^{-22} W m^{-2} Hz^{-1}. The composite solar Lyman-α flux from LASP varied by ± 2.2% around its average value of 3.5×10^{11} photons cm^{-2} s^{-1}. Consequently, the assumption of stable, invariant geocoronal and interplanetary H atom resonant scattering conditions was assumed. The obtained distribution is intended for use only during times of comparable solar activity.

The interplanetary glow was approximated using a representative all-sky map (Figure 70) that was derived from SWAN measurements on 11 June 2008 (W. Pryor and R. Gladstone, personal communication, November 2010).

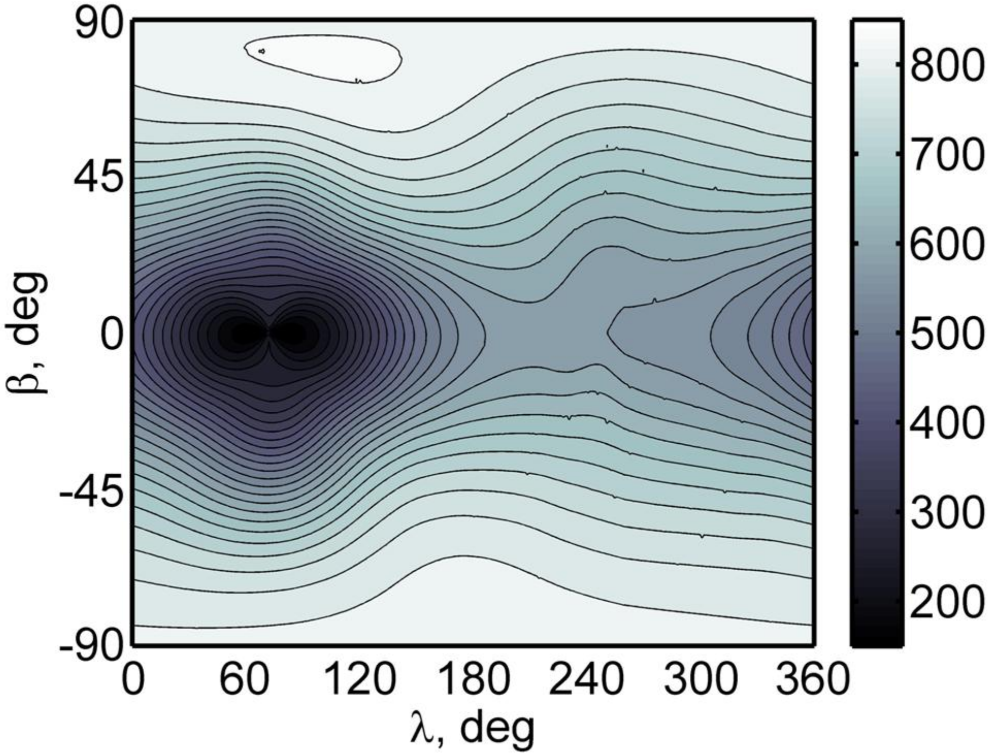

Figure 70. Interplanetary glow on 11 June 2008, derived from SWAN measurements (Pryor and Gladstone, personal communication, November 2010). The horizontal axis is ecliptic longitude *λ*, the vertical axis is ecliptic latitude *β*, and the color bar is in rayleighs.

It is assumed that only very small fluctuations of the interplanetary glow occurred from June to September 2008, associated with changes in the solar activity and additionally the parallax effect caused by the Earth's motion around the Sun. To investigate errors introduced by using a single representative all-sky map for the 3 month time period, interplanetary glow maps (W. Pryor and R. Gladstone, personal communication, November 2010) were compared for the first (11 June 2008) and last (13 September 2008) day used in the fitting procedure. The TWINS-1 LAD observed regions differed by an average of 5.6% of the actual observed intensities.

The solar activity conditions were quite stable at an extraordinarily low level from June to September 2008. TWINS-1 LAD measurements from four different time periods, 11 June, 22–24 July, 15–17 August, and 1–13 September, in 2008 were used as a representative data set because using all of the observations would be computationally impractical for a curve fitting procedure. The same amount of measurements was used from each of the four sections such that they contribute equally to the fitted solution. The measured Lyman-α intensities from LAD-1 and LAD-2 are shown in Figure 71 and Figure 72, respectively, versus the geocentric distance of each line-of-sight closest approach to the Earth, r_{LOS}. This type of plot, discussed in more detail in Section 6.2, is used as a convenient way of characterizing measurement sets. The coverage includes from 3 R_E to above 6 R_E by both LAD-1 and LAD-2, which is essential to obtaining accurate density distributions for this range.

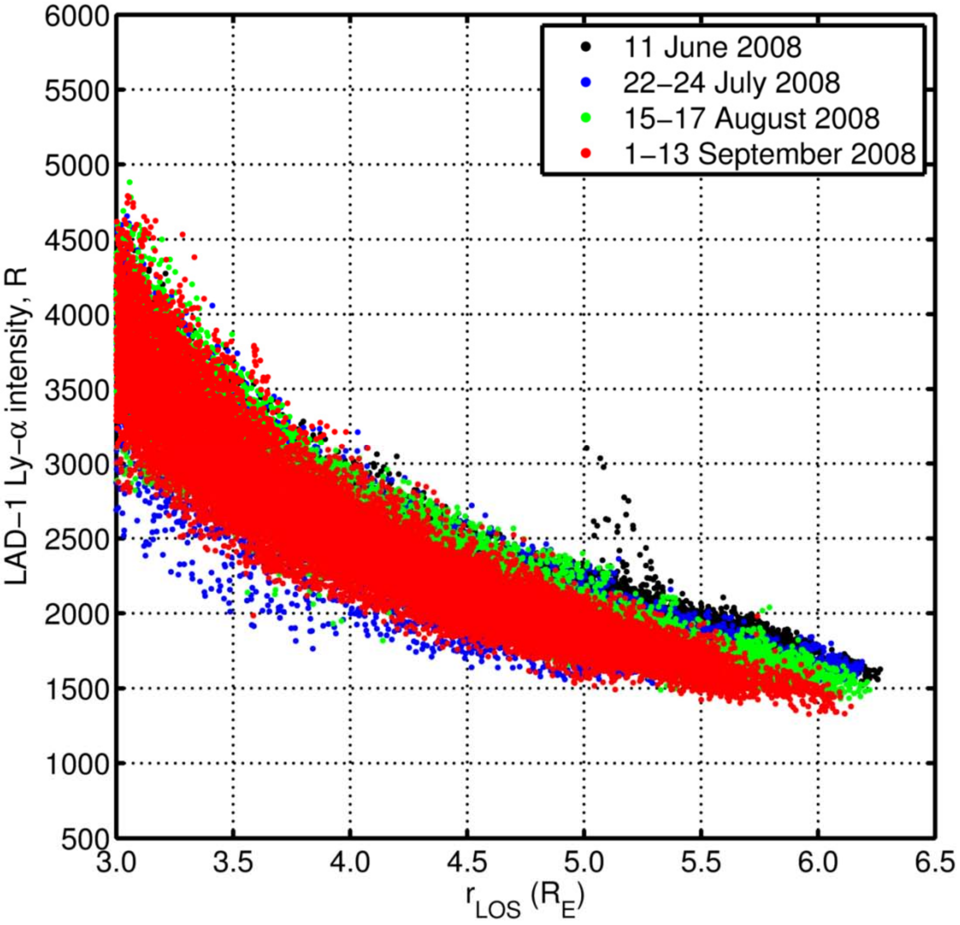

Figure 71. LAD-1 measured intensities for 11 June 2008 (black), 22-24 July 2008 (blue), 15-17 August 2008 (green), and 1-13 September 2008 (red) versus the geocentric distance of each line-of-sight closest approach to the Earth, r_{LOS}.

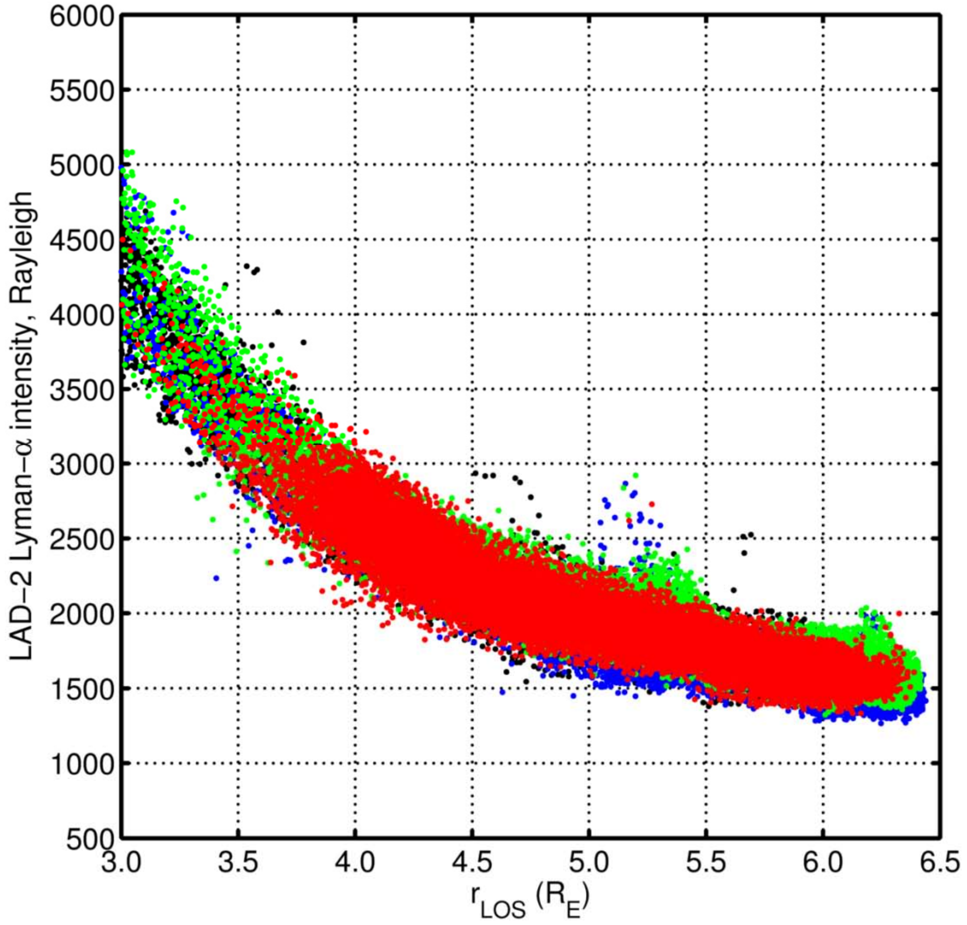

Figure 72. LAD-2 measured intensities for 11 June 2008 (black), 22-24 July 2008 (blue), 15-17 August 2008 (green), and 1-13 September 2008 (red) versus the geocentric distance of each line-of-sight closest approach to the Earth, r_{LOS}.

Since the geocorona exhibits a transition from optically thick to optically thin around 3 R_E [*Østgaard et al.*, 2003; *Zoennchen et al.*, 2010], the distribution is split into 2 segments: (A) for $r < 3$ R_E and (B) for $r > 3$ R_E. Segment (A) was chosen to be consistent with segment (B) by having nearly the same H number density of 800 cm^{-3} at the 3 R_E interface to provide a smooth transition.

Segment (A): < 3 R_E

For geocentric distances $r < 3$ R_E, no LAD data was used to obtain the H density distribution because of the optically thick conditions. Instead, a simple r-dependent density profile was developed, similar to the approach used by *Carruthers et al.* [1976], where two coefficients p and k were best fit,

$$n_H(r) = pe^{k/r}\ , \tag{68}$$

to a *Chamberlain* [1963] distribution with critical satellite altitude 2.5 R_E, resulting in numerical values $p = 70.005$ and $k = 7.5498$ between 1000 km altitude and $r < 3$ R_E.

Segment (B): > 3 R_E

For geocentric distances $r > 3$ R_E, a process of forward modeling fit a simplified version of the expansion in Equations 42 through 55 to the LAD observational data using a least squares curve fitting. The simplifications set all $B_{lm} = 0$, forcing dawn-dusk symmetry, and additionally setting $A_{21} = 0$ to minimize ecliptic north-south asymmetry. Additionally, isotropic scattering of Lyman-α photons on H atoms was assumed.

The corresponding parameter values in Equations 53 – 55 are listed in Table 3, where n_H is in cm^{-3} and r is in R_E.

Table 5. Parameters of the simplified operational model for solar minimum conditions (Equations 53 – 55) obtained using TWINS-1 LAD data from June to September 2008 in Geocentric Solar Ecliptic (GSE) coordinates; $n_H$is in cm^{-3} and *r* is in R$_E$.

Radial and Angular Parameters	June to September 2008
p	2.23647×10^4
k	-2.99318
a_{10}	-3.7311×10^{-2}
b_{10}	1.7820×10^{-2}
a_{11}	-1.85094×10^{-1}
b_{11}	5.0944×10^{-2}
c_{11}	0
d_{11}	0
a_{20}	1.59213×10^{-1}
b_{20}	-3.0911×10^{-2}
a_{21}	0
b_{21}	0
c_{21}	0
d_{21}	0
a_{22}	-1.40919×10^{-1}
b_{22}	3.6105×10^{-2}
c_{22}	0
d_{22}	0

Figure 73 shows that the radial dependence for both segments (A) and (B) on the dayside and nightside of the obtained distribution. The density profiles are consistent with but somewhat higher than the average profiles obtained by *Østgaard et al.* [2003] and *Rairden et al.* [1986].

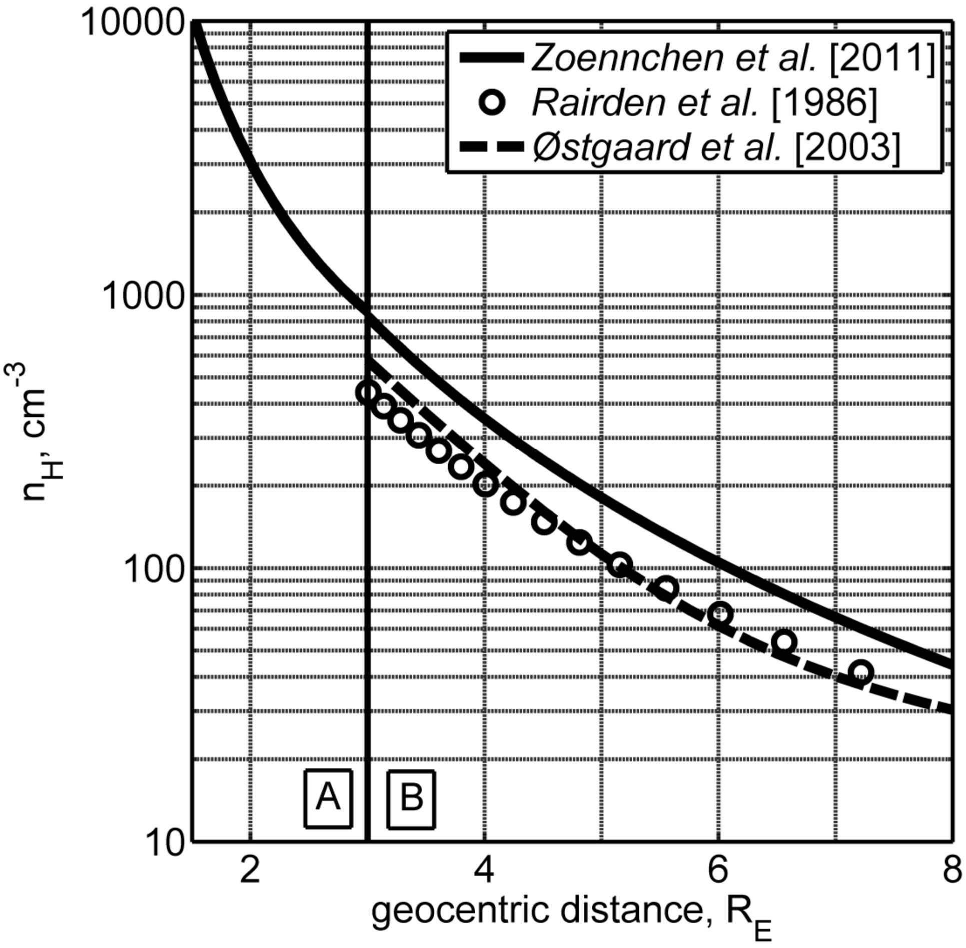

Figure 73. Comparison of different H number density profiles including segments (A) and (B) of the TWINS simplified operational exospheric model for solar minimum conditions (solid line), *Rairden et al.* [1986] (circles), and *Østgaard et al.* [2003] for solar zenith angle 90° (long dashed line).

The three-dimensional asymmetry, visible in Figure 74, is an advancement from the commonly used (by ENA modelers) distributions of *Rairden et al.* [1986] and *Østgaard et al.* [2003]. The global distribution is essentially cylindrically symmetric about the Sun-Earth line, exhibiting an enhancement in the antisolar direction that is consistent with the location of a geotail. The asymmetry does not, however, reflect spatial and temporal variations that occur over shorter time scales than the selected data set.

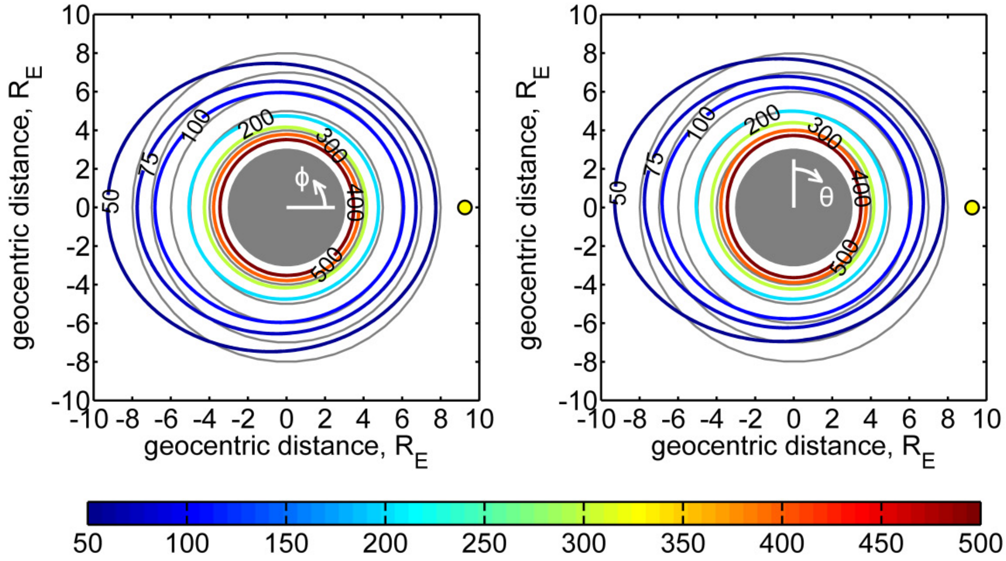

Figure 74. Contour plots of the exospheric H number density distribution for the TWINS simplified operational model for solar minimum conditions: (left) an ecliptic (*XY* plane) cross section and (right) a meridional (*XZ* plane) cross section. Also shown are the definitions of the angles ϕ and θ. Contours are lines of constant neutral hydrogen number density (cm^{-3}); the color bar is for the contour lines; the yellow dots are the direction to the Sun; the filled shaded circle represents the region with radius 3 R_E; and the grid of shaded concentric circles for r > 3 R_E, with a 1 R_E step, highlights the asymmetry of the distribution.

The estimated uncertainty in the obtained H density distribution is nearly constant at 15% to 20% from 3 R_E to 7 R_E, but then rapidly increases up to a factor of 2 at 10 R_E. For lower geocentric distances $r < 3$ R_E (within the region of the *Chamberlain* [1963]-like density profile), a relative error of 5 – 20% is assumed. It is recommended that the model be restricted to within these ranges or otherwise used with appropriate caution and error analysis.

7.5 Example Application, Ring Current Modeling

The TWINS mission enables three-dimensional visualization of large scale structures and dynamics of the magnetosphere. The observational geometry is ideal for investigation of the ring current, shown in Figure 75, which circles Earth in the equatorial plane. The ring current is generated by the longitudinal drift of energetic (10 – 200 keV) charged particles trapped on field lines between geocentric distances of 2 R_E and 7 R_E.

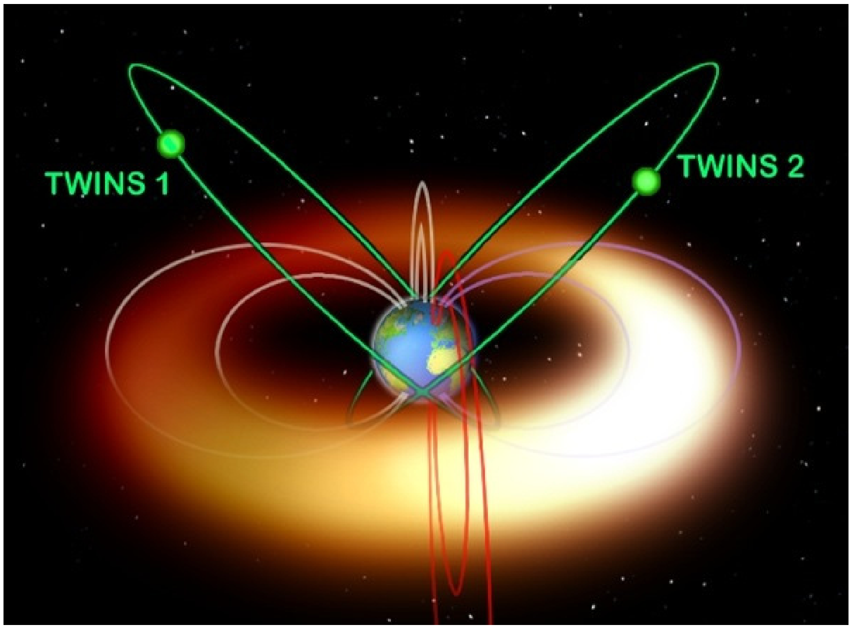

Figure 75. The TWINS mission stereoscopically images features of the magnetosphere from two satellites in widely spaced Molniya-type orbits, ideal for imaging ENAs that originate in the ring current (J. Goldstein).

Knowledge of the spatial distribution of exospheric hydrogen atoms limits accuracy of the reconstruction of ENA fluxes, and subsequently of energetic ion populations in the ring current. For example, long-term ring current decay is primarily due to collisions of charged particles with neutral atoms in the upper atmosphere. *Ilie et al.* [2011] simulated ion densities in the ring current during a geomagnetic storm that occurred on 22 July 2009 using five different H density distributions: *Rairden et al.* [1986], *Hodges* [1994], *Østgaard et al.* [2003], *Zoennchen et al.* [2011], and the 11 June 2008 distribution from this work. For high energy H^+ ions (≥ 100 keV), the H density distributions each predict similar decay rates of the ring current ions. However, for low energy ions, the decay rate and location of the ENA enhancements are highly dependent on the chosen exospheric H density distribution. Figure 76 shows the decay rate as a function of energy for an H^+ ring current ion at a geocentric distance of 5 R_E. *Hodges* [1994] predicts the highest overall H densities and thus results in the fastest decay rate. The decay rate predicted using the *Zoennchen et al.* [2011] distribution is closer to that of *Hodges* [1994] than of *Rairden et al.* [1986], *Østgaard et al.* [2003], and the 11 June 2008 distribution. The latter 3 have similar H density profiles and thus predict similar charge exchange decay rates as a function of ring current H^+ energy. The percentage difference between the 11 June 2008 distribution and *Hodges* [1994] predicted decay rates varies from 46% for equatorially mirroring particles to 53% for particles with an equatorial pitch angle of $\alpha = 30°$.

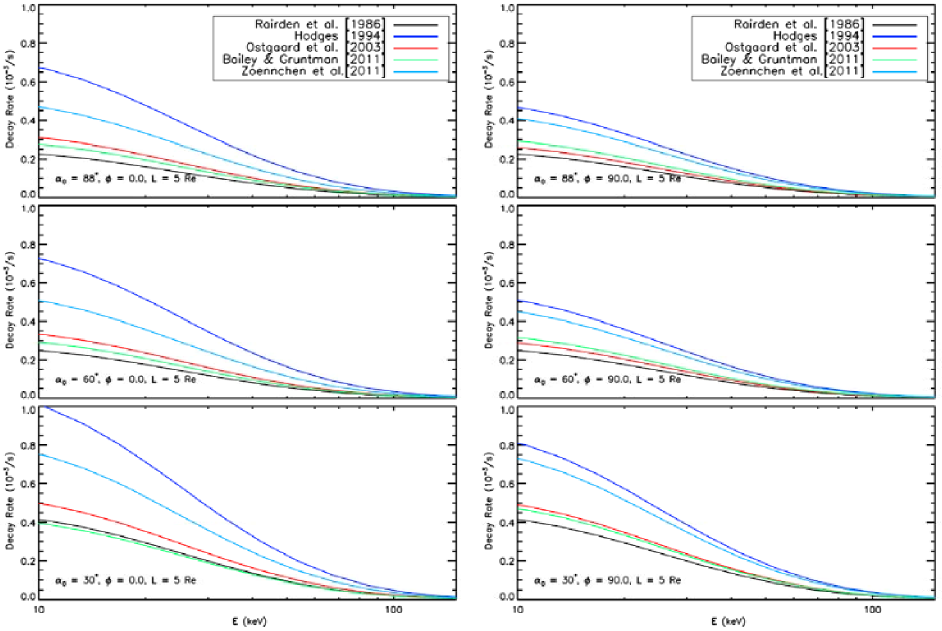

Figure 76. Variation of the charge exchange decay rate of ring current H^+ ions with 88° (top), 60° (middle), and 30° (bottom) equatorial pitch angle, at a radial distance of 5 R_E at midnight (ϕ = 0°, left column) and dawn (ϕ = 90°, right column) obtained using H density distributions from *Rairden et al.* [1986] (black), *Hodges* [1994] (blue), *Østgaard et al.* [2003] (red), the 11 June 2008 distribution [*Bailey and Gruntman*, 2011] (green), and *Zoennchen et al.* [2011] (light blue) [*Ilie et al.*, 2011].

The reconstructed ENA images rely on a line-of-sight integration of the ENA flux from the TWINS-2 position to the boundary of the HEIDI simulation domain,

$$j_{ENA} = \int j_{ion}\, \sigma_{H,H^+}\, n_H \, dl \, , \tag{69}$$

where j_{ion} corresponds to the H^+ ion differential flux from the HEIDI model, σ_{H,H^+} is the charge exchange cross section of an H^+ ion with an exospheric H atom, and n_H is the exospheric H number density distribution.

Figure 77 shows an ENA image of the 12 keV passband (6 – 18 keV) fluxes observed by TWINS-2 (top left) as well as reconstructed ENA images calculated from the Hot Electron Ion Drift Integrator (HEIDI) ion fluxes using the five different H density distributions. The limb of the Earth and the dipole field lines for geocentric distances of 4 R_E and 8 R_E are shown at four magnetic local times: noon (red lines), dusk (pink lines), midnight (black lines), and dawn (white lines).

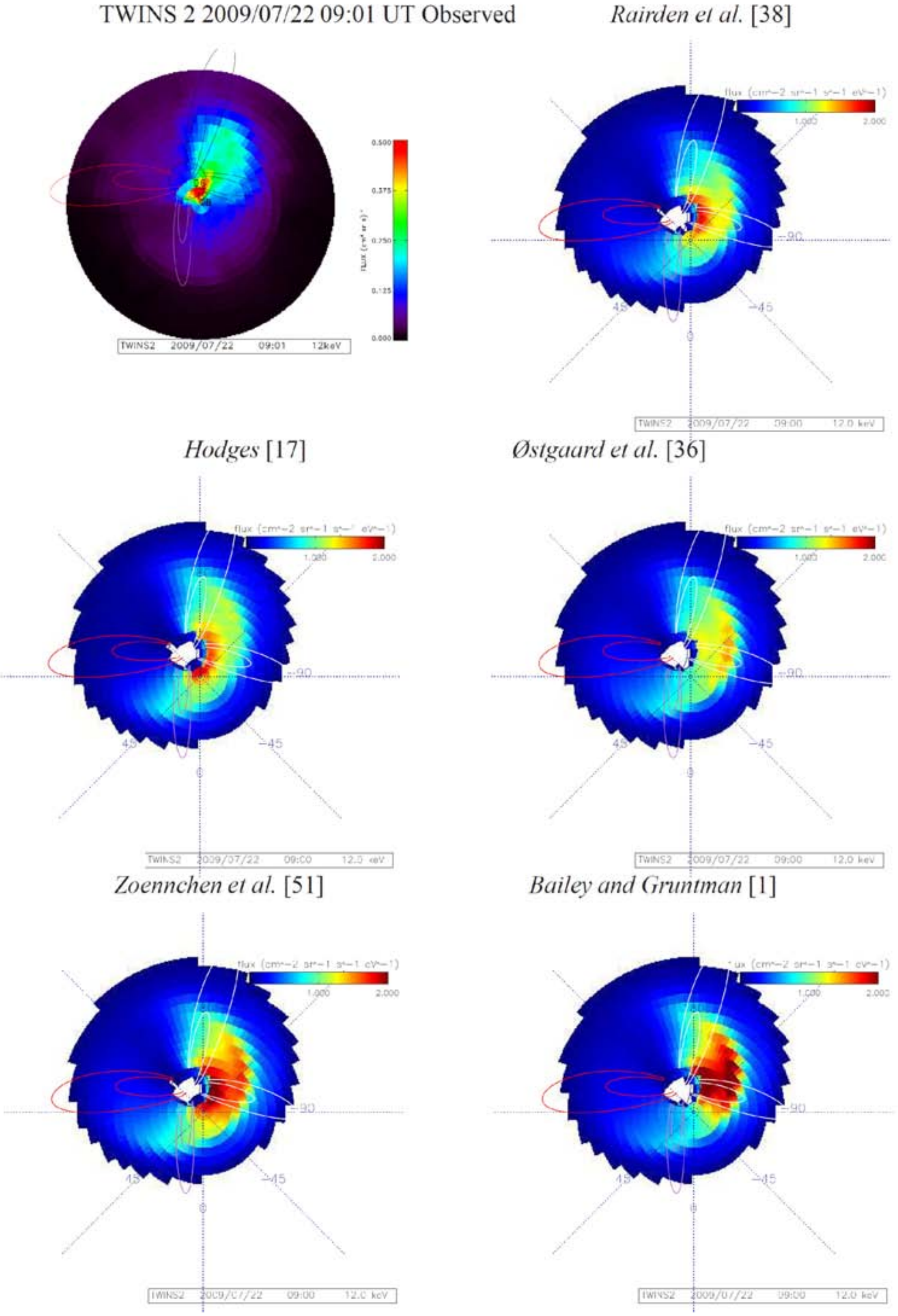

TWINS 2 2009/07/22 09:01 UT Observed

Rairden et al. [38]

Hodges [17]

Østgaard et al. [36]

Zoennchen et al. [51]

Bailey and Gruntman [1]

Figure 77. TWINS-2 observation of ENA fluxes in the 6 – 18 keV energy range (top left) and reconstructed ENA images using 5 different H density distributions: *Rairden et al.* [1986] (top right), *Hodges* [1994] (center left), *Østgaard et al.* [2003] (center right), *Zoennchen et al.* [2011] (bottom left), and the 11 June 2008 distribution [*Bailey and Gruntman*, 2011] (bottom right) [*Ilie et al.*, 2011].

Ilie et al. [2011] concluded that changing the H density distribution used to obtain n_H can have a significant impact on the reconstruction of ENA fluxes. For example, the TWINS-2 observation (Figure 77, top left) shows an enhancement in the midnight-dawn sector and weak ENA fluxes from noon-to-dusk during the 22 July 2009 storm. This spatial variation is only closely reproduced when using the 11 June 2008 distribution, which is an indication that allowing for dawn-dusk asymmetry in exospheric H density distributions may be essential for the reconstruction of certain magnetospheric features.

Chapter 8: Conclusions

A process for preparing TWINS data such that LAD measurements can be used to obtain global H density distributions with three-dimensional asymmetries above 3 R_E has been extensively described. Two considerations must be addressed when using the presented methodology to obtain distributions for days beyond the summer months of 2008. First, the majority of dayside measurements are excluded for having lines-of-sight that are pointed at $< 90°$ from the solar direction. Second, the relative cross calibration ratio between LAD-1 to LAD-2 changes with time.

LAD measurements from TWINS-1 on an example day of 11 June 2008 were used to obtain a global exospheric H density distribution for geocentric distances from 3 R_E to 8 R_E. The radial dependence of the spherically symmetric distribution is in agreement with the density profiles obtained by *Rairden et al.* [1986], *Hodges* [1994], and *Østgaard et al.* [2003]. For geocentric distances $r > 4.5\ R_E$, their density profiles, as well as the 11 June 2008 distribution, decrease more rapidly than that obtained by *Zoennchen et al.* [2010]. The 11 June 2008 distribution confirms the existence of an H density enhancement on the dayside, a feature previously reported by *Tinsley et al.* [1986] and *Hodges* [1994]. The 11 June 2008 distribution also exhibits an enhancement on the nightside, consistent with the location of a geotail, in agreement with the day-night asymmetry described by *Østgaard et al.* [2003], but less pronounced than reported by *Zoennchen et al.* [2010]. Another prominent asymmetry exists in the north-south direction, with larger densities in the Southern Hemisphere, similar to the *Hodges* [1994] solstice distributions for similar seasonal conditions. The dawn-dusk asymmetry is less prominent, but visible with densities slightly higher on the duskside.

A sequence of three global distributions with three-dimensional asymmetries using LAD data from TWINS-1 on 18-22 June 2008, 18-22 July 2008, and 18-22 August 2008 was obtained to investigate seasonal variations. All three distributions exhibit asymmetry that appears oriented with respect to the solar-antisolar direction such that there are enhancements on the dayside and nightside that are remarkably consistent with the spatial variation in the *Hodges* [1994] solstice distributions and *Carruthers et al.* [1976] images.

A sequence of 55 density profiles was obtained using TWINS-1 LAD data from August and October in 2011 as a way of investigating a possible response of the exosphere to geomagnetic variations because four magnetic storms occurred during this time period. Preliminary results suggest that exospheric H densities increase by 5% to 15% for the time period of a day or less in response to a magnetic storm.

For larger distances, uncertainty in the derived distributions accuracy increases for two reasons. First, the observational geometry is limited by a geocentric distance for an LAD line-of-sight closest approach to the Earth, r_{LOS}, that does not exceed 6.5 R_E. Second, accurate knowledge of the interplanetary glow becomes increasingly important as, above 8 R_E, it dominates the observed intensities.

The obtained asymmetries may be of particular interest to magnetospheric ENA imaging, which heretofore has largely relied on the spherically symmetric distribution of

Rairden et al. [1986]. An operational distribution for solar minimum conditions was collaboratively developed with the Bonn group and is now available for ENA modelers.

An analysis was summarized that demonstrates the importance of exospheric H density distributions for reconstructing images in ENA fluxes and obtaining ring current ion densities. Allowing dawn-dusk asymmetry in exospheric H density distributions may be essential for the reconstruction of certain magnetospheric features.

The unprecedented observational coverage of the LADs on TWINS opens the possibility for advancing scientific understanding of exospheric physics, including source and loss processes as well as more accurate details about the ballistic, orbital, and escaping populations of H atoms. The current rise to the next solar cycle (~ 11 year) maximum will offer a unique opportunity to investigate the response of the exosphere to enhanced solar activity. It is also anticipated that prediction capability for higher geocentric distances ($r > 8\ R_E$) will eventually become possible.

References

Anderson, D. E., Jr., and C. W. Hord (1977), Multidimensional radiative transfer: Applications to planetary coronae, *Planet. Space Sci.*, *25*, 563-571, doi: 10.1016/0032-0633(77)90063-0.

Bailey, J., and M. Gruntman, Experimental study of exospheric hydrogen atom distributions by Lyman-alpha detectors on the TWINS mission (2011), *J. Geophys. Res.*, *116*, A09302, doi: 10.1029/2011JA016531.

Bertaux, J. L., E. Kyrölä, E. Quémerais, R. Pellinen, R. Lallement, W. Schmidt, M. Berthé, E. Dimarellis, J. P. Goutail, C. Taulemesse, C. Bernard, G. Leppelmeier, T. Summanen, H. Hannula, H. Huomo, V. Kehlä, S. Korpela, K. Leppälä, E. Strömmer, J. Torsti, K. Viherkanto, J. F. Hochedez, G. Chretiennot, R. Peyroux, and T. Holzer (1995), SWAN: A study of solar wind anisotropies on SOHO with Lyman alpha sky mapping, *Solar Phys.*, *162*, 403-439, doi: 10.1007/BF00733435.

Bertaux, J. L. (1984), Helium and hydrogen of the local interstellar medium observed in the vicinity of the Sun, *NASA Conf. Publ.*, *CP 2345*, 3-23.

Bertaux, J. L., and J. E. Blamont (1970), OGO-5 measurements of Lyman-α intensity distribution and linewidth up to 6 earth radii, *Space Res.*, *10*, 591-601.

Bertaux, J. L., and J. E. Blamont (1973), Interpretation of OGO 5 Lyman alpha measurements in the upper geocorona, *J. Geophys. Res.*, *78*, 80-91, doi: 10.1029/JA078i001p00080.

Beth, H. A., and E. E. Salpeter (2008), Interaction with radiation, in *Quantum Mechanics of One- and Two-Electron Atoms*, 262-263, Dover Publications, New York.

Bevington, P. R., and D. K. Robinson (2003), Error analysis, in *Data Reduction and Error Analysis for the Physical Sciences*, pp. 36-50, McGraw-Hill, New York.

Bishop, J. (1985), Geocoronal structure: The effects of solar radiation pressure and the plasmasphere interaction, *J. Geophys. Res.*, *90*, 5235-5245, doi: 10.1029/JA090iA06p05235.

Bishop, J. (1999), Transport of resonant atomic hydrogen emissions in the thermosphere and geocorona: Model description and applications, *J. Quant. Spectrosc. Radiat. Transf.*, *61*, 473-491, doi: 10.1016/S0022-4073(98)0031-4.

Brandt, J. C., and J. W. Chamberlain (1959), Hydrogen radiation in the night sky, *Astrophys. J.*, *130*, 670-682, doi: 10.1086/146756.

Bush, B. C., and S. Chakrabarti (1995), Analysis of Lyman α and He I 584-Å airglow measurements using a spherical radiative transfer model, *J. Geophys. Res.*, *100*, 19609-19625, doi: 10.1029/95JA01210.

Carpenter, D. L. (1970), Whistler evidence of the dynamic behavior of the duskside bulge in the plasmasphere, *J. Geophys. Res.*, *75*, 3837-3847, doi: 10.1029/JA075i019p03837.

Carpenter, D. L., and C. G. Park (1973), On what ionospheric workers should know about the plasmapause-plasmasphere, *Rev. Geophys.*, *11*, 133-154, doi: 10.1029/RG011i001p00133.

Carpenter, D. L., B. L. Giles, C. R. Chappell, P. M. E. Décréau, R. R. Anderson, A. M. Persoon, A. J. Smith, Y. Corcuff, and P. Canu (1993), Plasmasphere dynamics in the duskside bulge region: A new look at an old topic, *J. Geophys. Res.*, *98*, 19243-19271, doi: 10.1029/93JA00922.

Carruthers, G. R., T. Page, and R. R. Meier (1976), Apollo 16 Lyman alpha imagery of the hydrogen geocorona, *J. Geophys. Res.*, *81*, 1664-1672, doi: 10.1029/JA081i010p01664.

Chamberlain, J. W. (1963), Planetary coronae and atmospheric evaporation, *Planet. Space Sci.*, *11*, 901-960, doi: 10.1016/0032-0633(63)90122-3.

Chamberlain, J. W. (1979), Depletion of satellite atoms in a collisionless exosphere by radiation pressure, *Icarus*, *39*, 286-294, doi: 10.1016/0019-1035(79)90171-4.

Chamberlain, J. W. (1980), Exospheric perturbations by radiation pressure: II. Solution for orbits in the ecliptic plane, *Icarus*, *44*, 651-656, doi: 10.1016/0019-1035(80)90133-5.

Chamberlain, J. W., and D. M. Hunten, Radiation pressure from solar Lyman-alpha, in *Theory of Planetary Atmospheres*, 353-354, Academic Press, New York.

Chappell, C. R., K. K. Harris, and G. W. Sharp (1970), The morphology of the bulge region of the plasmasphere, *J. Geophys. Res.*, *75*, 3848-3861, doi: 10.1029/JA075i019p03848.

Clarke, J. T., R. Lallement, J. L. Bertaux, H. Fahr, E. Quémerais, and H. Scherer (1998), HST/GHRS observations of the velocity structure of interplanetary hydrogen, *Astrophys. J.*, *499*, 482-488, doi: 10.1086/305628.

Coleman, T. F., and L. Yuying (1994), On the convergence of reflective Newton methods for large-scale nonlinear minimization subject to bounds, *Math. Program.*, *67*, 189-224, doi: 10.1.1.52.997.

Coleman, T. F., and L. Yuying (1996), An interior trust region approach for nonlinear minimization subject to bounds, *SIAM J. Optim.*, *6*, 418-445, doi: 10.1137/0806023.

Donahue, T. M. (1966), The problem of atomic hydrogen, *Ann. Geophys.*, *22*, 175-188.

Emerich, C., P. Lemaire, J. Vial, W. Curdt, U. Schühle, and K. Wilhelm (2005), A new relation between the central spectral solar H I Lyman α irradiance and the line irradiance measured by SUMER/SOHO during the cycle 23, *Icarus*, *178*, 429-433, doi: 10.1016/j.icarus.2005.05.002.

Fahr, H. J. (1974), The extraterrestrial UV-background and the nearby interstellar medium, *Space Sci. Rev.*, *15*, 483-540, doi: 10.1007/BF00178217.

Fuselier, S. A., H. O. Funsten, D. Heirtzler, P. Janzen, H. Kucharek, D. J. McComas, E. Möbius, T. E. Moore, S. M. Petrinec, D. B. Reisenfeld, N. A. Schwadron, K. J. Trattner, and P. Wurz (2010), Energetic neutral atoms from the Earth's subsolar magnetopause, *Geophys. Res. Lett.*, *37*, L13101, doi: 10.1029/2010GL044140.

Grimes, E. W., J. D. Perez, J. Goldstein, D. J. McComas, and P. Valek (2010), Global observations of ring current dynamics during CIR-driven geomagnetic storms in 2008, *J. Geophys. Res.*, *115*, A11207, doi: 10.1029/2010JA015409.

Gruntman, M. (1997), Energetic neutral atom imaging of space plasmas, *Rev. Sci. Instrum.*, *68*, 3617-3656, doi: 10.1063/1.1148389.

Gruntman, M., and V. Izmodenov (2004), Mass transport in the heliosphere by energetic neutral atoms, *J. Geophys. Res.*, *109*, A12108, doi: 10.1029/2004JA010727.

Hodges, R. R. (1994), Monte Carlo simulation of the terrestrial hydrogen exosphere, *J. Geophys. Res.*, *99*, 23229-23247, doi: 10.1029/94JA02183.

Holzer, T. E. (1977), Neutral hydrogen in interplanetary space, *Rev. Geophys.*, *15*, 467-490, doi: 10.1029/RG015i004p00467.

Hunten, D. M., and D. F. Strobel (1974), Production and escape of terrestrial hydrogen, *J. Atmos. Sci.*, *31*, 305-317, 10.1175/1520-0469(1974)031<0305:PAEOTH>2.0.CO;2.

Ilie, R., R. Skoug, H. Funsten, M. W. Liemohn, J. Bailey, M. Gruntman (2012), The impact of geocoronal density on ring current development, *J. Geophys. Res.*, accepted.

Kivelson, M. G., and C. T. Russell (1995), The plasmasphere, in *Introduction to Space Physics*, 298-300, Cambridge University Press, New York.

Kupperian, J. E., Jr., E. T. Byram, T. A. Chubb, and H. Friedman (1959), Far ultraviolet radiation in the night sky, *Planet. Space Sci.*, *1*, 3-6, doi: 10.1016/0032-0633(59)90015-7.

Levenberg, K., A method for the solution of certain problems in least-squares (1944), *Quart. App. Math.*, *2*, 164-168, doi: 10.1.1.135.865.

Liu, S. C., and T. M. Donahue (1974), The aeronomy of hydrogen in the atmosphere of the earth, *J. Atmos. Sci.*, *31*, 1118-1136, doi: 10.1175/1520-0469(1974)031<1118:TAOHIT>2.0.CO;2.

Mange, P., and R. Meier (1970), OGO 3 observations of the Lyman alpha intensity and the hydrogen concentration beyond 5 Re, *J. Geophys. Res.*, *75*, 1837-1847, doi: 10.1029/JA075i010p01837.

Marquardt, D. (1963), An algorithm for least-squares estimation of nonlinear parameters, *SIAM J. App. Math.*, *11*, 431-441, doi: 10.1137/0111030.

McComas, D. J., F. Allegrini, J. Baldonado, B. Blake, P. C. Brandt, J. Burch, J. Clemmons, W. Crain, D. Delapp, R. DeMajistre, D. Everett, H. Fahr, L. Friesen, H. Funsten, J. Goldstein, M. Gruntman, R. Harbaugh, R. Harper, H. Henkel, C. Holmlund, G. Lay, D. Mabry, D. Mitchell, U. Nass, C. Pollock, S. Pope, M. Reno, S. Ritzau, E. Roelof, E. Scime, M. Sivjee, R. Skoug, T. S. Sotirelis, M. Thomsen, C. Urdailes, P. Valek, K. Viherkanto, S. Weidner, T. Ylikorpi, M. Young, J. Zoennchen (2009), The Two Wide-angle Imaging Neutral-atom Spectrometers (TWINS) NASA Mission-of-Opportunity, *Space Sci. Rev.*, *142*, 157-231, doi: 10.1007/s11214-008-9467-4.

Meier, R. R. (1969), Balmer alpha and Lyman beta in the hydrogen geocorona, *J. Geophys. Res.*, *74*, 3561-3574, doi: 10.1029/JA074i014p03561.

Meier, R. R.(1977), Some optical and kinetic properties of the nearby interstellar gas, *Astron. Astrophys.*, *55*, 211-219.

Meier, R. R. and P. Mange (1970), Geocoronal hydrogen: An analysis of the Ly-α airglow observed from OGO-4, *Planet. Space Sci.*, *18*, 803-821, doi: 10.1016/0032-0633(70)90080-2.

Meier, R. R., and P. Mange (1973), Spatial and temporal variations of the Lyman-alpha airglow and related atomic hydrogen distributions, *Planet. Space Sci.*, *21*, 309-327, doi:.10.1016/0032-0633(73)90030-5.

Nass, H. U., J. H. Zoennchen, G. Lay, and H. J. Fahr (2006), The TWINS-LAD mission: Observations of terrestrial Lyman-α fluxes, *Astrophys. Space Sci. Trans.*, *2*, 27-31, doi: 10.5194/astra-2-27-2006.

Østgaard, N., S. B. Mende, H. U. Frey, G. R. Gladstone, and H. Lauche (2003), Neutral hydrogen density profiles derived from geocoronal imaging, *J. Geophys. Res.*, *108*, 1300, doi: 10.1029/2002JA009749.

Pryor, W., G. Holsclaw, W. McClintock, M. Snow, R. Vervack, R. Gladstone, A. Stern, K. Retherford, and P. Miles (2012), *Astron. Astrophys.*, submitted.

Quémerais, E., J. L. Bertaux, R. Lallement, B. Sandel, and V. Izmodenov (2003), Voyager 1/UVS Lyman α glow data from 1993 to 2003: Hydrogen distribution in the upwind outer heliosphere, *J. Geophys. Res.*, *108*(A10), 8029, doi: 10.1029/2003JA009871.

Rairden, R. L., L. A. Frank, and J. D. Craven (1983), Geocoronal imaging with dynamics explorer: A first look, *Geophys. Res. Lett.*, *10*, 533-536, doi: 10.1029/GL010i007p00533.

Rairden, R. L., L. A. Frank, and J. D. Craven (1986), Geocoronal imaging with dynamics explorer, *J. Geophys. Res.*, *91*, 13613-13630, doi: 10.1029/JA091iA12p13613.

Richter, M., U. Kroth, R. Thornagel, H. J. Fahr, G. Lay, and H. U. Nass (2001), Calibration of Lyman-α detectors for the NASA satellites TWINS, *Annu. Rep. S15*, BESSY, Berlin.

Roelof, E. C. (1987), Energetic neutral atom image of a storm-time ring current, *Geophys. Res. Lett.*, *14*(6), 652-655, doi:10.1029/GL014i006p00652.

Schwadron, N. A., and D. J. McComas (2010), Pickup ions from energetic neutral atoms, *Astrophys. J.*, *712*, L157-L159, doi: 10.1088/2041-8205/712/2/L157.

Stephan, S. G., S. Chakrabarti, J. Vickers, T. Cook, and D. Cotton (2001), Interplanetary H Lyα observations from a sounding rocket, *Astrophys. J.*, *559*, 491-500, doi: 10.1086/322322.

Thomas, G. E. (1963), Lyman α scattering in the Earth's hydrogen geocorona, *J. Geophys. Res.*, *68*, 2639-2660, doi: 10.1029/JZ068i009p02639.

Thomas, G. E. (1970), Ultraviolet observations of atomic hydrogen and oxygen from the OGO satellites, *Space Res.*, *10*, 602-607.

Thomas, G. E. (1978), The interstellar wind and its influence on the interplanetary environment, *Annu. Rev. Earth Planet. Sci.*, *6*, 173-204, doi: 10.1146/annurev.ea.06.050178.001133.

Thomas, G. E. and D. E. Anderson, Jr. (1976), Global atomic hydrogen density derived from OGO-6 Lyman alpha measurements, *Planet. Space Sci.*, *24*, 303-312, doi: 10.1016/0032-0633(76)90042-8.

Thomas, G. E., and R. C. Bohlin (1972), Lyman-alpha measurements of neutral hydrogen in the outer geocorona and in interplanetary space, *J. Geophys. Res.*, *77*(16), 2752-2761, doi: 10.1029/JA077i016p02752.

Tinsley, B. A., R. R. Hodges, and R. P. Rohrbaugh (1986), Monte Carlo models for the terrestrial exosphere over a solar cycle, *J. Geophys. Res.*, *91*(A12), 13631-13647, doi: 10.1029/JA091iA12p12631.

Tobiska, W. K. (2001), Validating the solar EUV proxy, E10.7, *J. Geophys. Res.*, *106*(A12), 29969-29978, doi: 10.1029/2000JA000210.
Tobiska, W. K., S. D. Bouwer, and B. R. Bowman (2008), The development of new solar indices for use in thermospheric density modeling, *J. Atm. Solar-Terr. Phys.*, *70*, 803-819, doi: 10.1016/j.jastp.2007.11.001

Wallace, L., C. A. Barth, J. B. Pearce, K. K. Kelly, D. E. Anderson, Jr., and W. G. Fastie (1970), Mariner 5 measurement of the earth's Lyman alpha emission, *J. Geophys. Res.*, *75*, 3769-3777, doi: 10.1029/JA075i019p03769.

Woods, T. N., W. K. Tobiska, G. J. Rottman, and J. R. Worden (2000), Improved solar Lyman α irradiance modeling from 1947 through 1999 based on UARS observations, *J. Geophys. Res.*, *105*(A12), 27195-27215, doi: 10.1029/2000JA000051.

Zoennchen, J. H., U. Nass, G. Lay, and H. J. Fahr (2010), 3-D-geocoronal hydrogen density derived from TWINS Ly-α-data, *Ann. Geophys.*, *28*, 1221-1228, doi: 10.5194/angeo-28-1221-2010.

Zoennchen, J. H., J. J. Bailey, U. Nass, M. Gruntman, H. Fahr, and J. Goldstein (2011), The TWINS exospheric neutral H-density distribution under solar minimum conditions, *Ann. Geophys.*, *29*, 2211-2217, doi: 10.5194/angeo-29-2211-2011.

Appendix: List of Publications

Published Articles

Bailey, J., and M. Gruntman, Experimental study of exospheric hydrogen atom distributions by Lyman-alpha detectors on the TWINS mission (2011), *J. Geophys. Res.*, *116*, A09302, doi: 10.1029/2011JA016531.

Zoennchen, J. H., J. J. Bailey, U. Nass, M. Gruntman, H. Fahr, and J. Goldstein (2011), The TWINS exospheric neutral H-density distribution under solar minimum conditions, *Ann. Geophys.*, *29*, 2211-2217, doi: 10.5194/angeo-29-2211-2011.

Accepted Articles

Ilie, R., R. Skoug, H. Funsten, M. W. Liemohn, J. Bailey, M. Gruntman (2012), The impact of geocoronal density on ring current development, *J. Geophys. Res.*, accepted.

It is anticipated that one or two additional articles will be submitted in 2012.

Conferences

American Geophysical Union Fall Meeting
San Francisco, CA
13-17 December 2010

American Geophysical Union Fall Meeting
San Francisco, CA
5-9 December 2011

THEMIS-TWINS Workshop
University of California – Los Angeles, CA
21-25 March 2011

Inner Magnetosphere Coupling II
University of California – Los Angeles, CA
19-22 March 2012

Presentations

Invited Monthly Speaker Series
The Aerospace Corporation – El Segundo, CA
3 August 2011

TWINS Science Team Meetings
Southwest Research Institute – San Antonio, TX
9-11 February 2009 and 3-5 February 2010

TWINS Science Team Meetings
Johns Hopkins University Applied Physics Laboratory – Laurel, MD
18-20 August 2009 and 16-18 August 2010

TWINS Weekly Teleconferences
15 July 2010, 10 February 2011, 9 June 2011, and 4 August 2011